# Layer resolved Lattice Relaxation in Magnetic $Fe_xPt_{1-x}$ Nanoparticles

Diploma Thesis
to obtain the degree of Diplom-Physikerin

at the Department of Physics
**University Duisburg-Essen**

submitted by
**Nina Friedenberger**
from Heiligenhaus, Germany

**Revised Version**

March 12, 2007

# Contents

# Abstract

The layer-resolved lattice structure of $Fe_xPt_{1-x}$ nanoparticles with different shapes, sizes (2 - 6 nm) and compositions has been investigated by focal series reconstruction of the exit wave in high-resolution electron microscopy. This recently developed technique allows the resolution of the distance between atomic columns with sub- angstrom precision and in principle should offer chemical sensitivity to the position of different atomic elements within a single column via the "Z-contrast" , i.e. the number of electrons per atom. The detailed analysis shows that:
a) surfaces and edges of particles can be directly visualized allowing the counting of missing atom columns at edges and along surfaces,
b) no ideal cuboctahedra or other platonic solids are formed,
c) the directly resolved lattice fct distortion of $L1_0$ ordered FePt cuboctahedra is similar to the bulk material (c/a= 0.98),
d) the overall lattice constant of the nanoparticles is up to 4 % expanded,
e) a radial composition gradient or a Pt enrichment at the surface is not observed in general,
f) in one cuboctahedron an 8% surface relaxation of the (111) facets is observed while the (100) and (110) surface planes show no significant inward or outward relaxation,
g) an absolute determination of Fe and Pt positions in the nanoparticle requires a three-dimensional imaging of the particle and a two-dimensional projection always leaves room for interpretation.
The latter point is demonstrated by simulations of the Z-contrast in a simplified model. Furthermore, experimental variations of the distance between atomic columns are analyzed by comparison to the expected spacings when the columns contain different amounts of the smaller Fe or larger Pt atoms. Small experimentally observed oscillations of the lattice spacings may be attributed to this effect.

# Zusammenfassung

Die lagenaufgelöste Gitterstruktur von $Fe_xPt_{1-x}$ Nanopartikeln verschiedener Formen, Größen (2 - 6 nm) und Kompositionen wurde mittels Fokus-Serien-Rekonstruktion der Austritts-Welle in der Hochauflösenden Elektronenmikroskopie untersucht. Diese vor kurzem entwickelte Technik ermöglicht die Auflösung interatomarer Distanzen mit sub-Ångström Präzision und prinzipiell auch chemischer Sensitivität bezüglich der Positionen verschiedener Elemente innerhalb einer einzelnen Atomsäule durch den "Z-Kontrast", bzw. der Anzahl an Elektronen pro Atom. Die detaillierte Analyse zeigt:
a) Oberflächen und Ecken der Partikel können direkt dargestellt werden, wodurch das Abzählen fehlender Atomsäulen an den Kanten und entlang der Oberfläche ermöglicht wird.
b) ideale Kuboktaeder oder andere platonische Festkörper entstehen nicht,
c) die direkte lagenaufgelöste fct Verzerrung eines $L1_0$-geordneten FePt Kuboktaeder ist vergleichbar zum Bulk (c/a= 0.98),
d) die mittlere Gitterkonstante der Nanopartikel ist um bis zu 4% ausgedehnt,
e) ein radialer Kompositionsgradient oder eine Pt-Anreicherung an der Oberfläche wird im allgemeinen nicht beobachtet,
f) in einem Kuboktaeder wird eine 8%ige Oberflächen-Relaxation einer der (111)-Facetten beobachtet, während die (100)- und (110)- Oberflächen keine signifikante äußere oder innere Relaxation zeigen,
g) eine absolute Bestimmung der Fe- und Pt-Positionen in einem Nanopartikel erfordert eine dreidimensionale Abbildung des Partikels und eine zweidimensionale Projektion lässt immer Platz für Interpretationen.
Letzteres wird durch Z-Kontrast Simulationen an einem vereinfachtem Modell gezeigt. Desweiteren werden experimentelle Variationen der Abstände zwischen Atomsäulen mit den erwarteten Abständen für Atomsäulen verschiedener Anzahl an kleineren Fe- und größeren Pt-Atomen verglichen. Kleine experimentell gefundene Oszillationen des Gitterabstandes könnten diesem Effekt zugeordnet werden.

# Chapter 1

# Introduction

Magnetic nanoparticles (NP) have become an important material in bio-medical applications ranging from gene sequencing to hypothermia treatment. For different types of applications the size, shape and magnetic properties of the nanoparticles must be controllable and the material must be bio-compatible [SM04]. Also, combining magnetic with luminescent properties in a single nanoparticle seems to be a promising route for future applications [SM06]. Water - based colloidal supensions either directly produced by organometallic chemistry or from gasphase condensed particles [Ace05] offer interesting approaches to obtain well defined, monodisperse particle systems.
In magnetic nanocrystals of different compositions one can establish and select a wide range of magnetic properties ranging from soft- to hard-magnetic behavior. Especially FePt (in its chemically ordered $L1_0$-structure) is a material with one of the biggest magnetic anisotropies ($10^6 J/m^3$) which makes it very interesting for applications in future magnetic storage media. A storage density of up to 20 Tbit/inch$^2$ is possible, if $L1_0$-ordered FePt nanoparticles can be arranged in two dimensional arrays of several cm$^2$ size by self organization. At the moment a storage density of 140 Gbit/inch$^2$ is state of the art for magnetic storage media.
FePt NPs can either be prepared by wet chemical or by gasphase synthesis methods. For the gasphase preparation the crystal structure of the NP depends on the nucleation pressure and the sintering temperature (e.g. [Dmi03]). Recent experiments also confirmed the increase of chemical order due to the addition of $N_2$ [Dmi06c, Dmi06b].
Chemically prepared FePt nanoparticles have a disordered face centered cubic (fcc) structure which yields a small magnetic anisotropy ($10^4 J/m^3$). The phase transition to the tetragonal distorted $L1_0$-phase due to volume diffusion is induced by annealing to more than 600°C for several minutes.

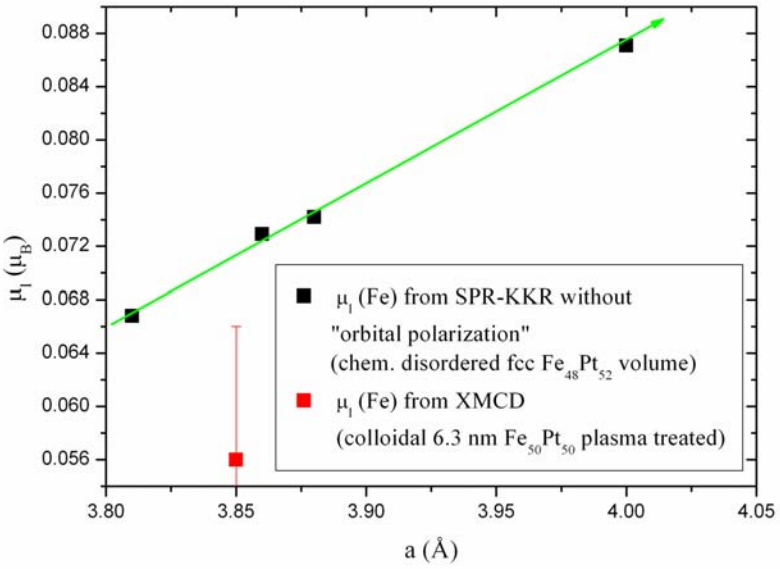


**Figure 1.1:** Experimentally measured and calculated (by SPR-KKR calculations without orbital polarization) orbital magnetic moment of $\mu_l$(Fe).

Monte Carlo Simulations of $L1_0$-ordered NPs were performed to study the surface segregation behavior and ordering temperature as a function of particle size [Mue05, Yan05]. Those simulations yielded a Pt-segregation to the surface which was also claimed by Wang et al. [Wan06] to explain the experimentally found surface layer relaxation of stoichiometric FePt icosahedric NPs.
Spin polarized relativistic calculations by C. Antoniak in our group for chemically disordered $Fe_{48}Pt_{52}$ bulk showed a significant increase of the orbital magnetic moment $\mu_l$ as a function of the lattice parameter (fig. 1.1 for Fe). From XMCD measurements a different behavior was found for colloidal FePt-Nanoparticles [Ant06b]: $\mu_l$(Fe) decreased and $\mu_l$(Pt) increased with respect to the calculated values. How can these deviations be explained? The question is if local compositional changes like the Pt-segregation to the surface can be the origin of those changes in the orbital magnetic moment. Figure 1.2 shows different chemical distributions of Fe and Pt atoms in a NP and suggests that the lattice constant and the lattice spacing, respectively, might not be unique throughout the particle and therefore will definitely influence the orbital magnetic moment. Another interesting question in that context is how a radial composition gradient or a shell-wise layered structure have an influence on the lattice parameter in a NP. The experimental investigation of these effects was the aim of this thesis. Therefore recently introduced High Resolution Transmission Electron Microscopy (HR-TEM) techniques which allow the determination of lattice

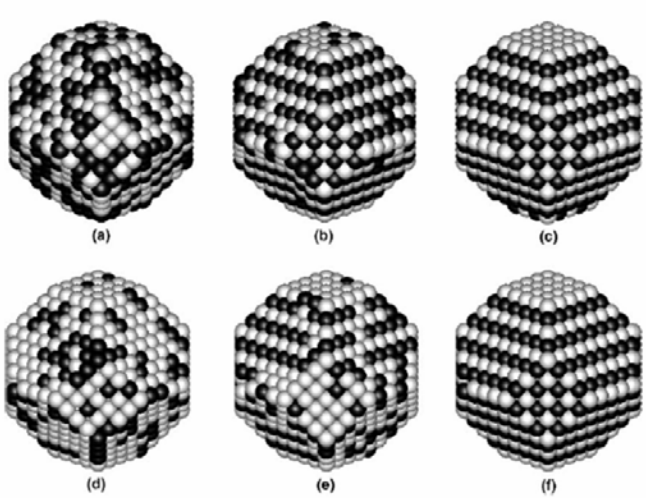


**Figure 1.2:** This figure shows 6 snapshots of the equilibrium structures of an equiatomic truncated cuboctahedron FePt-NP at different temperatures. White and dark circles represent Pt and Fe atoms, respectively [Yan05].

parameters of NPs with sub-Angstrom resolution [O´K01b] were applied. These techniques were available at the National Center for Electron Microscopy in Berkeley (NCEM). In this thesis I focussed on the following steps:

1. Sample Preparation for HR-TEM
2. HR-TEM-Analysis in Berkeley (National Center for Electron Microscopy) and in Duisburg
3. Exit Wave Reconstruction of focal series HRTEM-images, which allows the retrieval of the full phase and amplitude information of the electron exit wave.
4. Layer (atom column) resolved evaluation and interpretation of data
5. Image simulations to verify the results

In chapter 2 the main aspects of the theory of HR-TEM are summarized in short. The method of Exit-Wave-Reconstruction (EWR) is explained, and the process of image simulation is described. It is shown that EWR is the only feasible method yielding chemical sensitivity with sub-Angstrom resolution. After the theoretical description of the fundamentals several preparation methods for the NPs investigated in this thesis are shortly described. Finally the layer resolved analysis for chemically and gas-phase prepared NPs is discussed in detail. It is shown that under specific conditions a correlation with the

measured lattice relaxation and the chemical order within the atomic planes and columns can be deduced.

# Chapter 2

# Basics

This chapter gives an introduction to the theory and functionality of High Resolution Transmission Electron Microscopy. Since image simulations are required for quantitative interpretations of HR-TEM-images the main aspects are presented in section 2.1.5. Yet the main focus of this chapter will be the explanation of the method of Exit-Wave-Reconstruction to achieve sub ångstrom resolution. A theoretical overview concerning the idea and concept of EWR is given in 2.2.2. A short manual for the TrueImage software which was used for EWR can be found in Appendix A-5.

## 2.1 Theory of HR-TEM

The theory of (High Resolution) Transmission Electron Microscopy has been described in many textbooks [Rei84, Wil96]. Here only the most important facts only will be presented to understand HR-imaging.
Using electrons for microscopy yields smaller wavelengths and therefore a higher resolution. Theoretically, the resolution is 5 times higher than for visible light. For a 300kV ($\lambda = 1.97pm$) electron microscope the point-resolution should be in the range of 1 pm, for example, according to the Rayleigh criterium [Wil96]. The typical (point) resolution of a present TEM is worse than the calculated wavelength of the electrons. The attainable resolution of a transmission electron microscope (TEM) is mainly determined by the properties of the objective lens. One major lens defect, called spherical aberration and characterised by the spherical aberration coefficient, $C_S$, causes rays or electrons away from the optical axis not to be focused on the same focal point as those propagating on the optical axis [Sch05]. Nowadays, the highest achieved resolution is 0.78 Angstrom in Si [112] [Kis06a]. Fig. 2.1 shows the geometrical optics in a Transmission electron microscope (TEM) in

imaging (a) and diffraction mode (b).

### 2.1.1 Principle of High Resolution - Phase Contrast

There are in general three different contrast mechanisms in TEM. The *mass-thickness contrast*, the *diffraction contrast* and the *phase contrast*. In general the contrast, abbr.: $(C)$, can be defined as the difference of the intensity $(\Delta I)$ between two adjacent areas $I_1$ and $I_2$ [Wil96]:

$$C = \frac{(I_1 - I_2)}{I_1} = \frac{\Delta I}{I_1} \tag{2.1}$$

The phase contrast arises due to the differences in the phase of the electron waves scattered through a thin specimen to which the *weak phase object approximation* (WPOA) can be applied. This contrast mechanism is sensitive to many influencing factors like thickness changes of the specimen or astigmatism of the objective lens. Therefore the images are not easy to interpret. The phase contrast offers an improved sensitivity for the analysis of the atomic structure of thin specimens [Wil96]. For phase imaging several scattered electron beams contribute to the image and need to be properly reconstructed. In this context another aspect has to be mentioned, the appearance of lattice fringes in High Resolution TEM. In [Wil96] the origin is described using a simple two beam approximation. The result shows that the intensity varies sinusoidally with different periodicity for different values of $\mathbf{g}'$. $\mathbf{g}$ is the diffraction vector for the corresponding diffracted beam and $\mathbf{g}' = \mathbf{g}+\mathbf{s}_g$, where $\mathbf{s}_g$ = excitation error. With care the fringes can be related to the spacing of the lattice planes normal to $\mathbf{g}'$ keeping in mind that they are not direct images of the structure itself! Nevertheless, they can give lattice spacing information.

#### Image information - Amplitude-Phase-Diagrams

Taking into account the scattering cross-sections of the electron wave with the atomic potentials of the specimen and the interference of several beams it is possible to achieve atomic resolved information as described in section 2.1.1. Electron waves of the form: $\Psi = A\exp(i\phi)$ are fully described by their amplitude and phase.
However, in the TEM one measures intensities only. The amplitude and phase information is lost. Therefore the technique of reconstructing the electron exit wave was developed, see section 2.2.2. The electron exit wave is the wave directly below the sample plane. It only contains the information of the sample and is not modified by lenses. Unfortunately, the electron exit wave cannot be detected directly. It propagates through the optical system

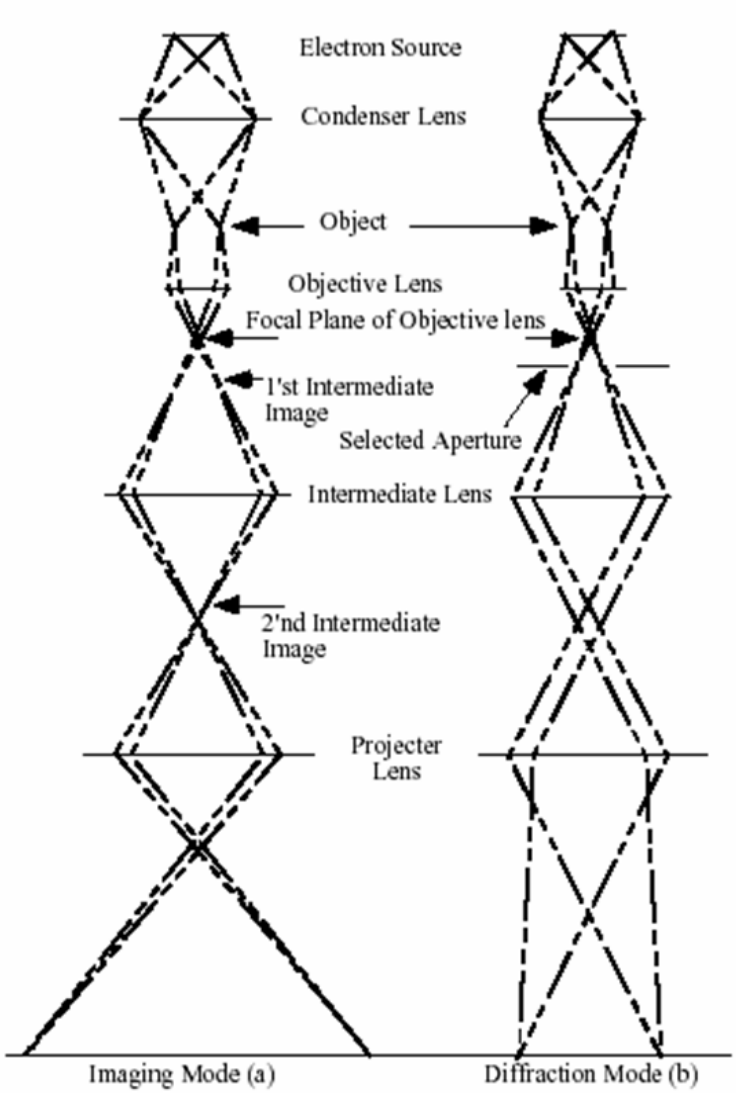


**Figure 2.1:** Geometrical optics representation of the TEM in imaging mode (a), and diffraction mode (b)(adapted from [Kila]).

of the microscope until reaching the screen or CCD camera. Both, the imaging system and the detection system influence the electron exit wave so that the acquired image has lost part of its information. These effects are mathematically described by the contrast transfer function (CTF) described in the next section 2.1.3.
If full phase and amplitude information are known, they can be presented in a polar plot: amplitude-phase diagrams, also called Argand plots. In these diagrams the amplitude defines the length of the vector and the phase is represented by the polar angle.

### 2.1.2 Analyzing Images - Delocalization and Resolution

The point of interest in acquiring and quantitatively analyzing HRTEM-images is the separation of individual atomic columns. Typically, lattice fringes are observed with high-resolution transmission electron microscopy (HR-TEM). But the direct imaging of the lattice structure of 2 to 6 nm sized nanoparticles is often disturbed by aberration and delocalization effects. The difficulty in imaging interfaces or surfaces is to judge where the interface is exactly located, because the information is spreading over a larger area (compare fig. 2.2 [Gro99, Sch05]). This so-called delocalization is due to a non-zero $C_S$ value. The electrons from one point of an object are not imaged into a single point but rather into a small disk smearing out the information (the information is no longer localized but delocalized).

Artifact-free imaging and ultimate resolution is possible by reducing the main lens defects either by software or by hardware. The hardware is featured by integrating new electron-optical components like monochromators or $C_S$ correctors into the microscope. The TrueImage$^{TM}$ software obtains directly interpretable results from high-resolution TEM beyond the point-resolution. This reconstruction mathematically eliminates the spherical aberration of the microscope, thus removing delocalization effects from the FEG electron source and therefore it is a very good alternative compared to working with the new generation of microscopes, the Cs aberration-corrected TEMs. And please note that even in an hardware corrected microscope it is still beneficial to make EWR in order to recover the exit wave from the image intensities [Jin02].
Resolution up to the information limit of the microscope is achieved by applying an special algorithm to the images which are acquired in focal series. In this process lens aberrations and delocalization are compensated and the resolution of the microscope can be pushed to the information limit. First sub-Angstrom resolution was reported in [Kis]. For the OAM (One Angstrom Microscope) it is 0.8 Å [O´K01b].

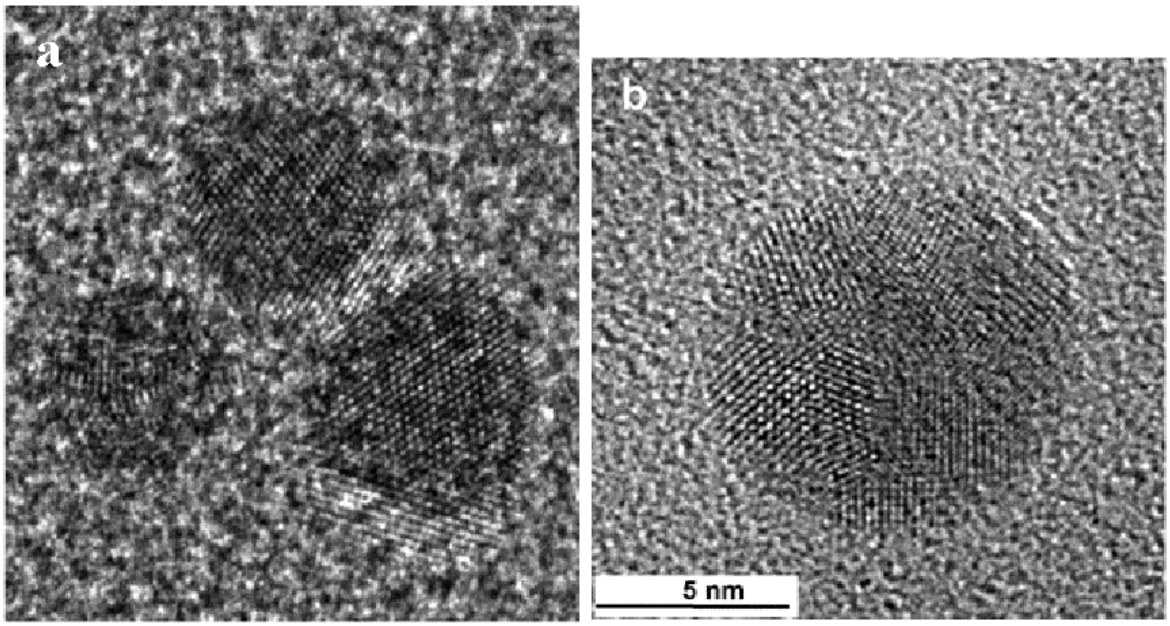


**Figure 2.2:** Image of Au particles on carbon support film. With an uncorrected objective lens (a) strong delocalization (fringe contrast outside the particles) is visible. In the $C_S$-corrected case (b) the delocalization has disappeared and the Au particle is imaged artifact free [Sch05].

### 2.1.3 Contrast Transfer Function

The optical system of the microscope transforms each point of the specimen into a disk[1] in the final image. This is described by the *point spread function* $h(\mathbf{r})$. The final image is a convolution of the point spread function with the specimen transmission function (exit wave) $f(\mathbf{r})$. The realspace convolution is difficult to treat mathematically. The problem is fourier transformed to the reciprocal space and the convolution becomes a simple multiplication. The Fourier transformed point spread function is the so called *contrast transfer function (**CTF**)* $H(\mathbf{k})$. $\mathbf{k}$ is the spatial frequency, sometimes in literature, e.g. [Wil96], also referred to as $\mathbf{u}$ or in chapter 2.1.4 as $\mathbf{G}$. The spatial frequency corresponds reciprocally to distances, high spatial frequencies mean small distances and vice versa. Therefore large spatial frequencies are needed for high resolution.
The following phenomena contributes to the CTF: apertures, attenuation of the wave and the aberration of the lens. They are described by the aperture function $A(\mathbf{k})$, the envelope

[1] The radius of the point spread area is given by [Lic91]:

$$\rho = -0.75 C_S \left(\frac{\mathrm{d}\chi}{\mathrm{d}\mathbf{k}}\right)_{max} \tag{2.2}$$

With the aberration function and phase distortion function respectively $\chi(\mathbf{k})$.

function $E(\mathbf{k})$ and the aberration function $B(\mathbf{k})$. The CTF can be written as following:

$$H(\mathbf{k}) = A(\mathbf{k})E(\mathbf{k})B(\mathbf{k}) \tag{2.3}$$

The aberration function is of an exponential form:

$$B(\mathbf{k}) = \exp(-i\chi(\mathbf{k})) \tag{2.4}$$

With the so called "phase grating" function $\chi(\mathbf{k})$ which has the form of a phase shift expressed as $\frac{2\pi}{\lambda}$ times the path difference traveled by the spherical aberration, defocus and astigmatism affected waves [Wil96]:

$$\chi(\mathbf{k}) = \pi\Delta f\lambda\mathbf{k}^2 + \frac{1}{2}\pi \mathrm{C_S}\lambda^3\mathbf{k}^4 \tag{2.5}$$

The former mentioned weak phase object approximation (WPOA), which uses a two dimensional projection of the crystal structure to represent the potential of the specimen, reveals that for a very thin specimen the amplitude of the transmitted wave function is linearly related to the potential [Wil96]. This approximation yields for the electron exit wave:

$$f(x, y) = 1 + i\sigma V_t(x, y) \tag{2.6}$$

where $V_t(x, y)$ is the projected potential in z-direction and $\sigma$ a interaction constant. Using this approximation, the correlation of the electron exit wave function with the CTF and the fact that the intensity is given by:

$$I = \psi\psi^* =\mid \psi \mid^2 \tag{2.7}$$

and neglecting terms in $\sigma^2$ because $\sigma$ is small, the following expression is obtained:

$$I = 1 + 2\sigma V_t(x, y) \otimes \sin(x, y) \tag{2.8}$$

This shows that only the imaginary part of the aberration function $B(\mathbf{k})$ contributes to the intensity so that equation 2.4 can be set to:

$$B(\mathbf{k}) = 2\sin(\chi(\mathbf{k})) \tag{2.9}$$

Using this expression for $B(\mathbf{k})$ a new function, the transfer function $T(\mathbf{k})$ can be defined:

$$T(\mathbf{k}) = A(\mathbf{k})E(\mathbf{k})2\sin(\chi(\mathbf{k})) \tag{2.10}$$

which is often called the contrast transfer function, too. This sinusoidal expression for the CTF is also used for the plots made with the CTF-explorer [Sid] in this thesis.

### Information limit

The information limit is a microscope-specific parameter and gives the maximum resolution which can be achieved with the instrument. It is defined as the spatial frequency from which the CTF oscillations are equal to the noise level and the envelope functions damp the CTF to zero, respectively [Sid].

### Point-to-point resolution

The point-to-point resolution for one defocus value is the spatial frequency or rather the resolution for which the corresponding CTF has its first node. Images with only smaller spatial frequencies[2] are directly interpretable since the contrast is of the same sign in that area. For spatial frequencies larger than the first-node value the contrast is not directly interpretable and image simulations are needed, see chapter 2.1.5. Negative values of the CTF and the phase transfer function respectively correspond to a positive phase contrast, which makes atom columns look dark and the background look bright, and vice versa for positive values [Sta03b]. The defocus which yields the largest point-to-point resolution is called *Scherzer defocus* and defines the point-to-point resolution of the microscope.

### Optimum defocus

Finding the optimum defocus is difficult. Equation 2.10 gives only one free parameter to optimize the CTF which is the defocus value. Which defocus is optimum depends on what is to be achieved. If one wishes as good a resolution as possible or if one wants directly interpretable images makes a difference in the choice of defocus. As described in the section 2.1.3 the Scherzer defocus given by equation 2.11 yields the best results for the direct interpretation of images but at the expense of the resolution.

$$\Delta f_{Scherzer} = -1.2\sqrt{C_S\lambda} \tag{2.11}$$

Especially for layerwise investigations of atom columns in nanoparticles it is necessary to have a resolution up to the information limit of the microscope which is not the case for working under Scherzer defocus conditions, see fig. 2.3 for the Scherzer defocus.
In [Lic91] Lichte presents some theoretical results concerning the optimum focus for taking

[2] which can be achieved by using apertures to cut the larger spatial frequency values

electron holograms. He found an optimum defocus for the desirable value of the maximal spatial frequency, the information limit. His calculation includes the assumption that by subsequent reconstruction the aberrations of the objective lens will be corrected. This optimum defocus value is nowadays known as the *Lichte defocus* and given by:

$$\Delta f_{Lichte} = -0.75 C_S (k_{max}\lambda)^2 \tag{2.12}$$

The idea of his investigations was to minimize the derivative $\frac{\mathrm{d}\chi}{\mathrm{d}\mathbf{k}}$ and to choose the defocus values which minimizes the maximum value of the modulus of the derivative of the wave aberration function $\chi(\mathbf{k})$ respectively [Lic91], for the spatial frequency interval of interest $(0 - \mathbf{k}_{max})$. This corresponds to minimizing the radius of the point spread area, as can be seen in equation 2.2.

Summing up this section there is to say that the Lichte defocus is the best in terms of obtaining the highest info limits while the Scherzer defocus yields the best point-to-point resolution. The problem of the Scherzer defocus is the number of nodes of the CTF which mean no contribution of the corresponding spacial frequencies to contrast. Full recovery of the information is possible by acquiring a so called *focal series* which is explained in section 2.2.2.

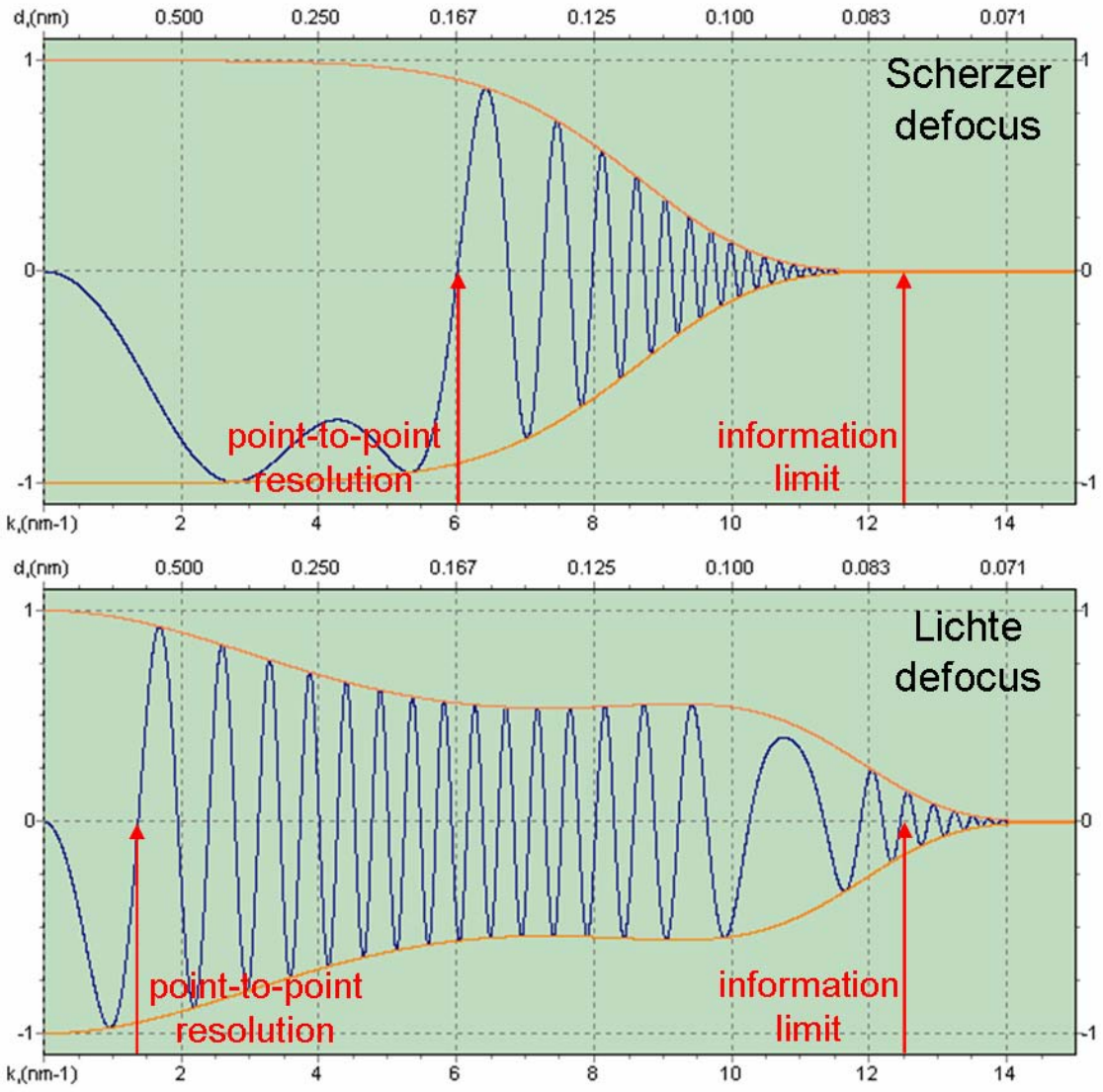


**Figure 2.3:** Scherzer and Lichte defocus for the CM300 microscope. The upper x-axis gives the real space dimension in nm.

### 2.1.4 Sample Wave Interaction - HR-TEM Image Formation

Interpreting HRTEM-images is not easy, because in most cases the images are anything but a direct structure representation of the sample. Due to the interaction of the electrons with the specimen a complicated interference pattern of diffracted electron beams and the central beam $\phi(\mathbf{G})$[3] is formed which includes linear and non-linear effects. This short theoretical overview is adapted from [Coe96] and [Ish80] and uses the same notation as in the EWR-chapter 2.2.2. A more detailed theoretical discussion of image formation can be found elsewhere, e.g.[Wil96, Rei84].

According to [Ish80] the diffracted electron beams result in the spatially varying image intensity in the image plane with the general Fourier components I($\mathbf{G}$). $\mathbf{G}$ is the two-dimensional spacial frequency vector. Under isoplanatic imaging conditions and with T, the transmission-cross-coefficient, I($\mathbf{G}$), the image intensity fourier coefficient, is given by:

$$\mathrm{I}(\mathbf{G}) = \int \phi(\mathbf{G}+\mathbf{G}')\phi^*(\mathbf{G}')\mathrm{T}(\mathbf{G}+\mathbf{G}',\mathbf{G}')\mathrm{d}\mathbf{G}' \tag{2.13}$$

Eq.2.13 can be treated separately for the two cases $\mathbf{G} \neq 0$ ("ac"-component) and $\mathbf{G} = 0$ ("dc"-component[4]).

$$\mathrm{I}(\mathbf{G}=0) = \int |\phi(\mathbf{G}')|^2 \mathrm{d}\mathbf{G}' \qquad \text{"dc" component} \tag{2.14}$$

$$\begin{aligned}\mathrm{I}(\mathbf{G}\neq 0) = {} & \phi(0)\phi^*(-\mathbf{G})\mathrm{T}(0,-\mathbf{G}) + \phi^*(0)\phi(\mathbf{G})\mathrm{T}(\mathbf{G},0) \\ & + \int_{\mathbf{G}'\neq 0;\mathbf{G}'\neq -\mathbf{G}} \phi(\mathbf{G}+\mathbf{G}')\phi^*(\mathbf{G}') \\ & \times \mathrm{T}(\mathbf{G}+\mathbf{G}',\mathbf{G}')\mathrm{d}\mathbf{G}' \qquad \text{"ac" component}\end{aligned} \tag{2.15}$$

$\phi(\mathbf{G}=0)$ is the transmitted electron beam and $\phi(\mathbf{G}\neq 0)$ is one of the diffracted beams. While in equation 2.15 in the first two terms the information of the linear interferences between the transmitted electron beam with one diffracted electron beam is given, the third term accounts for non-linear interferences between diffracted electron beams. The

[3] note that the spatial frequency $\mathbf{G}$ was denoted by $\mathbf{k}$ in chapter 2.1.3

[4] spatially constant, non varying

Transmission-Cross-Coefficient (TCC) takes into account aberrations and coherence effects and is expressed by:

$$\mathrm{T}(\mathbf{G_1},\mathbf{G_2}) = \mathrm{p}(\mathbf{G_1})\mathrm{p}^*(\mathbf{G_2})\mathrm{E}_\Delta(\mathbf{G_1},\mathbf{G_2})\mathrm{E}_\mathrm{S}(\mathbf{G_1},\mathbf{G_2}) \tag{2.16}$$

with $\mathrm{p}(\mathbf{G})$ denoting the pure phase transfer function (PTF) equation 2.17, $\mathrm{E}_\Delta$ and $\mathrm{E}_\mathrm{S}$ being envelopes for temporal ($\delta$) and spatial ($S$) coherence. $\mathrm{E}_\Delta(\mathbf{G_1},\mathbf{G_2})$ is influenced by the defocus of the objective lens ($\Delta f$) and the "focal spread" parameter ($\Delta$) whereas $\mathrm{E}_\mathrm{S}(\mathbf{G_1},\mathbf{G_2})$ is dependent on the electron wavelength $\lambda$ and $\alpha$ denotes half the angle of beam convergence.

$$\mathrm{p}(\mathbf{G}) = \exp[-2\pi\mathrm{i}\chi(\mathbf{G})] \tag{2.17}$$

$\chi(\mathbf{G})$ is the aberration function of the electron wave. It describes phase distortions due to the spherical aberration, represented by the aberration coefficient $C_S$, and the defocus value $\Delta f$:

$$\chi(\mathbf{G}) = \frac{1}{2}\Delta f\lambda\mathbf{G^2} + \frac{1}{4}\mathrm{C_S}\lambda^3\mathbf{G^4} \tag{2.18}$$

This expression is also known from chapter 2.1.3. Specially for a FEG-TEM according to its high spatial coherence $\mathrm{T}(\mathbf{G_1},\mathbf{G_2})$ can be factorized, so that:

$$\mathrm{T}(\mathbf{G_1},\mathbf{G_2}) \approx \mathrm{t}(\mathbf{G_1})\mathrm{t}^*(\mathbf{G_2})\mathrm{E}_\Delta(\mathbf{G_1},\mathbf{G_2}) \tag{2.19}$$

with $\mathrm{t}(\mathbf{G})$ being the effective transfer function (product of pure transfer function and the linear envelope function):

$$\mathrm{t}(\mathbf{G}) = \mathrm{p}(\mathbf{G})\mathrm{E}_\mathrm{S}(\mathbf{G},0) = \exp[-2\pi\mathrm{i}\chi(\mathbf{G})] \times \left[-\left(\frac{\pi\alpha}{\lambda}\right)^2[\nabla\chi(\mathbf{G})]^2\right] \tag{2.20}$$

For this factorization approximations had to be made. There occurs an error for most of the non-linear interferences, which can be neglected for a FEG due to not causing huge offset errors in the model used for the image reconstruction. For larger values of $\alpha$ this approximation has to be improved.

There is also blurring of the image due to the detection process. To model this effect a damping function is used which acts on the frequency components of the ideal image intensity. This "damping envelope" is given by 2.21. $\mathrm{I}^\mathrm{D}(\mathbf{G})$ is the modelled image intensity for all blurring aspects. Those of the detection process are the modulation transfer function

of the detector (CCD camera) M($\mathbf{G}$) and two envelopes for vibration V($\mathbf{G}$) and drift D($\mathbf{G}$) of the sample during the image acquisition.

$$I^D(\mathbf{G}) = E_I(\mathbf{G})I(\mathbf{G}) \tag{2.21}$$

$$E_I(\mathbf{G}) = M(\mathbf{G})V(\mathbf{G})D(\mathbf{G}) \tag{2.22}$$

### 2.1.5 Image Simulation

For reasonable HR-TEM-image interpretation it is absolutely necessary to do image simulation (see also [Dmi03]), i.e. all possible models of the structure have to be simulated by computers. Comparing the simulated images with the experimental data will help to find the real structure of the sample. But this is to be considered very carefully. Only if really all thinkable model-structures have been simulated as well as the simulation parameters have been chosen very sensibly, the right interpretation of the HRTEM-images becomes possible. It is also a good idea to match simulation and experimental data for different orientations.

#### Different approximations

The scattering behavior of an electron wave propagating through a crystal structure is fully described by the Schroedinger equation. Since it is still difficult to solve even in the so called forward scattering approximation, Cowley and Moodie (1957) developed the Multislice Method which is much more elegant [Cow57]. There also exists another approximation in terms of Bloch waves. Here the electron wavefunction as a function of the reciprocal space vector $\mathbf{k}$ is written as a linear combination of Bloch waves b($\mathbf{k}, \mathbf{r}$) with coefficients $\varepsilon$ (Howie, 1963 [How63]). Each Bloch wave is itself expanded into a linear combination of plane waves which reflect the periodicity of the crystal potential. That leads to a set of linear equations to be solved. The Bloch wave approximation can be characterized as follows:

- Easy accounting of reflections outside the zero order Laue zone, but also requires exact specification of which reflections g are included in the calculation.
- Very good for perfect crystals, but not suited for calculating images from defects.
- Validity of the solution for a particular specimen thickness.
- Dynamical scattering is included.

- Allows rapid calculation of convergent beam electron diffraction patterns.

### The Multislice Approximation

The idea of the Multislice Method is to "cut" the sample perpendicular to the incident electron beam into slices. For every slice the crystal potential is projected to a plane. Thus the electron wavefunction is calculated at $z+n*dz$ by taking the output of one calculation as the input of the next one.

$$\Psi(x,y,z+\mathrm{d}z) \approx \exp[-i\sigma \mathrm{d}z \nabla^2_{x,y}] \cdot \exp[-i\sigma \int_z^{z+\mathrm{d}z} V(x,y,z^{'})\mathrm{d}z^{'}]\Psi(x,y,z) \tag{2.23}$$

This equation is solved in a two step process. The potential due to the atoms in a slice dz is projected onto the plane $t = z$, giving rise to a scattered wavefield:

$$\Psi_1(x,y,z+\mathrm{d}z) = \exp[-i\sigma \int_z^{z+\mathrm{d}z} V(x,y,z^{'})\mathrm{d}z^{'}]\Psi(x,y,z) \equiv q(x,y)\Psi(x,y,z) \tag{2.24}$$

where the function $q(x,y)$ is referred to as the phasegrating.
The wavefield is propagated through vacuum to the plane $t = z + dz$:

$$\Psi(x,y,z+\mathrm{d}z) = \exp[-i\sigma \mathrm{d}z \nabla^2_{x,y}] \cdot \Psi_1(x,y,z) \tag{2.25}$$

This equation being a convolution in real space is therefore transformed to the Fourier space:

$$\Psi(\mathbf{H},z+\mathrm{d}z) = \exp[-i\pi\lambda \mathrm{d}z \mathbf{H^2}] \cdot \Psi_1(\mathbf{H},z) \equiv p(\mathbf{H},\mathrm{d}z) \cdot \Psi_1(\mathbf{H},z) \tag{2.26}$$

with $\Psi(\mathbf{H},z)$ being the Fourier coefficients and the so called propagator $p(\mathbf{H},\mathrm{d}z)$. A repeated use of the last two equations defines the multislice formalism giving the wavefield at any arbitrary thickness T of the specimen.

### Image formation

In this section the image formation by a simulation Software is described in accordance to [Kila]. Only the first lens of the microscope, the objective lens, is considered in the simulation calculations. All the other lenses just magnify the image formed by the objective lens. Since the angle which the electrons form with the optic axis of the lens varies inversely with the magnification, only the aberrations are important. Without any aberrations,

instabilities and with the specimen in the focal plane of the objective lens, the image observed in the microscope would be a magnified version of:

$$I(x,y) = |\Psi(x,y,z = exitplane\ of\ specimen)|^2 = \Psi_e(x,y)\Psi_e^*(x,y) \tag{2.27}$$

Normally, the following effects are included in the calculation:

- spherical aberration
- chromatic aberration
- lens defocus
- *considered correctable by the operator, but can also be included in the equations:*
  - two-fold astigmatism
  - three-fold astigmatism
  - axial coma

Considering only spherical aberration and defocus of the objective lens, the image would be obtained as follows:

1. Calculate the wavefield emerging from the specimen according to one of the approximations.
2. Fourier transform the wavefield which gives the amplitude and phase of scattered electrons.
3. Add the phase shift introduced by the lens defocus and the spherical aberration to the Fourier coefficients.
4. Inverse Fourier transform to find the modified wave function.
5. Calculate the image as the modulus square of the wavefield.

However there are two more effects concerning variations in electron energy and direction to be considered: *chromatic aberration/temporal incoherence* and *beam divergence/spatial incoherence*. The *chromatic aberration* causes electrons of different energies to focus on different planes. Therefore a Gaussian spread in defocus is assumed in the calculation which leads to a damping of each Fourier term (diffracted beam). Another damping of the diffracted beam occurs due electrons not proceeding parallel to one another, thus forming a cone of an angle $\alpha$. This leads to a disk instead of a point in the diffraction pattern.

### Stobbs factor

The *Stobbs factor* is a factor describing the ratio of contrast in simulated and experimental images and is defined as follows:

$$Stobbs\ factor = \frac{contrast\ in\ simulated\ image}{contrast\ in\ experimental\ image}$$

The typical value of the Stobbs factor is 3. Still nowadays the origin of this big difference is not explained and under intensive investigation. There were some thoughts including a frozen phonon approach yielding results which were even worse according to the experimental data. C. B. Boothroyd ascertains the problem, see [Boo00] for example. He has also performed some investigations on phonon scattering influencing the experimental measured intensity. There are 2 methods to get access to phonon scattering. They are described in [Boo03] and in [Boo05]. Summarizing those experiments yielded an influence of $10 - 15\%$ which does not explain the discrepancy between simulated and experimental images either. According to Boothroyd there must be other reasons for the Stobbs factor which he sees in the part dealing with microscope parameters of simulation calculations.

## 2.2 Different Applications of HR-TEM

Transmission Electron Microscopy offers many possibilities of characterizing materials. In this thesis the so called CTEM (Conventional Transmission Electron Microscopy) was mainly used. For the chemical analysis the analytical TEM (ATEM) is used which employs the techniques of electron energy loss spectroscopy (EELS) and the energy dispersive x-ray spectroscopy (EDS). EDS is a common method to characterize thin films and particles by element specific energy spectra generated by X-rays from scattering processes of the electron beam-sample interaction. In the electron energy loss spectroscopy (EELS) the energy of the inelastic scattered electrons is detected.
Since the aim of this thesis was to analyze the lattice structure of the FePt-nanoparticles lattice imaging had to be processed which means HR-TEM had to be done. As described in 2.1.4 aberrations and delocalization effects (2.1.3) influence the image and have to be considered when interpreting the results. So the goal was to find a way of minimizing this disturbing effects but simultaneously to maximize the information. The maximum information is obtained when the amplitude and phase of the electron is detected. And the maximum also means to extend your information up to the limit of the microscope, the information limit (2.1.3) which is given by mechanical limitations of the microscope. So the

idea of Exit Wave Reconstruction was born. Because HR-TEM images only show a two-dimensional projection of the sample, it is not possible to get any three-dimensional (3D) shape information. Hence another technique is necessary: 3D-Tomography (e.g. [Bal06]).

### 2.2.1 Quantitative HR-TEM

The Z-contrast is the dependence of the image "intensity" from the atomic number Z($I \sim Z^2$). That means "heavier" atoms contribute more to contrast than "lighter" atoms. In TEM the Z-contrast is usually used in the Scanning Transmission mode (STEM - Scanning Transmission Electron Microscope) because in this mode the beam is focused to a single spot of the sample. In HR-TEM a parallel illumination is used. If Scherzer imaging is applied atom columns appear black in HR-TEM while they appear white in STEM. With the introduction of EWR the phase problem was solved and a quantitative interpretation of image intensities became possible in HR-TEM.

Fig. 2.4 shows the Z-dependence of the signal/noise ratio for HR-TEM and STEM for single atoms. It is clear that HR-TEM exhibits a larger signal/noise ratio over the whole Z-range. In 2002 one could expect to detect single atoms in HR-TEM for Z larger than 2 and STEM single atoms with Z larger than 40. The strength of STEM is a better discrimination of atoms with different Z. The current development of hardware $C_C$ and $C_S$ correctors in essence aims at an improvement of signal/noise ratios (detection limits) for STEM and HR-TEM.

In STEM the chemical sensitivity originates from Rutherford scattering. In HR-TEM the origin of chemical sensitivity is illustrated in fig. 2.5. There the zero beam is plotted as a function of sample thickness and for different elements of atomic number Z. An identic cubic structure is considered in all cases. It is seen that the beam intensity oscillates with sample thickness. The periodicity of these oscillations is called extinction distance. The extinction distance decreases with increasing Z. Moreover, gray values repeat periodically as a function of sample thickness and uniqueness requirements make it often necessary to restrict measurements to a thickness limited by the first extinction oscillations. Please note that in crystals made from heavy materials this thickness can be very small.

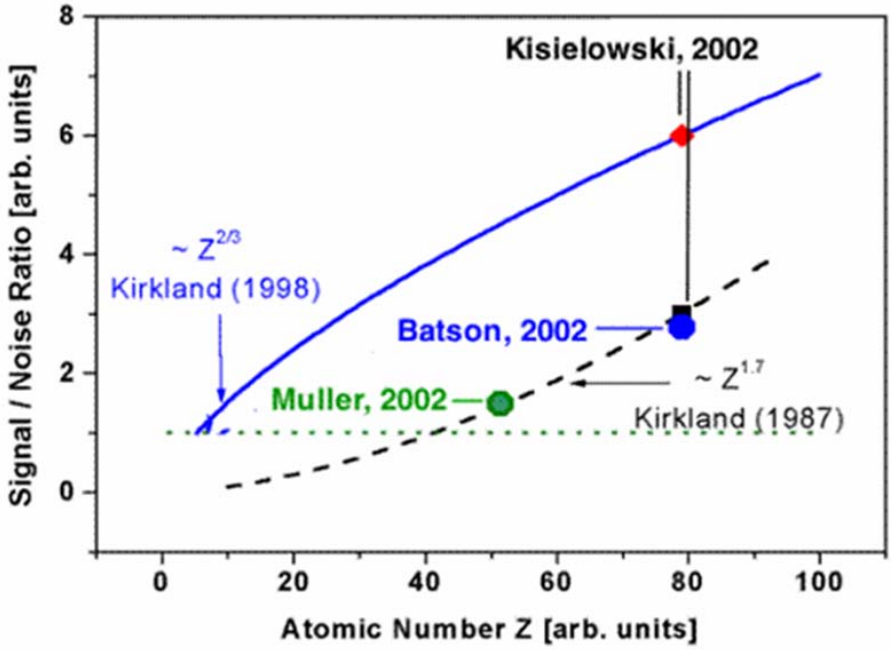


**Figure 2.4:** Sensitivity of Exit Wave Reconstruction (diamond), and HAADF imaging for the detection of single atoms with atomic number Z (13). A signal to noise ratio of 1 is considered to be the detection limit [Kis02].

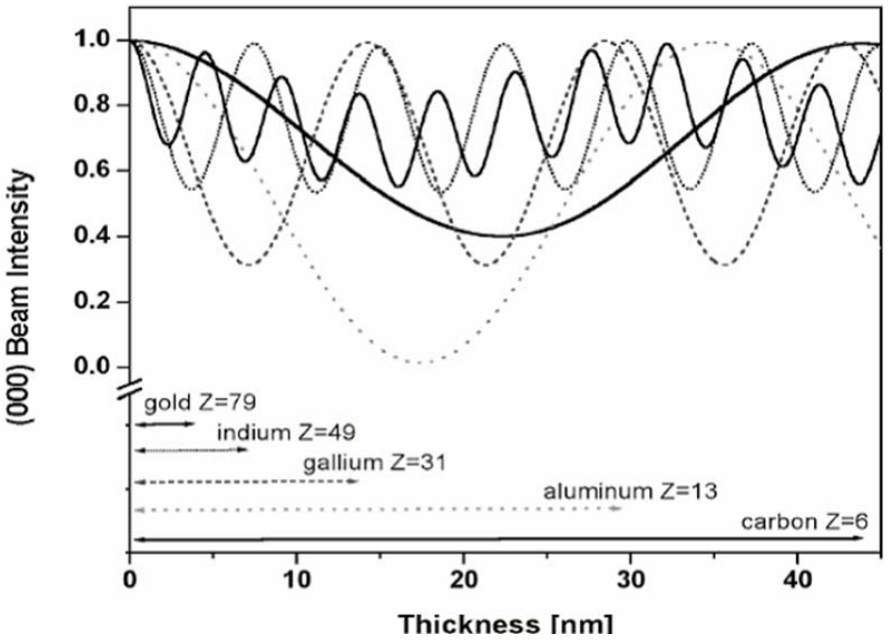


**Figure 2.5:** Zero beam intensity versus sample thickness of a fcc crystal with lattice parameter a=0.4 nm and lattice sites occupied by the indicated elements [Kis02].

### 2.2.2 Exit Wave Reconstruction

The idea of *Exit Wave Reconstruction* is to remove all the blurring effects in the exit wave caused by the imaging system of the microscope and to reconstruct the "image" directly below the sample. This task requires a physical description of the model "reconstruction" and also demands to reconstruct from a series of intensity images the amplitude and phase contrast of the exit wave. In the intensity image, given through $\Psi^2$, the phase and amplitude information is completely lost. The most important work enabling a complete reconstruction of the Exit-Wave was done by Kirkland [Kir84] and Thust [Thu96],[Coe96].

#### Why focal series acquisition?

For Exit-Wave-Reconstruction the acquisition of a focal-series is required. But why is this the way of choice to recover the complete electron exit wave information and what is a focal series? The Contrast Transfer Function is "responsible" for the information transfer from the Exit-Wave of the sample to the image as already discussed in 2.1.3. The problem is, that the CTF oscillates heavily for higher spatial frequencies, especially for the microscopes using a Field Emission Gun (FEG). And those oscillations mean no spatial frequency information for the crossing points with the x-axis. To recover all spatial frequencies and the full phase information a series of images must be recorded with different focus settings. Focal series means a series of images taken under identical conditions in the microscope apart from the defocus value which is changed by a small fixed amount for every acquisition. As shown in 2.6 changing the defocus value by 4 nm only causes a slight shift of the CTF for the higher spatial frequencies. For a shift in the low frequency area the defocus change has to be larger. 2.7 shows 3 direct comparisons of a -270 nm defocus with -2 nm, +10 nm and +20 nm deviating defocus values. It is easy to see that a defocus change of 20 nm only leads to a slight change of the lower spatial frequencies. Therefore it is necessary to use a larger defocus range, e.g. 40 nm. With a defocus step of 2 nm this leads to a series of 20 images which is a typical number. Due to the fact that the delocalization effects 2.1.2 are smallest for the Lichte-defocus as shown in 2.1.3 it is consequentially that a focal series is taken around Lichte-defocus. For the CM300-microscope which was used for my investigations Lichte-defocus is -273 nm and that is why the defocus values in 2.6 and 2.7 are chosen around -270 nm. According to [Kis06a] other defocus values were discussed in order to extend the resolution. Both an aberration free defocus and an alpha-null defocus were suggested to optimize information transfer for Exit Wave Reconstruction [O'K01a]. However, there were many obstacles like inability to predict image Fourier components for non-periodic structures and huge image delocalization which still make the Lichte defocus

the best for focal series recording.

### Different methods of image processing

The imaging process can be considered approximately linear for very thin samples. For this linear model a closed form image reconstruction solution exists. On the other hand, for thicker samples it is necessary to work with a non-linear model. Kirkland presented in [Kir84] a method of nonlinear image reconstruction from a defocus series which is based on the maximum a-posteriori method (MAP) of image restoration. But this method only works with one image. Kirkland names his new method multiple input MAP (MIMAP). It provides refining of the defocus values, translational alignment of the images of the series and is general enough to improve the non-linear partial coherence reconstruction theory for which a approximate formulation has been published before. In [Kir84] two different approaches to the MIMAP reconstruction are discussed: one using fast fourier transforms (FFT) based on an approximation to the spatial coherence which uses less computer time; the other one is more precise but therefore it needs much more computer time. In Kirkland's MIMAP method a least-square functional is minimized and so the electron wave is matched to the measured intensities of the focal-series. Based on his pioneering work in the area of non-linear image reconstruction improved versions have been developed by Coene at al. [Coe96]. This was necessary because it was demonstrated that MIMAP only worked for a few images of a very limited frame size. Another disadvantage was the long computation time due to the 50-100 iterations which are necessary to reach convergence. The method developed by Coene et al. is called maximum-likehood method (MAL). It uses a least-square functional similar to the one in MIMAP. The difference between the two methods is a noise-control term containing a priori information on the wave function which is used in MIMAP but not in MAL. The coupling of the wave function and its complex conjugate (in HR-TEM image formation and the exit wave reconstruction)is also considered in the MAL approach . Another item deals with the optimization of the numerical implementation for large frame sizes which are typical for slow scan CCD cameras ($512 \times 512\ pixel^2, 1024 \times 1024\ pixel^2$). A large frame size of the images is necessary because a real space sampling interval of sub angstrom size is required. That leads to a field of view of 12nm in a frame of $512 \times 512\ pixel^2$. Also not to be neglected is the influence of the point-spread function which effects a smaller effective field of view. In addition to the MAL-approach which was developed in the BRITE-EURAM project there exists another concept also developed in the same project. This so-called paraboloid concept deals with the linear processing of the reconstruction but yields two improvements compared to former

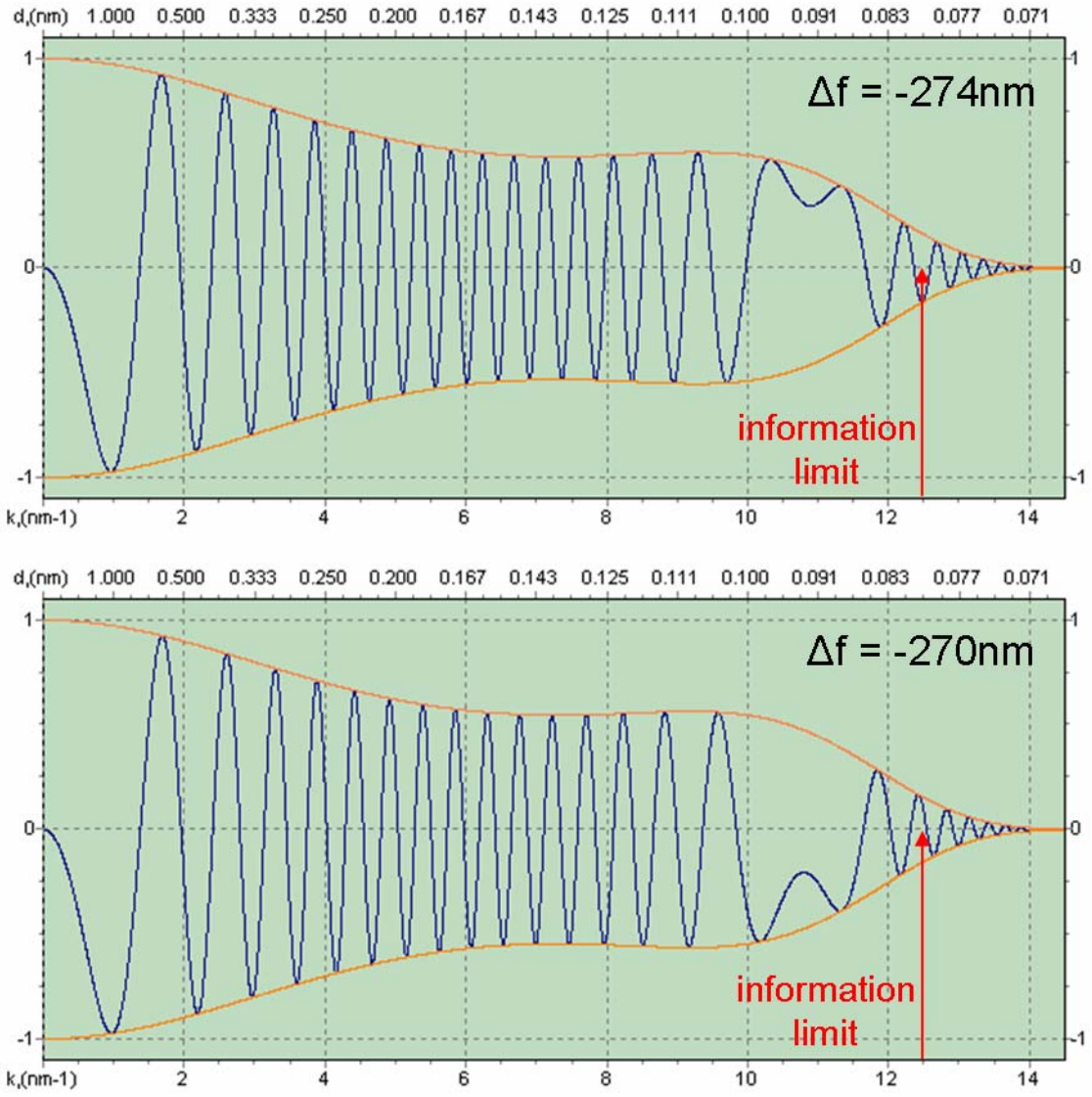


**Figure 2.6:** CTF for two different defocus values. Plotted with CM300 parameters. The red arrow indicate the information limit of the CM300. The spatial frequency **k** is the same as one denoted with **G** in the text. The upper x-axis gives the real space dimension in nm.

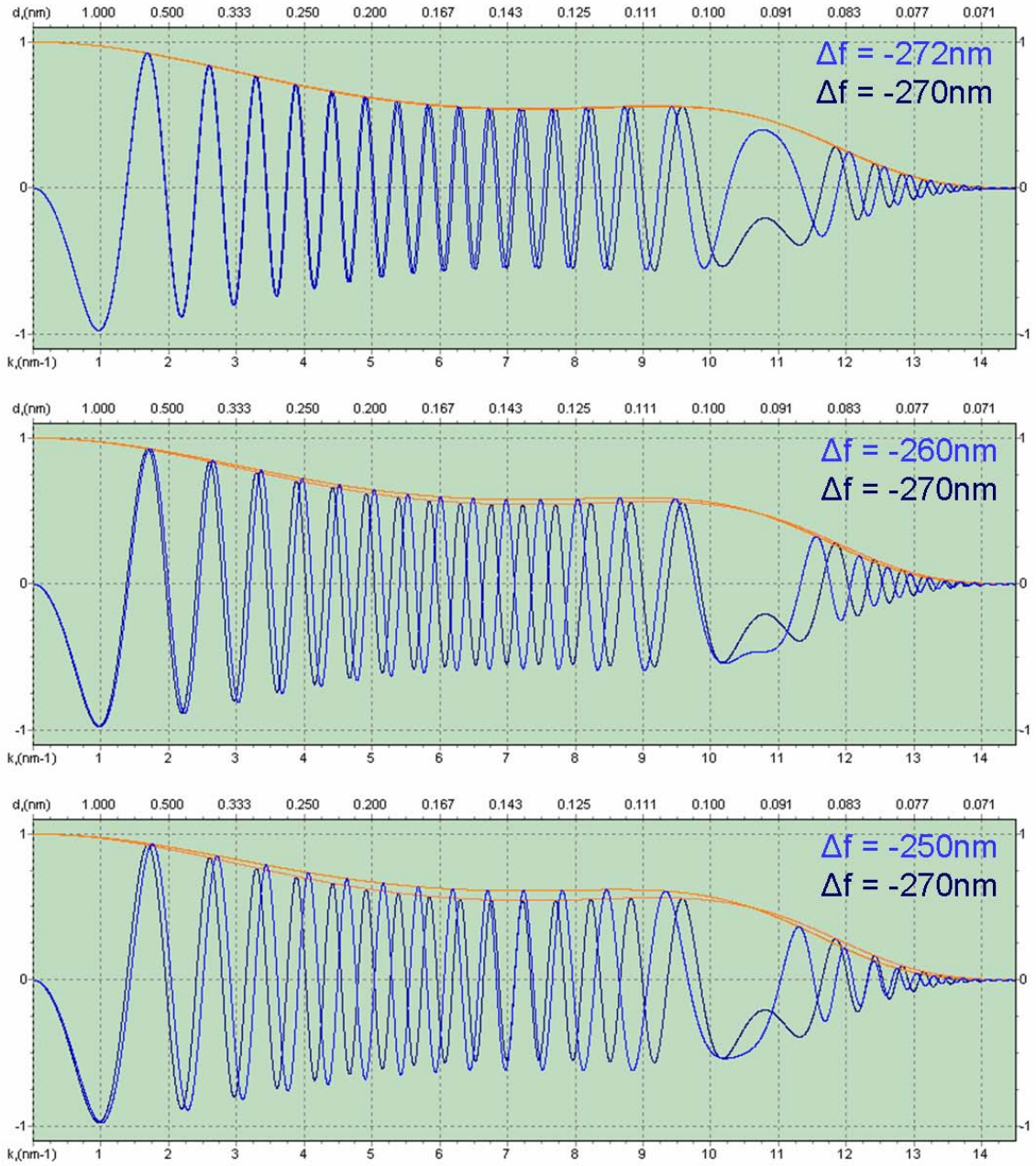


**Figure 2.7:** Comparisons of the CTF for a defocus of -270 nm and -272 nm, -260 nm and -250 nm. Plotted with CM300 parameters. One should note how sensitive the CTF reacts for spatial frequencies $\mathbf{G} = \mathbf{k} > 0.14$.

linear approaches for which a strong beam had to be assumed: (i) weighting linear and non-linear terms properly leads to a constant determination of the beam amplitude (ii) treating of non-linear terms as a perturbation $\longrightarrow$ recursive application of the linear reconstruction scheme. This paraboloid method (PAM) also known as "Van Dyck method" is related to early work by Saxton whereas the maximum-likehood method is based on Kirkland's work as elucidated before. According to Coene [Coe96] the reconstruction performance of MAL is superior to that of PAM.

In 2.8 a typical "mean squared difference" convergence plot is shown as a function of the number of iterations. It points out that a combination of PAM and MAL leads to the best results concerning convergence and iteration time. The advantage of PAM is that it converges very fast, MAL on the other hand allows for a better solution because this method uses all information of the images optimally. Using only the MAL iterations would require many more iterations to get the same result than the combination of both yields [Dyc96].

### The MAL method

HRTEM image reconstruction is used to calculate the electron wave $\phi$ at the specimen exit plane. This is usually done by minimizing an error functional over a focal series of N images.

$$S^2 = \frac{1}{N}\sum_{n=0}^{N-1}\int \mathrm{d}\mathbf{G}|\delta I_n(\mathbf{G})|^2 \tag{2.28}$$

The mean-squared error $S^2$ of the estimated images with respect to the experimental images is given by equation 2.28. $\delta I_n(\mathbf{G})$ is the image difference for the n$th$ focal image $(n = 0, ..., N-1)$. With $I_{n,E}$, the intensity of the experimental and $I_{n,\phi}$, the intensity for a particular estimate of the electron wave $\phi$ simulated n$th$ focal image:

$$\delta I_n(\mathbf{G}) = I_{n,E}(\mathbf{G}) - I_{n,\phi}(\mathbf{G}). \tag{2.29}$$

The recursive minimization process is based on the gradients of $S^2$ with respect to the related Fourier components of the electron wave. Hereby $\phi(\mathbf{G})$ and $\phi^*(-\mathbf{G})$ are equivalent to $\phi^*(\mathbf{G})$ and $\phi(-\mathbf{G})$. The gradients are formally written as follows:

$$\mathrm{g}(\mathbf{G}) \equiv \nabla_{\phi^*(\mathbf{G})}\mathrm{S}^2 \tag{2.30}$$

$$\mathrm{g}^*(-\mathbf{G}) \equiv \nabla_{\phi(-\mathbf{G})}\mathrm{S}^2 \tag{2.31}$$

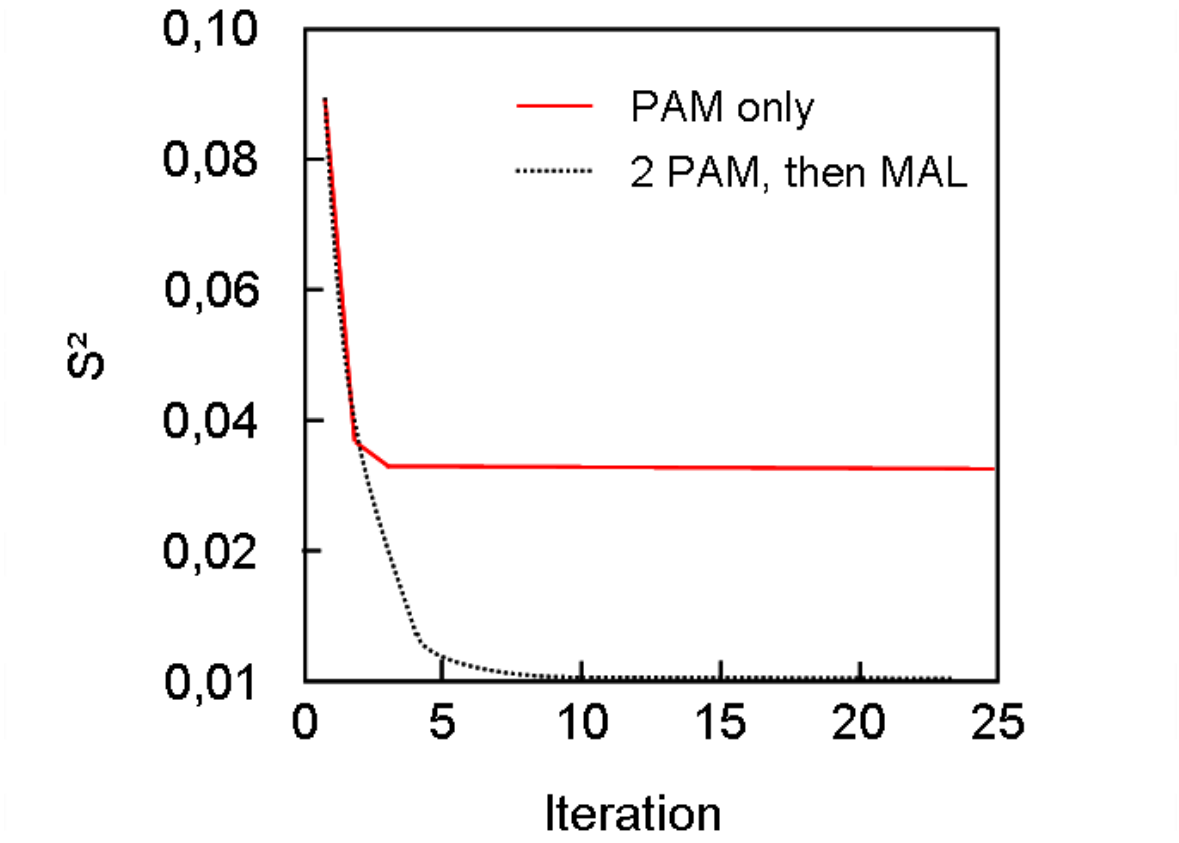


**Figure 2.8:** Convergence of a simulation experiment of $YBa_2Cu_4O_8$ with parameters for a 200kV FEG-TEM. The full line shows the convergence for only PAM iterations, the black dashed line indicates the convergence for the first and second PAM-iterations and followed by MAL (after [Dyc96]).

For minimizing $S^2$ eq. 2.30 and eq. 2.31 have to be zero. With the estimated image intensity from eq. 2.16 and eq. 2.21 one obtains from eq. 2.30 [Coe96]. This leads to the MAL-equations which are written as:

$$0 = \sum_{n=0}^{N-1} \int \mathrm{d}\mathbf{G}^{'} \mathrm{T}_n(\mathbf{G}^{'}, \mathbf{G}) \phi(\mathbf{G}') \delta I_n(\mathbf{G} - \mathbf{G}^{'}) \times \mathrm{E}_{I,n}(\mathbf{G} - \mathbf{G}^{'}) \tag{2.32}$$

$$0 = \sum_{n=0}^{N-1} \int \mathrm{d}\mathbf{G}^{'} \mathrm{T}_n(-\mathbf{G}, -\mathbf{G}^{'}) \phi^*(-\mathbf{G}') \times \delta I_n(\mathbf{G} - \mathbf{G}^{'}) \mathrm{E}_{I,n}(\mathbf{G} - \mathbf{G}^{'}) \tag{2.33}$$

This MAL-equations determine how $\delta I_n$, the difference between an experimental and an estimated image, has to be fed back to the starting point to obtain an optimized reconstructed electron wave $\phi$.
Figure 2.9 shows the recursive scheme of the MAL procedure for one iteration step $j \longrightarrow j+1$. The input are $\mathrm{N}(0 \cdots N-1)$ images of a focal series. The output is the reconstructed electron exit wave $\phi^{final}$ after convergence has been reached. For a more mathematical information concerning the minimization of the least square functional [Coe96](section 4) is the article of interest. The MAL-procedure for one feedback step can be described as follows:

1. HR-TEM-images are simulated with the parameters of the microscope: e.g. defocus spread, have to be well-known.
   $\Longrightarrow$ estimated image $I_{n,\phi}$ ($I_{n,j}$ for $j$th iteration) is received.

2. Comparison of estimated($I_{n,j}$) and experimental ($I_{n,E}$) images.

3. Image differences $\delta I_{n,j}$ are computed
   $\Longrightarrow$ tranformation of $\delta I_{n,j}$ to a correction $\delta\phi^j$ for the specimen wave $\phi^j$

4. update to $\phi^{j+1}$

5. ... repetition of $1. - 4.$ (one feedback-loop), if convergence is reached $\Longrightarrow 6.$

6. stop of iteration processing $\Longrightarrow$ output of $\phi^{final}$

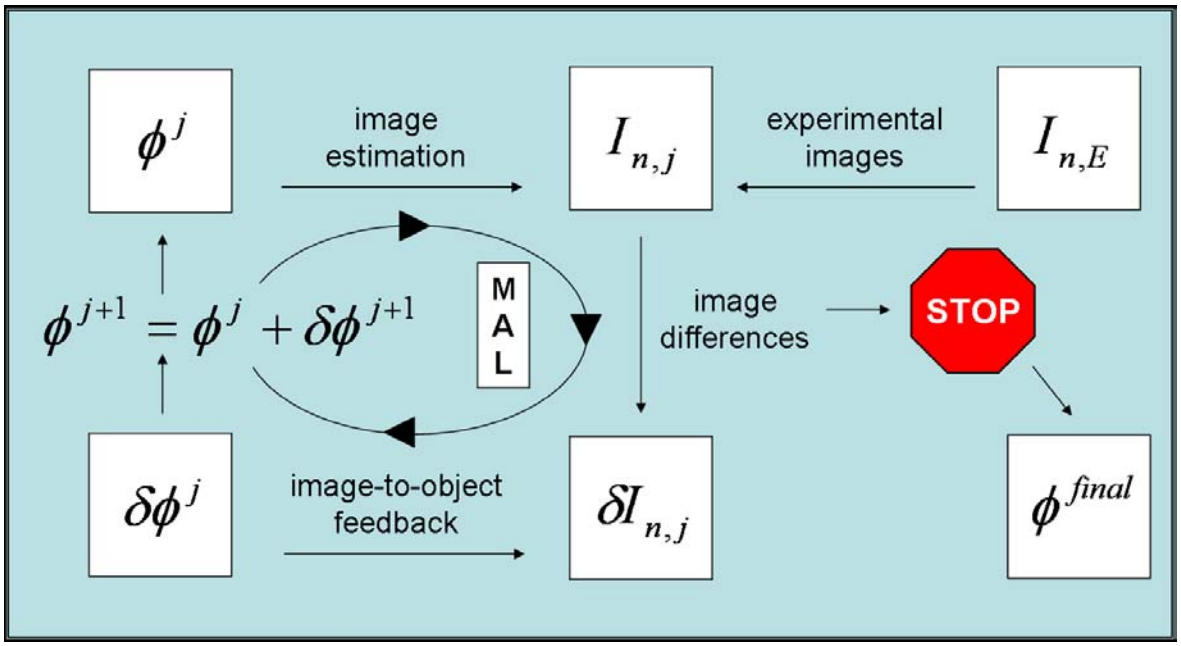


**Figure 2.9:** This graphic is in conformity to [Coe96]. Represented is one iteration circle $j \longrightarrow j+1$ of the MAL method for HRTEM image reconstruction. $\phi^j$ is the electron exit wave at the start (j) and $\phi^{j+1}$ at the end of this cycle.

### Some remarks on the paraboloid (PAM) method

The PAM-is a special case of the so called SC-MAL (self consistent-MAL) method, which is a special treatment of the MAL-equations. It is described by:

$$c_0\phi^1(\mathbf{G}) = \frac{1}{N}\sum_{n=0}^{N-1} \mathrm{F}_n(\mathbf{G})\mathrm{I}_{n,E}(\mathbf{G}) \tag{2.34}$$

$c_0$ is a value of the central Fourier component of the electron wave. A comparison between linear and expected non-linear terms allows for the determination of $c_0$. In this case only "dc" information in the initial electron wave is used. Herein the filter functions $\mathrm{F}_n(\mathbf{G})$ are applied to the experimental image intensities. All in all this is only a good approximation for thin samples, though. This was already mentioned in 2.2.2 when discussing linear approximation approaches.

Another method which yields information on the phase retrieval is the off-axis holography explained in [Dyc96].

### Necessity of EWR and conclusion

Exit Wave Reconstruction enables the following:

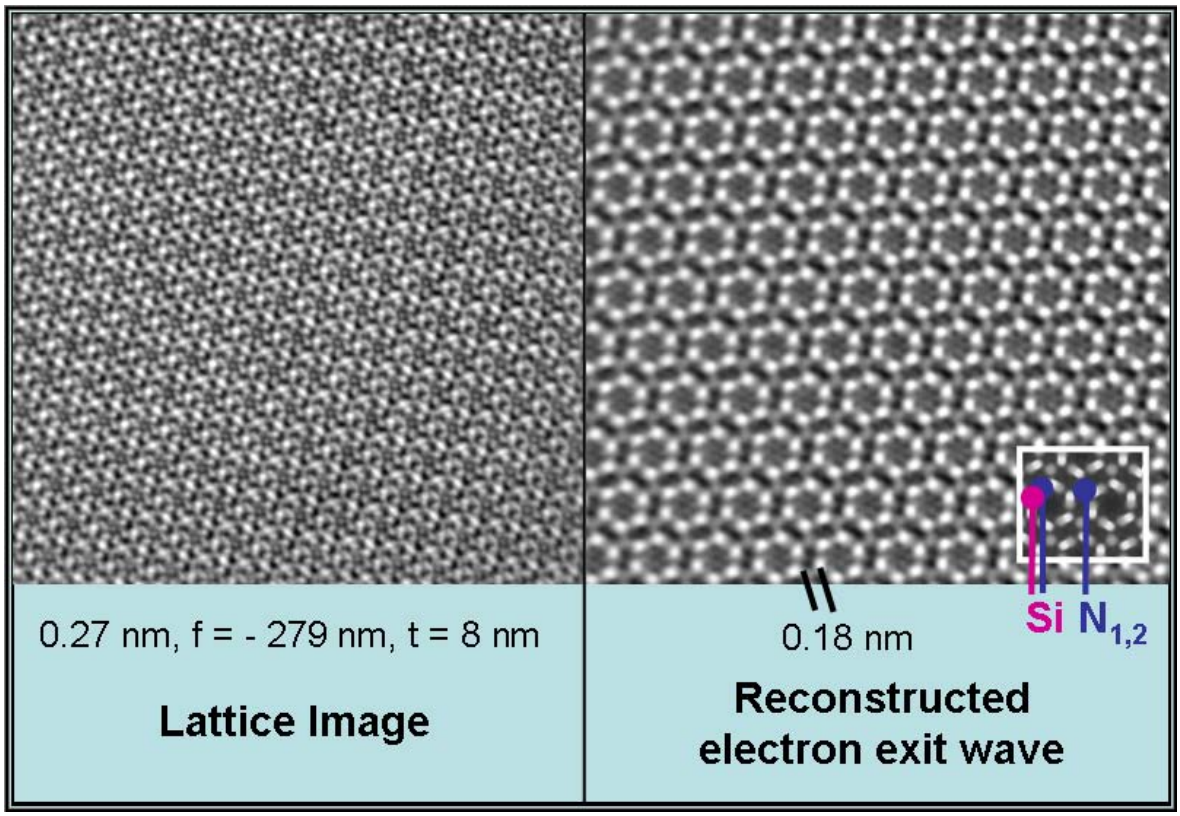


**Figure 2.10:** This graphic by [Kis06b] illustrates clearly the advantage of EWR: On the left side the normal lattice image for a silicon nitride ceramic sample of 7nm thickness is shown (defocus value of -279nm). Too many image Fourier components lead to this complicated lattice structure which does not represent the real structure. The result of the EWR is shown on the righthand side. Here detailed structure information is available, Si- and N-columns can be identified. The small white-framed square area shows a simulated image of the crystal structure.

- achieving for the information limit of the microscope
- removing delocalization effects
- correcting aberrations, astigmatism and coma
- receiving complete amplitude and phase information

Though this method was already developed more than 10 years ago it is still nowadays the best method relating to the determination of lattice structures in very small features.

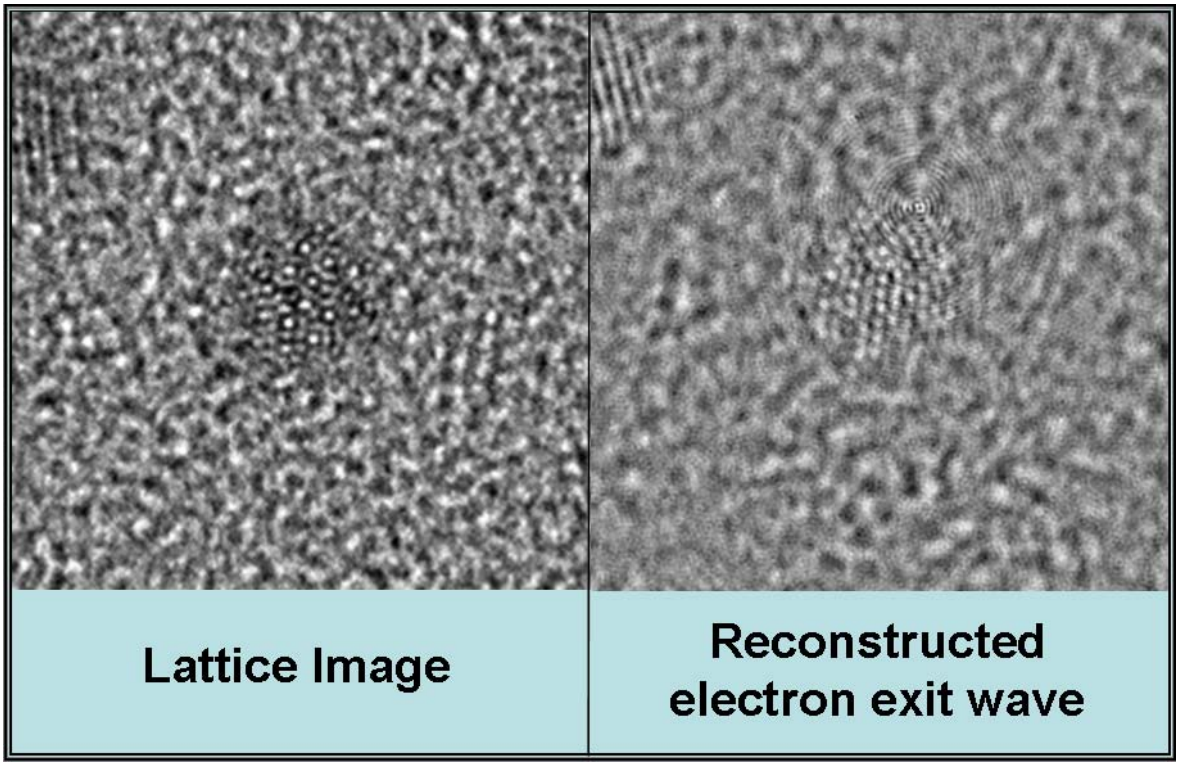


**Figure 2.11:** Another example demonstrating the efficiency of EWR for a FePt particle with 5-fold-symmetry. In the reconstructed phase image on the right hand side the atom columns are individually resolved on an amorphous C-coated grid whereas they are not in the left image taken under Scherzer defocus.

# Chapter 3

# Experimental Techniques

## 3.1 Preparation Methods of FePt-nanoparticles

In this section the two different preparation methods, gasphase condensation and organometallic synthesis, for the FePt-nanoparticles used in this thesis are described. Another section in this chapter deals with the development of a new TEM-Tomography holder and the preparation of special TEM/FIM-samples. Field Ion Microscopy (FIM) is a method providing chemical sensitive analysis. It was planned to perform experiments in the TEM to investigate the lattice structure and to analyze the same samples by FIM to reveal atomically resolved chemical information. The sample preparation for such TEM/FIM-investigations was never done before and could not be optimized during my thesis. The FIM investigations will have to be performed in the near future.

### 3.1.1 Gasphase Condensation

This method is established very well in our group and only the most important facts concerning my thesis are described. More information on the preparation of the FePt-nanoparticles by gasphase condensation can be found in [Sta03c, Rel03]. Recent investigations on the influence of nitrogen to increase the degree of chemical order [ea04] are discussed in [Dmi06c, Dmi06b]. The sputtering system was developed and built by S. Stappert [Sta03b]. This system allows for gasphase condensation of nanoparticles and thermal sintering of the particles in vacuum before deposition on a substrate. The system (fig. 3.1) consists of a nucleation chamber, a sintering furnace and a deposition chamber.

The FePt-nanoparticles are produced by inert gas condensation in the nucleation chamber: gasphase Fe- and Pt-atoms/ions are sputtered from a target and nucleate homoge-

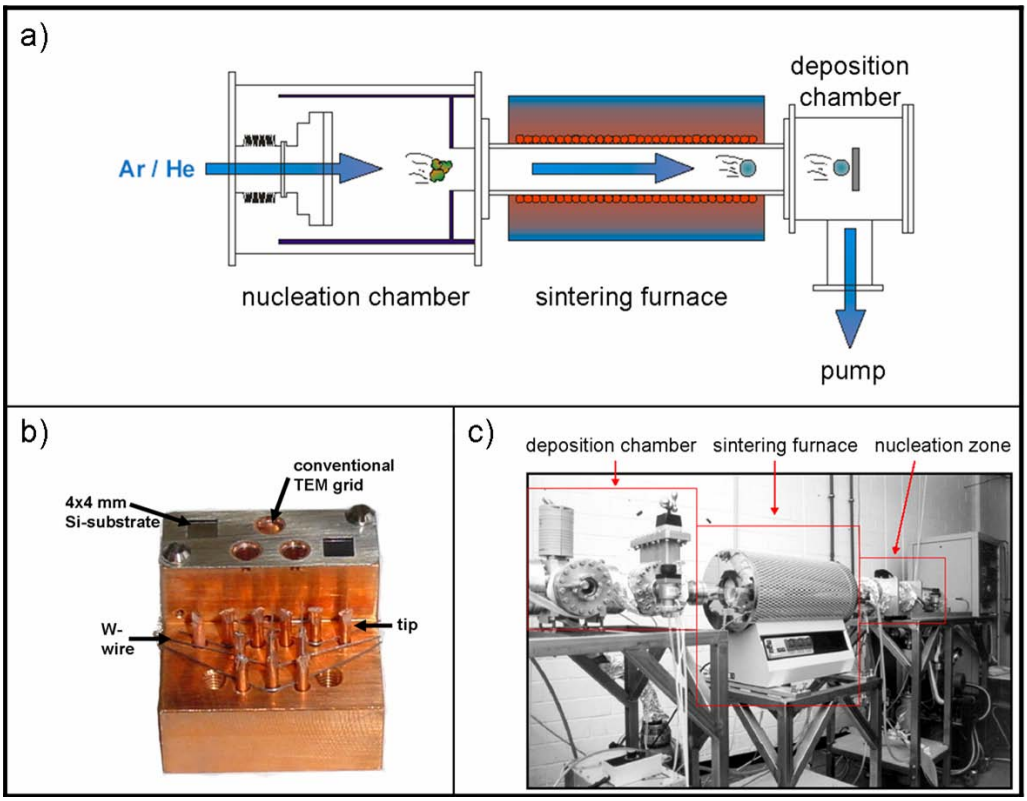


**Figure 3.1:** a) Simplified scheme of the sputtering system [Dmi03]. b) Sample holder developed in this thesis which allows a simultaneous deposition on tips, conventional TEM-grids and 4x4 mm Si-substrates. The W-wires are used to fix the tips in the holes which is necessary because of the vertical built-in position of the virtual moveable sample holder on which this holder is tightened in the deposition chamber. c) Picture of the sputtering system from [Sta03b].

nously due to the cooling in the nucleation zone which causes the supersaturation of metal vapor. The continuous gas stream carries the particles through the sintering furnace where temperatures up to $T_S = 1273\ K$ can be produced. Afterwards they are thermophoretically deposited onto the substrates. The chemical composition of the nanoparticles is approximately the one of the target but can vary with different target thickness [Sta03b]. The important parameters for the gasphase condensation method are:

$p$**:** the nucleation pressure.

$f_{Ar}$, $f_{He}$, ($f_{N_2}$)**:** the gas flow rates for Ar and He (and $N_2$) respectively.

$P_{DC}$**:** the power of the sputter source.

$t_{sputter}$**:** the sputtering time.

$T_{KS}$**:** the temperature of the cooling shield.

$T_P$**:** the temperature of the sample holder.

### Samples

The gasphase condensated particles investigated in my thesis were prepared by adding nitrogen in the sputtering process to get single crystalline, mostly $L1_0$-ordered particles [Dmi06c, Dmi06b]. The following parameters were used: p = 0.5 mbar , $f_{Ar}$ = 40 sccm, $f_{He}$= 50 sccm, $f_{N_2}$ = 10 sccm, $P_{DC}$= 250 W, $t_{sputter}$ = 25 min , $T_{KS} \approx$ -170°C and $T_P \approx$ -100°C. The $N_2$-flux rate corresponds to a ratio of 20% $N_2$ in Ar.

## 3.1.2 Organometallic Synthesis

Two different types of chemically prepared particles were analyzed. The synthesis was done by O. Margeat (see fig. 3.2).

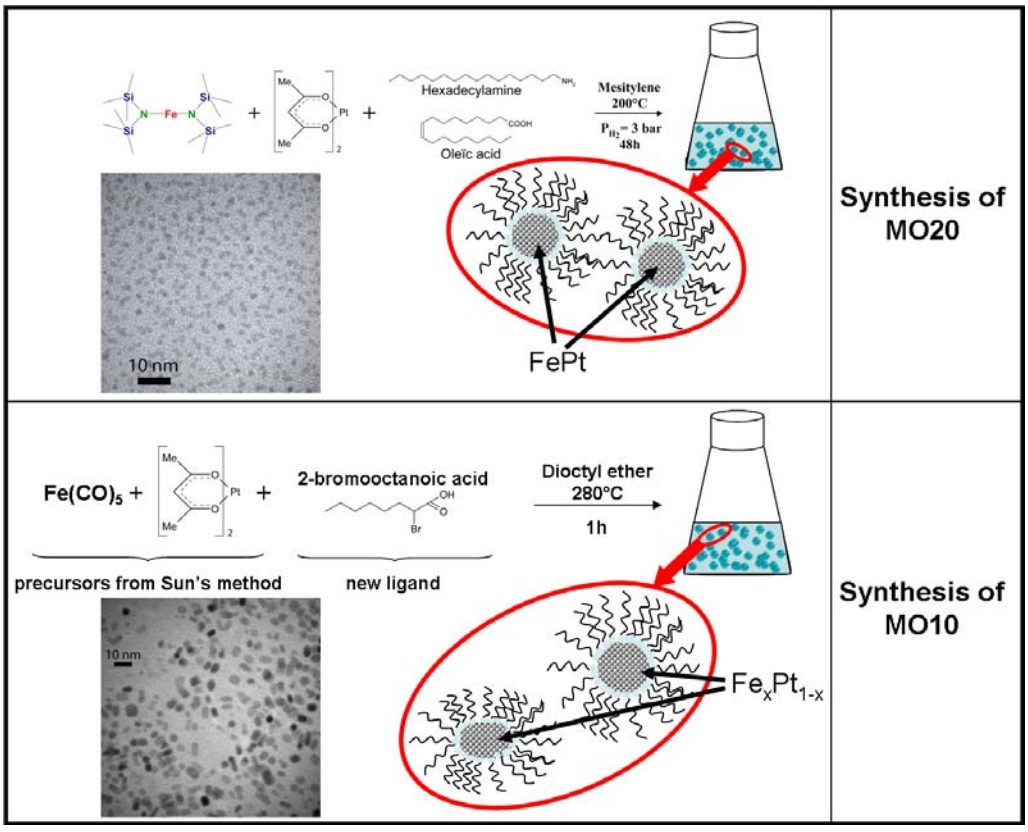


**Figure 3.2:** The two different wet chemical preparation methods: MO20 and MO10

The first sample **(MO20)** was prepared by the simultaneous reduction of the two precursors iron bis-bistrimethylsilylamide ($Fe[N(SiMe_3)_2]_2$) and platinum acetylacetonate ($Pt(acac)_2$). *Hexadecylamine* and *oleic acid* were used as ligands, and trimethylbenzene (*mesitylene*) as solvent. The mixture was then heated at 200°C during 48 hours under 3 bar of dihydrogen pressure (reducing agent).
The second sample **(MO10)** was prepared by a simultaneous decomposition and reduction of the two precursors iron pentacarbonyl ($Fe(CO)_5$)and platinum acetylacetonate ($Pt(acac)_2$) according to Sun's method [Sun00] and adding $2-bromooctanoic\ acid$ as a new ligand. The solvent was *dioctyl ether*. The solution was heated at 280°C during one hour and afterwards washed by adding ethanol and centrifugated.
Both samples used for the HRTEM investigations were common TEM copper grids covered with an amorphous carbon layer on which a drop of the solution was dried. After drying the grids were washed in aceton to remove dispensable ligands.

## 3.2 Microscopes

For my investigations I used two microscopes. The TecnaiF20 ST in Duisburg for the pre-characterization of the samples and the (OÅM), a modified Philips CM300FEG/UT, at the National Center for Electron Microscopy in Berkeley for the focal series acquisitions and the tomography studies. Both microscopes are shown in fig. 3.3. Technical details can be found in the Appendix section (A-1).

## 3.3 Software

Reconstructing the Exit Wave (electron wave function) of the sample was done with the TrueImage Professional software package by FEI. TrueImage consists of two independent parts, one part is used for the acquisition of a focal series in the microscope. The other one is for the reconstruction of the complete phase and amplitude information from a focal-series of HR-images. The TrueImage algorithm is patented and uses linear approaches as well as non-linear approaches. The advantage of this reconstruction consists in eliminating imaging errors like the spherical aberration of the microscope. Also the delocalization effects caused through the FEG (Field Emission Gun) source are removed so that the obtained images are directly interpretable beyond the point-resolution. The professional version of TrueImage, which was used for this thesis, also offers the features of manual correction of coma and 3-fold astigmatism and the automatic correction of 2-fold astigmatism and defocus [Fc06].

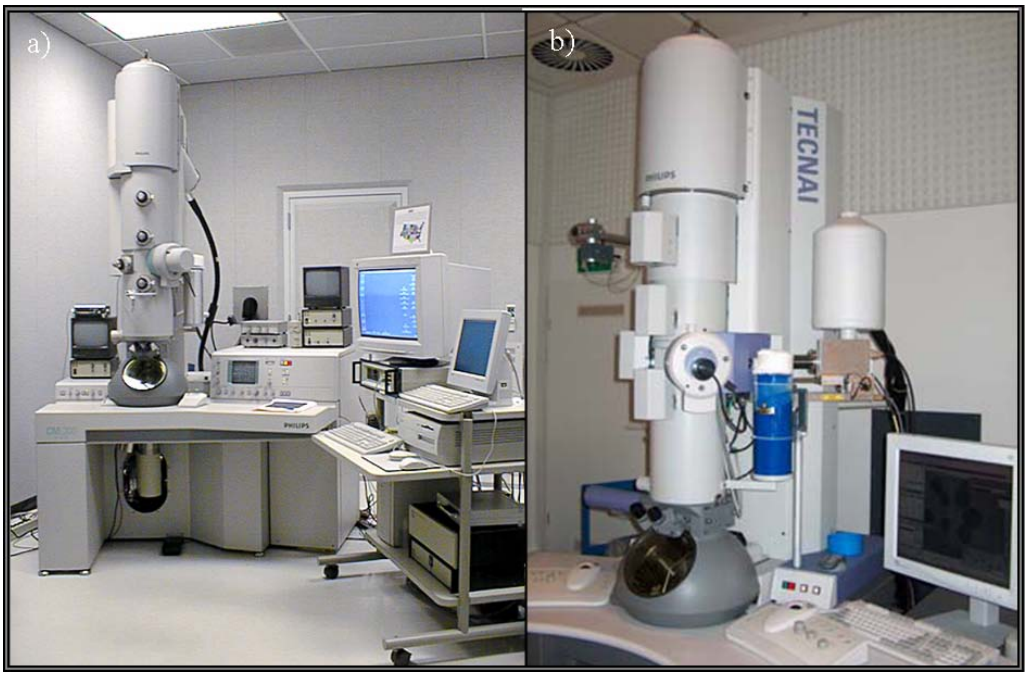


**Figure 3.3:** Microscopes: a) CM300 - (NCEM, Berkeley, CA) b)Tecnai - (University Duisburg-Essen, Duisburg)

A description of how the method of Exit Wave Reconstruction works was given in Chapter 2.2.2 and a short manual of how to use this software is given in Appendix A-5.

## 3.4 W-tip Preparation

As described before one aspect of this thesis was the preparation of samples which can be studied by HR-TEM for structural analysis and Field Ion Microscopy (FIM) for chemical analysis. For FIM sharp tips with a radius of curvature $< 100$ nm are needed. Therefore the idea was to prepare tips which can be studied in the TEM and afterwards being used as a FIM-sample. This idea also included the design of a special TEM-holder allowing the investigation of these tips. This holder is described in section 3.5. Typically used FIM-tips are etched Ag- or W-wires which are compressed in a Cu-tube of 1.5 mm outer and 0.5 mm inner diameter. The entire length of this sample is limited to 20 mm and not less than 17 mm. The length of the Cu-tube should be between 10 mm and 15 mm. For my investigations I chose Cu-tubes of 15 mm length and a W-wire because of the better expected adhesion character for the FePt-nanoparticles. To center the wire as good as possible in the Cu-tube both were centered in a lathe. The centering becomes important

for tomography, since if it was not centered, a step-wise rotation around its axes would bring the tip out of the focus. With a special flat-nose pliers the Cu-tube was compressed so that the W-wire was fixed. Although the lathe was used for centering, this did not guarantee having the wire centered afterwards but gave the best results comparing to other tried methods. After centering and fixing the W-wire it was cut to a length of approximately 5 mm (up from the Cu-tube).
For the electro-chemical etching of the tips a special construction developed by D. Severin in his diploma thesis was used [Sev03]. With this it was possible to dip the wire in a controlled way into the electrolyte. 2 M NaOH was used as electrolyte. FIM-experts (T. Al-Kassab, E. Marquis) told me to try alternate current, a voltage between 1 and 5 Volts and a successive retracting out of the electrolyte to get sharp tips. To find the optimum parameters more systematic experiments have to be done. After the etching process the tips had to be washed several times in distilled water to remove the rest of the electrolyte. After this, the tips were also dipped in methanol to remove all the water out of the Cu-tube. Methanol evaporates quickly and takes the water with it.

**Deposition of gasphase FePt-nanoparticles on the tips**

After etching the tips the final sample had to be prepared. To be able to position the tips on the sample holder of the sputtering system a new tip holder had to be made. The one designed by me allows the simultaneous deposition of nanoparticles on tips, TEM-grids and Si-Substrates. A picture of this holder with built in tips is shown in fig. 3.1 b). There are three lines of holes with 4 and 3 holes each, respectively. The tips are put into the holes and fixed with a bent W-wire in each line as can be seen in the picture. The Si-substrates and the TEM-grids are fixed with an Al-sheeting which is screwed to the holder which is made from Cu. On the other side of this holder (not visible in the picture) there is a screw which allows to apply a voltage to the holder. First experiments showed that there are already some particles deposited on the tips without applying any voltage. To deposit the nanoparticles on the tips the sputtering procedure is the same as for any other sample. There is no way of avoiding C-contamination on tungsten, but in order to reduce it as good as possible the tips were brought to degas into the evacuated system 1-2 days before the sputtering process.

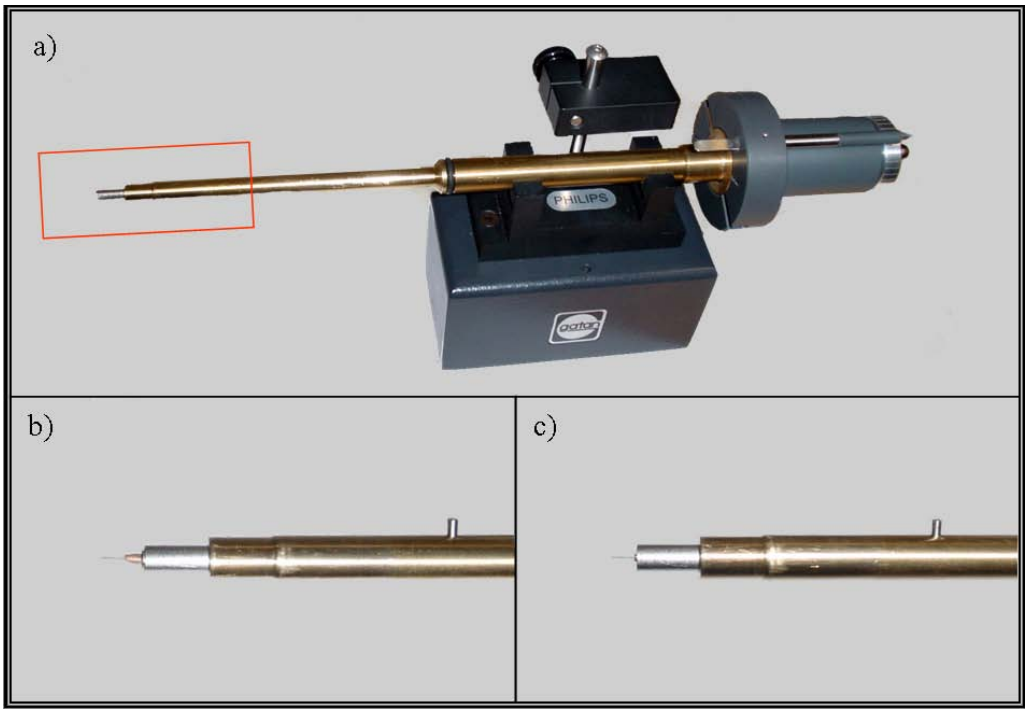


**Figure 3.4:** New TEM-holder: a)full view b)tip extended - built-in situation c) tip retracted - position as in TEM

## 3.5 TEM-Holder for Tomography

The FIM-tips should be analysed in the TEM first before being used as a FIM-Sample. Since the FIM-tips do not fit into a standard TEM-holder, a new one had to be constructed. The idea was to be able to fully rotate around its axis and to mechanically protect the tip during the transfer into the evacuated TEM-column. A ball bearing offers the opportunity to insert a guiding rod on the top on which the tips can be fixed by simply pulling it with tweezers into the suited vent. By rotating the gray sleeve at the end of the holder the bar moves forwards and backwards and the tip can be retracted till it is fully screened by the protection sleeve (see a) in figure 3.4). With this construction translation and rotation are completely independent.

# Chapter 4

# Results and Discussion

In this chapter three different methods for the determination of the lattice parameter of FePt nanoparticles with sub-angstrom resolution are compared and the results are discussed.
It is shown that all lead to the same result within the error bar. First Fourier and bright field analysis for the lattice constant determination are shortly described and the error estimation for both methods is described in section 4.1. The Quantitative HR-TEM ("Z-contrast") as possibility for columnwise chemical analysis is discussed in section 4.2. In section 4.3 all results for the gasphase particles and in section 4.4 for the colloidal particles are presented.
Another question, if small changes of the lattice constant, e.g. due to the $L1_0$-phase, can be detected, is addressed in section 4.3.1. The difference between the lattice constant in a- and the c-direction is 3.8% (table in section 6.2)[Lan92].

## 4.1 Software Analysis of TEM images

### FFT analysis of bright field images

The lattice constant a and the lattice plane spacing $d_{hkl}$ of fcc structures are related acc. to eq. 4.1. For the tetragonal distorted $L1_0$-structure this equation is more complicated and given in Appendix: eq. 6.2.

$$\mathbf{a} = d_{hkl} \cdot \sqrt{h^2 + k^2 + l^2} \tag{4.1}$$

The miller indices (h,k,l) can be determined by the Fast Fourier Transform (FFT) of the bright field image or better the reconstructed phase image of the particle (4.1).

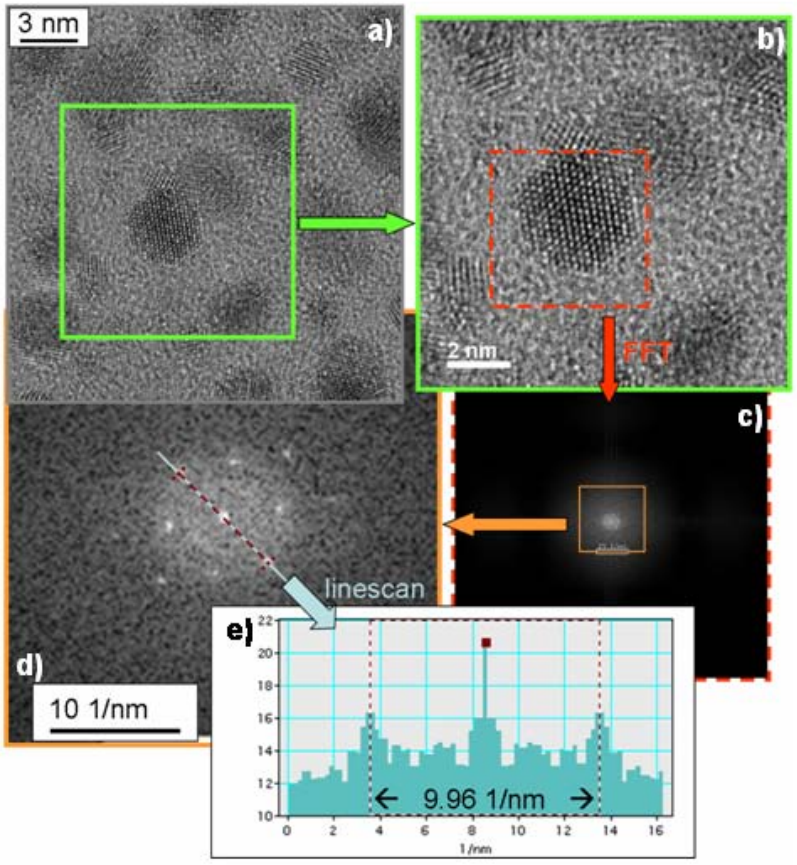


**Figure 4.1:** : Scheme of the FFT analysis steps as described in the text.

The FFT pattern corresponds to the diffraction pattern which can be recorded in another TEM mode. The distance between one diffraction spot (h,k,l) and the center spot (0,0) is the reciprocal $d_{hkl}$-spacing. The distance between the two diagonal equivalent diffraction spots was measured and then the reciprocal of half the distance was determined to get the $d_{hkl}$-values. In fig. 4.1 the whole procedure is demonstrated : First a squared frame as large as possible (overlap with neighboring particles has to be avoided) for the FFT has to be marked (b). The larger this frame can be chosen the finer is the resolved FFT image(c). This FFT image was magnified so that the diffraction pattern was better visible (not changing the total number of pixels)(d). The distance between two diffraction spots is determined from an intensity profile (e). $d_{hkl}$ and the lattice constant **a** are calculated according to eq. 4.1.

**"Bright field" analysis**

The layer resolved structure can be determined from intensity profiles (linescans) across atomic columns, observed in bright field TEM images (fig. 4.2). The images were scaled by 400% for easier analysis.
Assuming that the spacings are equal, the average d-spacing is calculated by dividing the distance between the intensity maximum of the first and the last measured atomic column by the number of atomic columns minus one. For non periodic structures the distance between two adjacent columns is measured.
For the latter method the error is much larger than for the averaging method, since it is directly given by the resolution, which I have limited to one pixel, and small changes in the "pixel" separation are not averaged out. For perfect periodic structures it is evident that the larger the distance the smaller the error.
In this work mostly both analysis methods were performed. The FFT of a linescan (referred to as FFT ls in table 4.3) was taken in to see if there is more than one peak, i.e. more than one periodicity in the lattice spacing. This method, however, leads to no improvement as the analysis for the series23 and for the series62 particle has shown. The uncertainty for the FFT graphs was almost 5% and consequently too large for the needed accuracy (for an example, see Appendix: A-4). Therefore it was not used for detailed relaxation investigations.

Linescan parameters are the length and the width of the line in pixels (integration width). If it is set larger than 1 the resolved linescan is an averaged intensity profile over this width. It is always useful to slightly increase the integration width to make sure that all maxima are included. If it is only set to one pixel also artifacts and noise contribute strongly to the intensity profile. By increasing the integration width these effects are weakened and the intensity profile is smoothed. Large integration widths, as used for "fast" analysis can also result in artifacts as discussed in section 4.3.2.
Fig. 4.2 illustrates the effect of changing the width of a linescan. The two viewgraphs show the same linescan as indicated in the image above for different integration widths from 1-20 pixels. The framed area of the left viewgraph is magnified in the right one. Also the mathematical average of those linescans was formed and it turned out that the 10 pixel integration width was in good accordance to this average and consequentially was used for further investigations of single layer linescans.

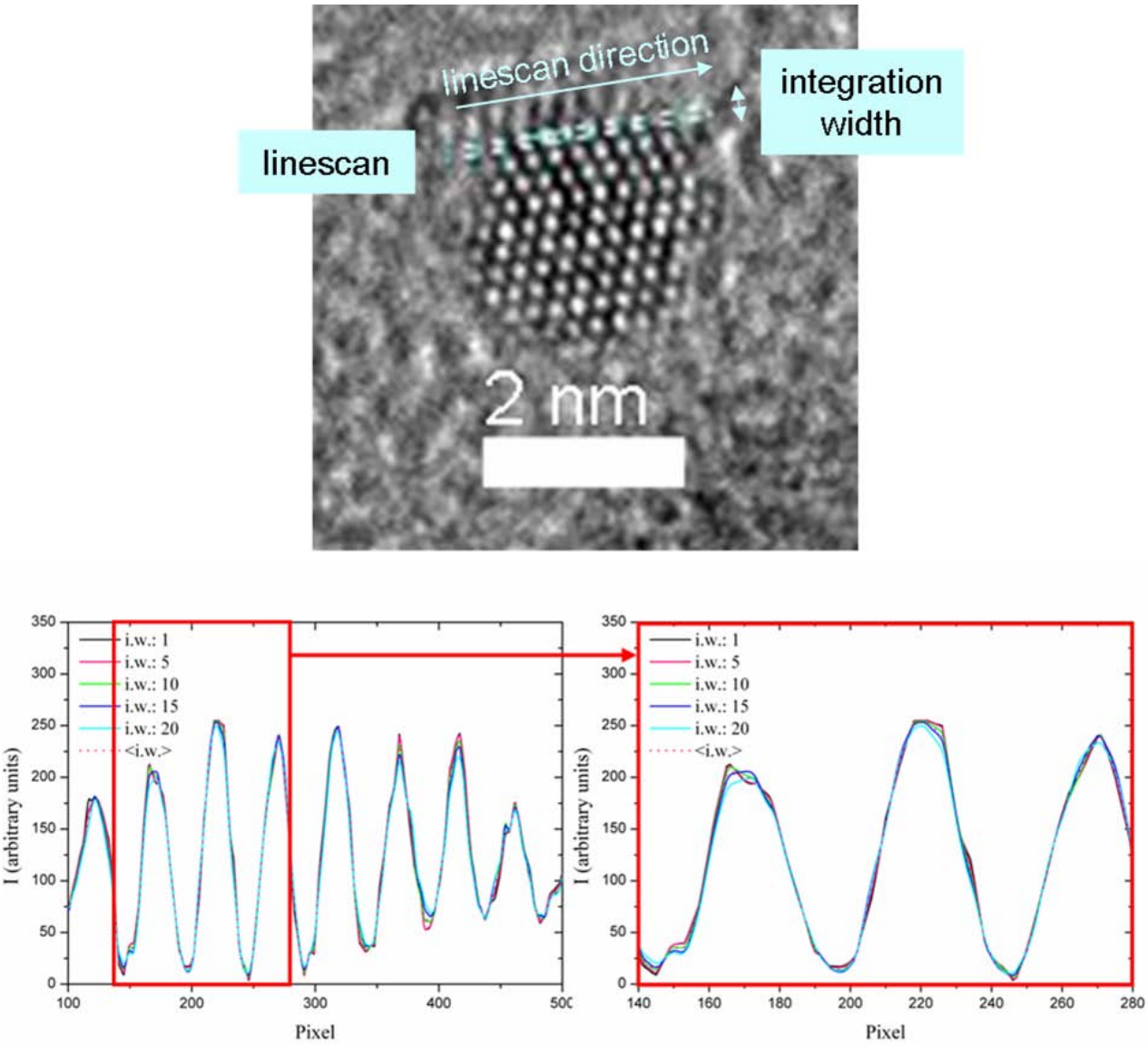


**Figure 4.2:** . This graph shows several intensity linescans for different integration width (i.w.) values. <i.w.> is the average over all linescans.

### Evaluation of error bars

For the analysis methods presented in the two previous sections the accuracy and the resolution is limited by the quality of the micrograph and the software. The analysis in this thesis was done with the DigitalMicrograph(TM) 3.6.5 for GMS 1.1 software by Chris Meyer, Doug Hauge and the Gatan Software Team. The resolution cannot be more accurate than one pixel in the micrograph. Fig. 4.3 shows a linescan for the "series 62"

colloidal particle[1].
The measured peak separation (in [200]-direction) is 9.96 $nm^{-1}$ in a). The circles mark the areas in which the peak intensity is the same - that means an uncertainty in the positioning of the distance determination tool. In b) the smallest resolvable interval is shown, which is 0.2 $nm^{-1}$ here. Hence, the start or end position of the linescan can only be varied by this amount in one direction.
With eq. 4.2 the upper and the lower error limits of the distance x/2 can be determined. We calculate $1/d_{200} = x/2 = 4.98\ nm^{-1}$ for the reciprocal $d_{200}$-spacing and 0.2008 nm for the absolute $d_{200}$-spacing ($d_{200} = \mathbf{a}/\sqrt{4}$).

$$d_{hkl} = \frac{1}{\frac{x}{2} \pm \Delta} \tag{4.2}$$

The error bar to the upper boundary is bigger than for the lower boundary, approximately 0.4%. Here it is 0.1931 nm < 0.2008 nm < 0.2092 nm (-3.8%, +4.2%). The error bar depends on the size of the frame for the FFT but can be pushed below 2%. In the example a small frame was chosen.
As already mentioned before, the error for the bright field intensity linescans is also the pixel-uncertainty, for my investigations of the phase images typically 0.00505 nm. This value is due to the scaling of 0.0202 nm/pixel of the phase images reconstructed from the CM300 focal series and the rescaling by 400%. Even though this interrelationship between the scaling and the error suggests that the larger the scaling the smaller the error it is clear that larger scaling is physically useless. By increasing the number of pixels the information content is not increased since it is limited to the number of pixels of the reconstructed images. Magnifying the image only makes the positioning of the linescans easier. Apart from that, the scaling of the bright field image does not effect the FFT image at all. A magnification of 400% allowed an easier positioning of the cursor on the computer screen.

The previous error consideration for the FFT analysis is valid for every single diffraction spot measurement, whereas the error bars in the following figures are given - if no other specification is given - by the standard deviation of the average of distances determined in different directions.

### Other possibilities of investigating relaxations

For the layerwise investigation of the lattice parameter I used the "linescan method" but there exists another possibility: NCEM developed a software called "Derip" for the deter-

[1]The Scherzer image was used for this case.

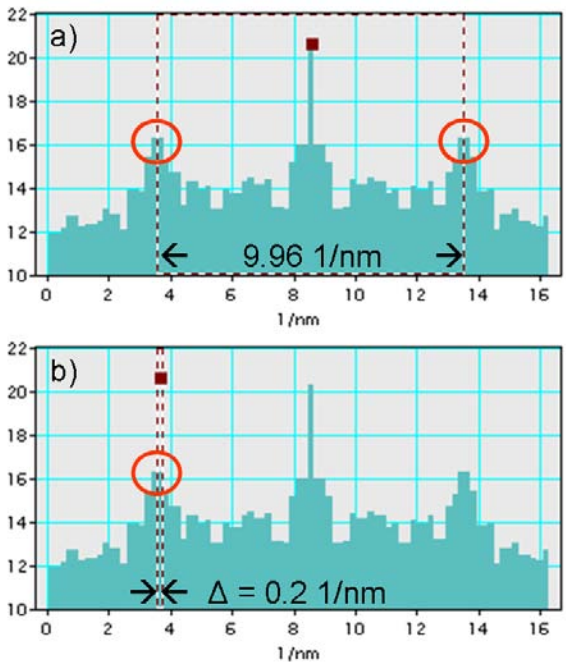


**Figure 4.3:** Limit of the FFT-analysis. a) Shows the linescan also shown in fig. 4.1. The red circles indicate the peaks used for the distance estimation. b) Shows the minimum resolvable interval $\Delta$ by software which corresponds to one pixel in the micrograph.

mination of the intensity maxima in a picture. The maxima are evaluated by a software algorithm that marks these positions with a so-called "blob". A schematic view and a short description of a detection process with "Derip" is given in fig. 4.4. These "blobs" can be recorded and exported as a .dat-file into an analysis-program like $ORIGIN^{TM}$. "Derip" is said to work with an accuracy of 0.1 pixel. When the .dat-file is imported into ORIGIN all y-values have to be multiplied by minus 1 to represent directly the positions of the recorded blobs. In order to plot the blobs in the aspect ratio as taken from the image the ratio of x/y-axis has to be adjusted, in the case of that particle shown in the scheme it is 1.36 (750/550). A special tool for ORIGIN7.5 enables the measuring of the distance between two points. This distance determination tool can be used by eye only. Its accuracy is so rough that a direct investigation of the lattice relaxation was not done with the Derip images.

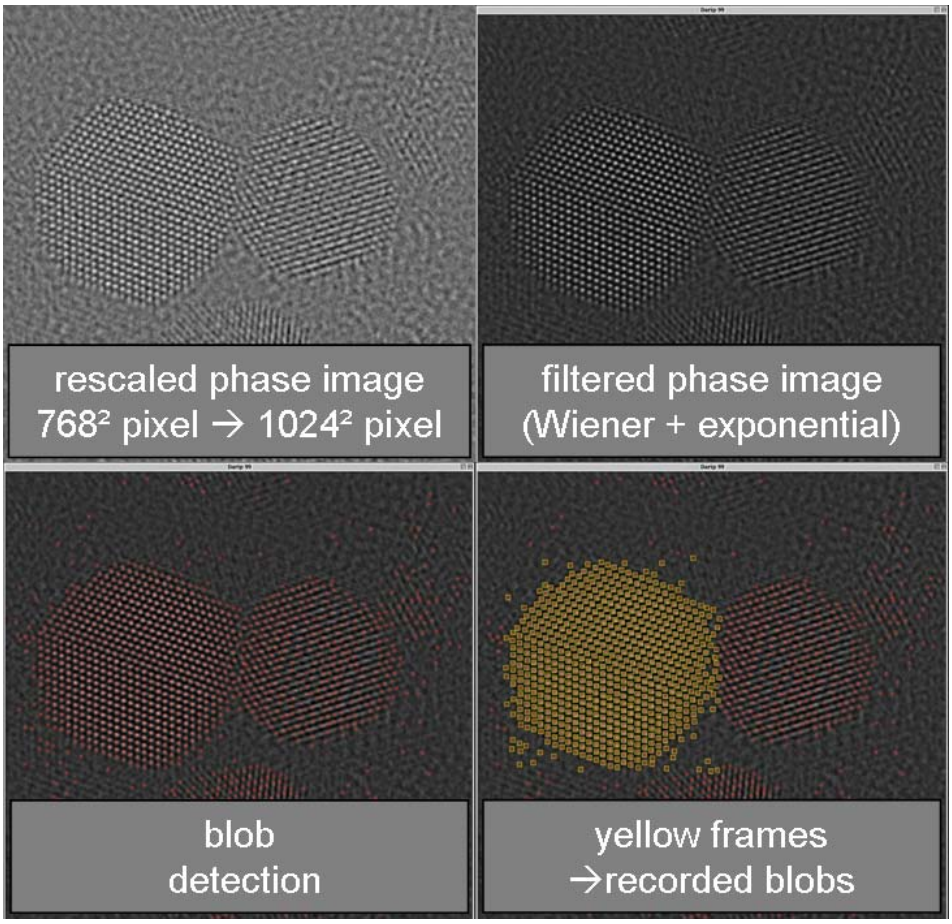


**Figure 4.4:** Working procedure for Derip: First the image has to be scaled to $1024 \times 1024$ pixel$^2$. Secondly the image is filtered exponentially and also with a Wiener filter to increase contrast and decrease the noise signal from the amorphous part of the sample. Then the blobs detection parameters are optimized till all or as many atom columns (intensity maxima) as possible are detected. Fourth a frame can be set to choose the area of blobs which are to be recorded. The blobs in this area are automatically put into a .dat-file yielding the corresponding coordinates.

### Discussion of results

The discussions following in the next sections will include the analysis of average values by less than 1%. In terms of the absolute error bar these discussions have to be regarded very critically. Nevertheless they were performed to emphasize small changes between different analysis methods and possibly see some tendencies in the variation of the lattice parameter. The maximum precision obtainable from the EWR at the OAM is 2 pm [Xu05], i.e. approximately 0.5% with respect to the bulk but up to 1.5% ($d_{222}$) for the smaller d-spacing values for $Fe_xPt_{1-x}$.

## 4.2 Quantitative HR-TEM

In this section I discuss a simplified model for quantitative HR-TEM analysis as a possible tool to identify the elemental composition in atomic columns. As described in section 2.2.1 this contrast provides chemical sensitivity for single atomic columns. The exit wave reconstructed phase images represent the real lattice structure, i.e. the positions of atomic columns. The intensity in those images corresponds to the phase of the electron wave after scattering of the potentials in the atomic column.
The task is to identify the chemical composition of the single columns from intensity (phase) profiles across atomic columns. The following simple analysis is approximately valid for a total phase shift smaller than $2\pi$ (see chapter 2.2.1, extinction distance). This limits the analysis to real samples with a thickness of less than 5 nm for large Z-elements like Pt (Z = 78) or Au (Z = 79) or less than 40 nm for light elements like C (Z = 6)(fig. 2.5).
To illustrate the possible information which could be obtained one chemically disordered (fig.4.5) and one $L1_0$-ordered (fig. 4.6) 10-shell cuboctahedron were modeled. Both are viewed from the [011]-direction. The electron beam is assumed to come from top and scatters along the atomic columns. Pt-atoms are light blue and Fe-atoms dark grey. The $L1_0$-cuboctahedron has top and bottom Pt-surface layers. In figure 4.7 the simple Z-dependence of the signal which is proportional to $Z^{1.7}$ for STEM and to $Z^{2/3}$ for HR-TEM are plotted for columns 1-17 of the model. The column signal was calculated according to equation 4.3 and is also given in table 4.1.

$$Intensity = x * 26^y + (n - x) * 78^y \tag{4.3}$$

n is the total number of atoms in the column, x is the number of Fe-atoms in the column and y is 1.7 for the STEM and 0.67 for the TEM calculation. 26 is the atomic number Z for iron and 78 is Z for platinum. Figure 4.7 is an estimate of the expectable signal if dynamic scattering would be removed. Only the Z-dependence was calculated and any other influences or offsets neglected. The number of Fe-atoms in each column is marked with a green striped bar.

The even-numbered columns in the $L1_0$-phase consist of Fe-atoms, the odd ones of Pt-atoms only. For the chemically disordered particle the distribution is 50:50 for even-numbered columns whereas for odd-numbered columns there is one more Fe-atom than Pt-atoms. There are three exceptions: column 1 which consists of one single Pt-atom as for the $L1_0$-phase and column number 11 and 15 which have one more Pt-atom than Fe-atoms which results in a signal increase by 14% for the STEM and 6.5% for the HR-TEM. Such a small difference when replacing Fe and Pt can only be detected by STEM if

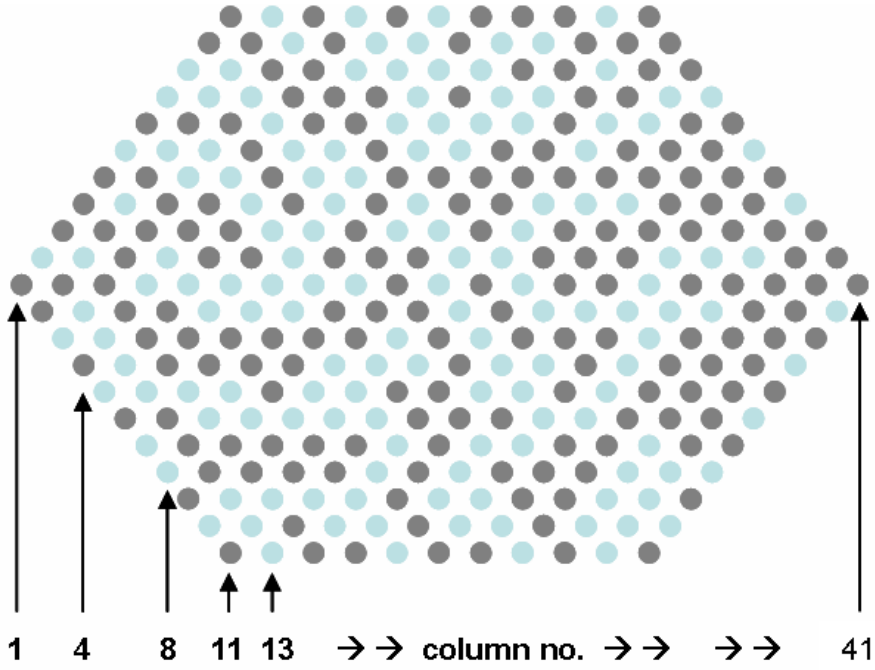


**Figure 4.5:** Model of a 10-shell chemical disordered FePt-cuboctahedron along the [011]-direction. The gray dots mark Pt-columns, the light blue dots Fe-columns.

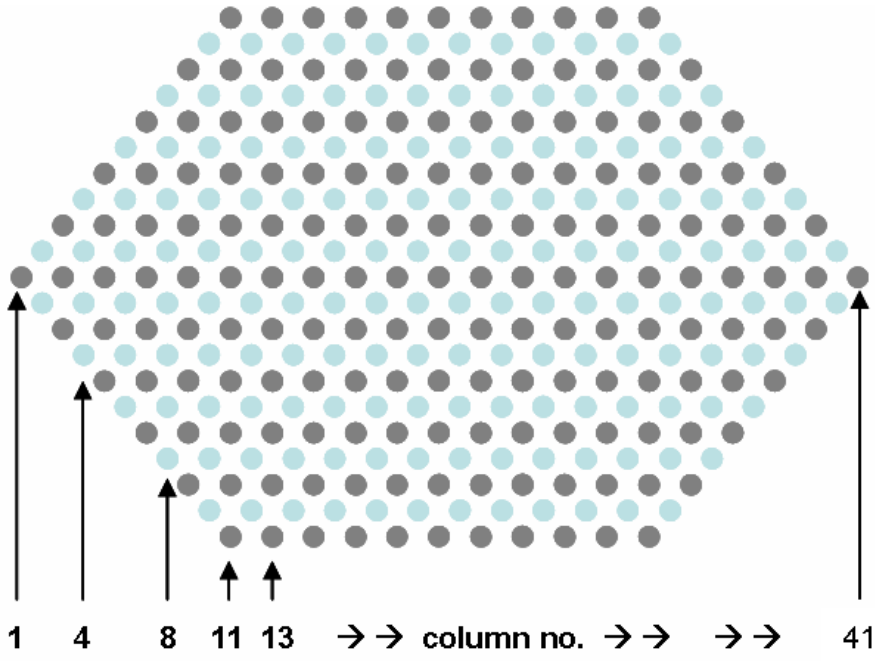


**Figure 4.6:** Same view of a cuboctahedron as in fig. 4.5 but for the $L1_0 - phase$ (fct).

| 1 | 2 | 3 | 4 | 5 | 6 | 7 | 8 |
|---|---|---|---|---|---|---|---|
| 1 | 0 | 0 | 1 | 1646.49655 | 1646.49655 | 18.25561 | 18.25561 |
| 2 | 1 | 2 | 2 | 508.72688 | 1900.85999 | 17.55277 | 27.032 |
| 3 | 1 | 0 | 3 | 4939.48964 | 3547.35654 | 54.76684 | 45.28761 |
| 4 | 2 | 4 | 4 | 1017.45376 | 3801.71998 | 35.10553 | 54.06399 |
| 5 | 2 | 0 | 5 | 8232.48274 | 5448.21653 | 91.27806 | 72.3196 |
| 6 | 3 | 6 | 6 | 1526.18065 | 5702.57997 | 52.6583 | 81.09599 |
| 7 | 4 | 0 | 7 | 11525.47584 | 5956.94341 | 127.78929 | 89.87237 |
| 8 | 4 | 8 | 8 | 2034.90753 | 7603.43996 | 70.21106 | 108.12798 |
| 9 | 5 | 0 | 9 | 14818.46893 | 7857.8034 | 164.30051 | 116.90436 |
| 10 | 5 | 10 | 10 | 2543.63441 | 9504.29995 | 87.76383 | 135.15998 |
| 11 | 5 | 0 | 11 | 18111.46203 | 11150.79649 | 200.81173 | 153.41559 |
| 12 | 5 | 10 | 10 | 2543.63441 | 9504.29995 | 87.76383 | 135.15998 |
| 13 | 6 | 0 | 11 | 18111.46203 | 9758.66339 | 200.81173 | 143.93636 |
| 14 | 5 | 10 | 10 | 2543.63441 | 9504.29995 | 87.76383 | 135.15998 |
| 15 | 5 | 0 | 11 | 18111.46203 | 11150.79649 | 200.81173 | 153.41559 |
| 16 | 5 | 10 | 10 | 2543.63441 | 9504.29995 | 87.76383 | 135.15998 |

**Table 4.1:** Theoretical Z-contrast of the cuboctahedra shown in fig. 4.5 and in fig. 4.6. In this table column 1 is the index, column 2 the number of Fe atoms in the respective columns for the chemical disordered model, column 3 the number of Fe atoms for the $L1_0$-ordered case, column 4 the total number of atoms in the column, columns 5 and 6 the STEM signal for the chemical disordered and the $L1_0$-ordered case and columns 7 and 8 the HR-TEM signal for the chemical disordered and the $L1_0$-ordered case, respectively.

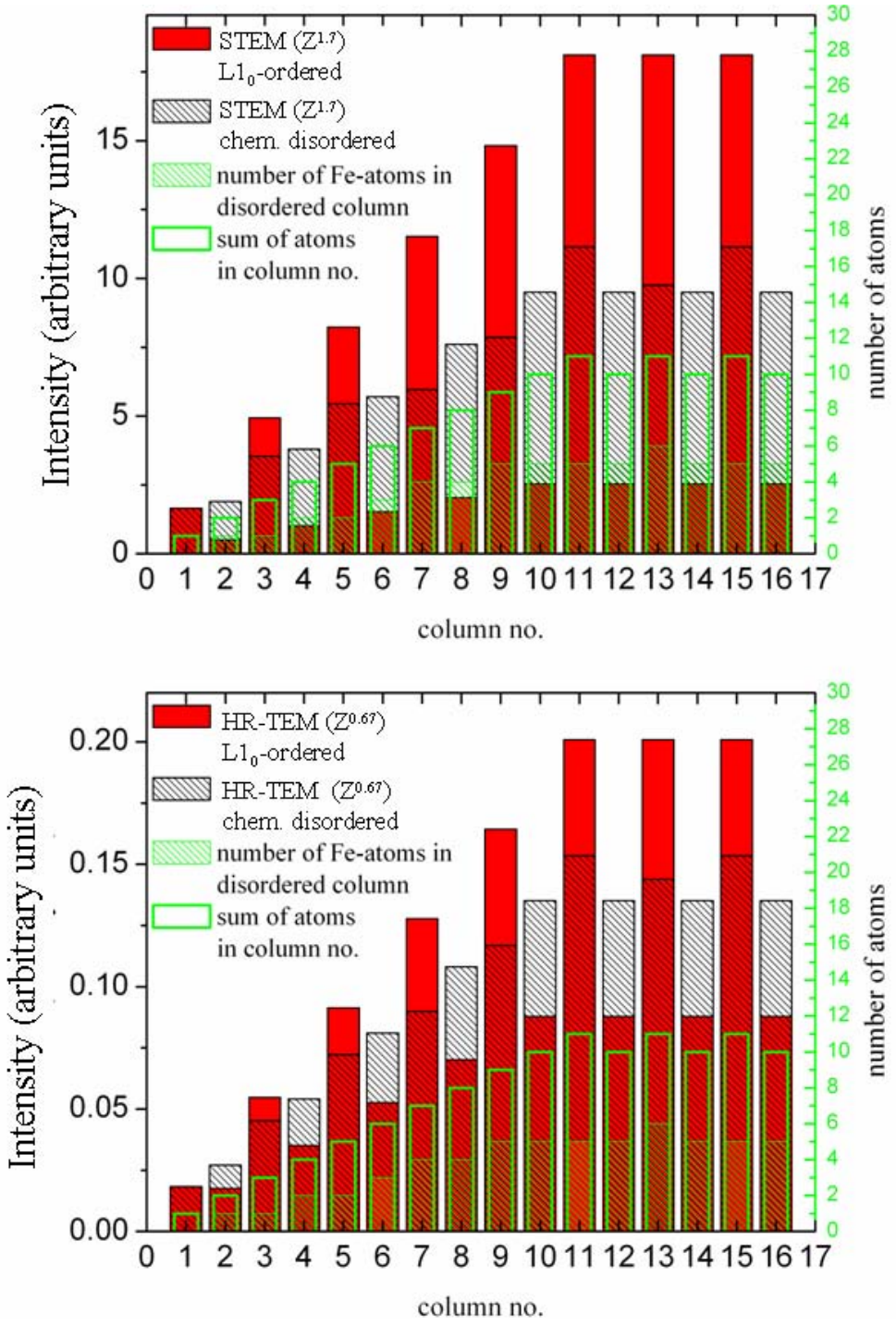


**Figure 4.7:** Calculated Z-contrast for the two cuboctahedra shown in figures 4.6 and 4.5. The intensity values are divided by the factor 1000 with respect to those given in table 4.1. The upper graph shows the intensity STEM Z-dependence and the graph below the intensity for the HR-TEM Z-dependence. Note the different intensity scales! The green lined bar in each viewgraph gives the number of atoms in the corresponding column. The green striped column gives the number of Fe-atoms in the chemically disordered column accordingly. For the $L1_0$-phase the even column numbers consist only of Pt-atoms and the odd ones only of Fe-atoms, see fig. 4.6.

the signal/noise-ratio improves (2.4). The HR-TEM simulation of the Z-contrast will be discussed in more detail. Comparing columns 1 and 2 it is evident that the signal is the same for one Pt-atom per column or for two Fe-atoms per column (fig. 4.7 bottom, red bars). That means, it is impossible to distinguish in-between the two cases. By further considerations it also becomes obvious that there is no constant ratio which would indicate for one more Pt- or Fe-atom in a column. It depends on the number of atoms per column very sensitively. One should note that also columns which are not next to each other may give similar signals depending on the Pt/Fe composition in the column. Column 7 for the $L1_0$-phase and column 10 for the disordered phase give an almost identical signal, although the number of atoms differs by three.
Hence the determination of column compositions from a single image of a particle is impossible in the center of a particle. A flat intensity profile could have two reasons:

1. the number of atoms per column and the composition of all columns is the same. In my simplified model it would make no difference where the Pt and Fe are positioned in the column. In a refined more realistic model the actual positions of the different elements will influence the overall column Z-contrast.
   or

2. the chemical composition changes from the inner to the outer columns - more atoms of larger Z are in the outer columns which usually consist of less atoms.

That means, to be able to make any statement about the chemical compositions of the atom columns the shape of the particle has to be known since a normal TEM image is only a 2-dimensional projection. Shape information can be obtained from tomography investigations [Bal06], that is from high resolution images taken along different crystallographic axes of the nanoparticle.

Image acquisition of the same particle in different orientations can take a long time and beam damage to the sample is likely. First tomography experiments on FePt-cubes at the NCEM in Berkeley also showed that there is significant change in the form of the particles for only a few tilt-steps [Sud06]. Therefore it is necessary to control beam damage. This can be achieved by the application of low-dosed techniques or by the choice of appropriate voltages. The challenge for the future is to acquire such tomography series, that is along many directions focal series have to be recorded without damaging the particles. Even if this can be achieved, the challenge remains to identify the number of atoms per column viewed from different directions. Due to the "phase wrapping" of the exit wave the particles must be small enough in all these directions. The model of the nanoparticle

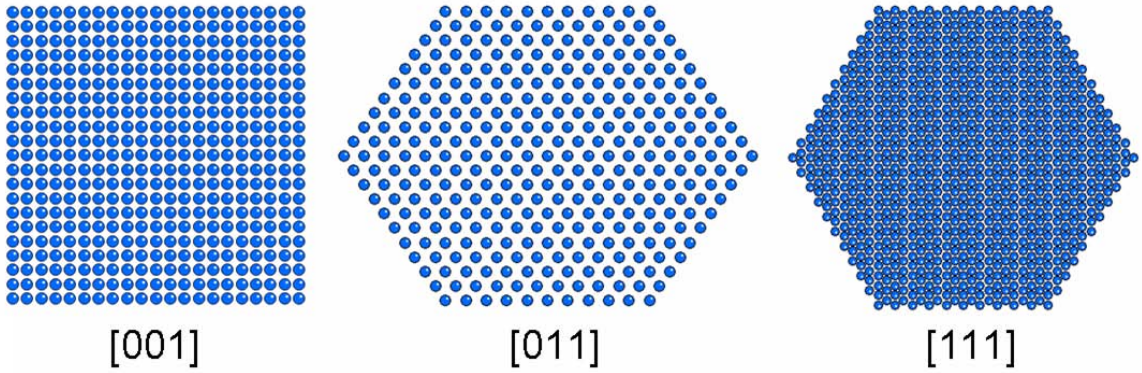


**Figure 4.8:** . Scheme of a 10-shell perfect cuboctahedron along the [001]-, [011]- and the [111]-direction.

according to the tomography results would undergo a simulation process with a HR-TEM simulation software for the zone-axis the focal series were taken from. The phase images reconstructed from those series have to be compared to the corresponding simulated phase images. In the framework of this thesis it was not possible to recover the structure and its chemical constituents yet. In order to understand and interpret the recorded images I compared image simulations with the experimental data. However, this is possible only within limitations because the image contrast in experimental images is commonly smaller than in the simulations (Stobbs factor) and phase-wrapping has to be considered [Kis06b].

### First simulation results

To simulate the TEM phase contrast from real space models of different crystals with different compositions the MacTempasX software by R. Kilaas [Kilb] was available at NCEM, LBL. This program was not optimized for small particle simulation. The x,y,z coordinates for a cuboctahedron had to be defined in a data file which could be read by the software.

For simplification I start the discussion for a pure Fe-cuboctahedron. The beam is in the [001]-direction so the [001]-layer of the particle is seen. Due to the geometry of the cuboctahedron this layer appears as a square. The resulting phase image is shown in fig. 4.10 on the left. In the right image the central Fe-atom was replaced by a Pt-atom. The gray scale phase images show no significant difference at the center column. The plotted intensity profiles, however, for the linescans show a phase shift of approximately 0.3 rad, which is equal to 12%. That means the Pt-atom gives a 12% larger signal than the

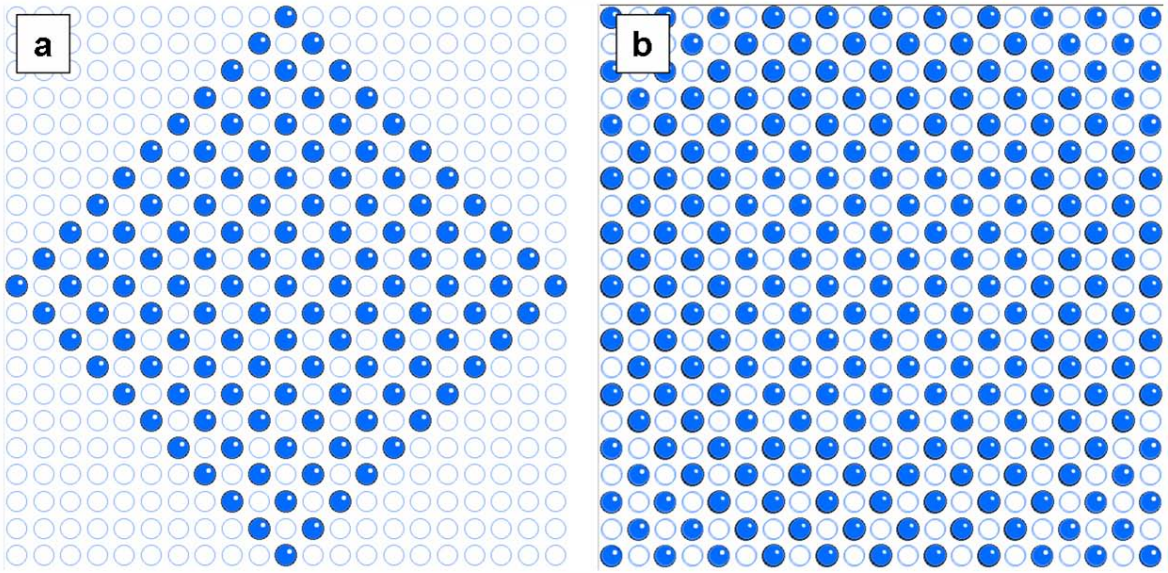


**Figure 4.9:** . Cross section views of the cuboctahedron used for the simulations. a) surface layer - used for linescan edge b) center layer - used for linescan middle

Fe-atom. The difference between the other columns for which the number of Fe-atoms is alternating between 10 and 11 (see also fig.4.9b)) is only 0.05 rad (2%). The same linescans were also done for the amplitude images (modulus) of the exit wave (fig.4.11). In this figure the difference is much smaller, 4% only if the central Fe atom is replaced by Pt. In the amplitude (modulus) signal, on the other hand, the different number of Fe atoms in the columns can be resolved easily. As expected the signal for the outermost columns is larger than for columns consisting of the same number of Fe-atoms in the inner part of the particle because of the dynamical scattering. For the columns consisting of 11 Fe-atoms also next to the center column with the Pt-impurity the modulus is even smaller.
In analogy to this observation, there are also differences in the phase image for the outermost columns. Here the phase is smaller than for any other 11 Fe-atom column and even smaller than for a 10 Fe-atom column. It makes clear that the phase signal of the reconstructed image is not easy to understand and that simulations for many specific models are mandatory.

A linescan (fig. 4.12) along a surface layer of the cuboctahedron was also looked at in detail. Fig. 4.9a shows this surface layer, the electron beam direction is from top to the bottom. For the columns consisting of 1-10 Fe-atoms the slope of the phase shift is almost constant, but for the center column, the signal is smaller than expected, also with respect to the value of 2.5 rad of the middle linescan. It would be interesting to see if the slope is the same as it is for the other ones if there would be two columns more, i.e. one center

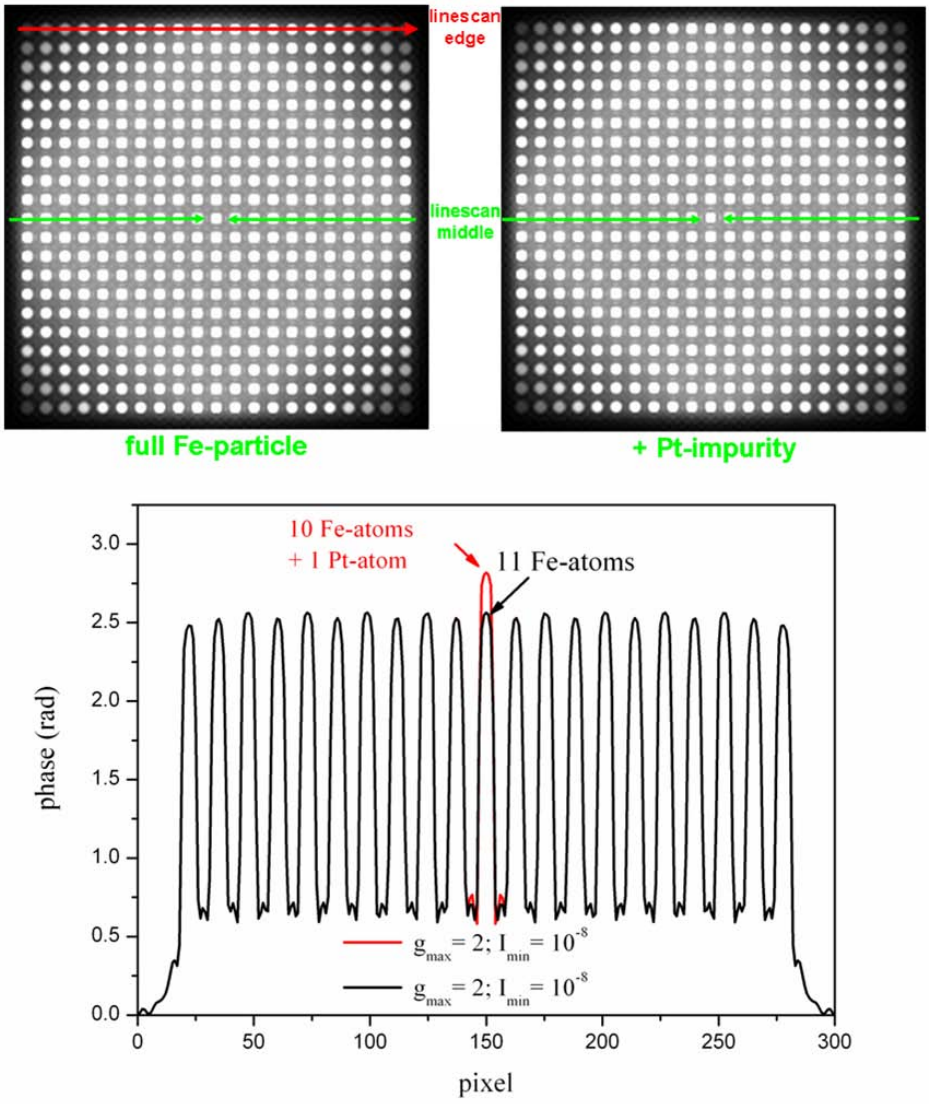


**Figure 4.10:** Simulated phase images for a 10-shell Fe cuboctahedron and phase versus pixel plot of the two middle linescans. The images show the [001]-direction. In the particle on the right the center Fe-atom was replaced by an Pt-atom.

column consisting of 12 and another next to it with 11 Fe-atoms - so that the distribution is symmetric. Then it would be clear if maybe 11 Fe-atoms in a column is a critical size or if it is really an effect based on the surface geometry.
It turns out to be possible to count atoms in the 1-10 Fe atom columns from the magnitude of the phase signal, which has an almost constant phase shift of 0.2rad per atom (9% phase shift from the 9- to 10-atom column). This is a huge difference compared to the shift for the center linescan. There the shift between the 10- to the 11-atom column is 0.05rad, i.e.

2%. This is a perfect example for dynamical scattering and why it has to be considered. Although this last figure suggests that it might be simple to distinguish between different atom numbers in atom columns, there is also another point to mention, the position of the atom columns with respect to the substrate: It will certainly make a difference if there is space between the last atom of the column and the substrate or if the column is touching. This effect was not considered in my simulations.

### Summary

In this section it is demonstrated that quantitative HR-TEM could be used for the determination of the chemical composition of atom columns if the shape of the particle is known. It is shown that due to the effects of dynamical scattering different signals can be observed even when the column composition is identical but the column is located at different positions. Ambiguity of the signal for a specific number of atoms in a column with different compositions is also discussed.

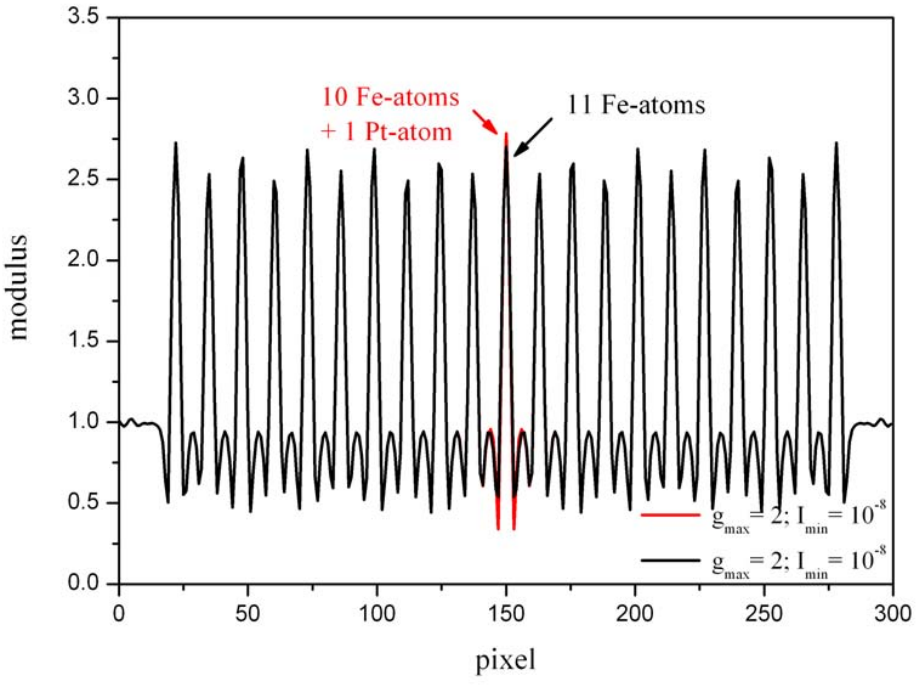


**Figure 4.11:** Modulus of the middle linescans as shown in fig. 4.10.

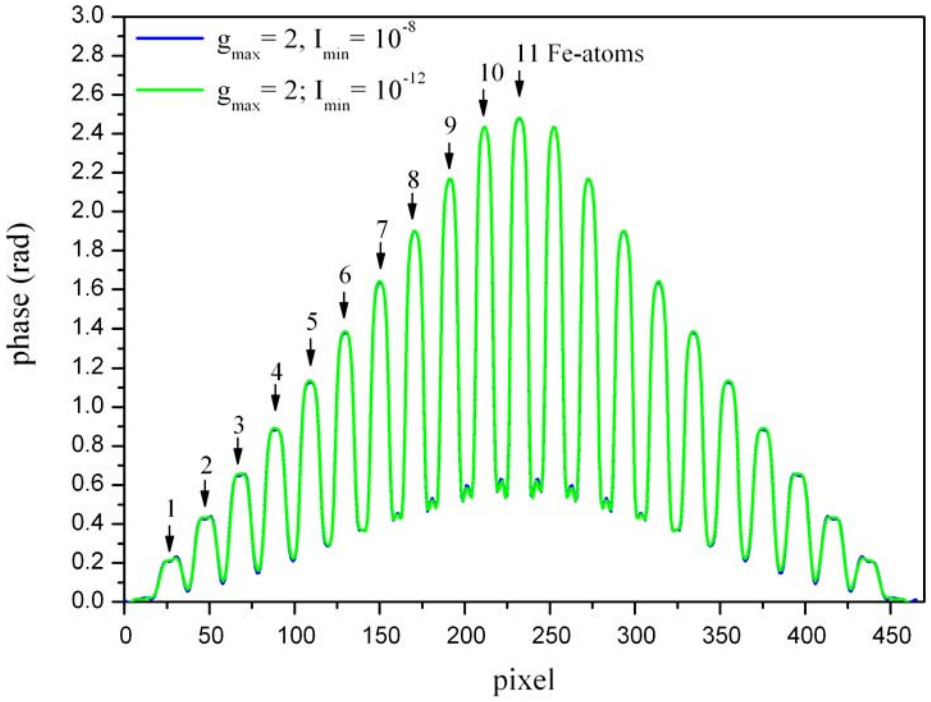


**Figure 4.12:** Phase signal of a 10-shell hollow particle (central shells 0-5 missing). The edge linescan is equal to the one of a full cuboctahedron. The position of the edge linescan is also shown in fig. 4.10.

All these aspects lead to the conclusion that detailed simulations have to be done in order to verify the phase signal. To simplify the simulation process the chemical composition of the particle should be known. From my results I can conclude that the determination of elemental composition from HR-TEM (EWR) phase and amplitude images will be successful only with modeling and simulations.

## 4.3 Cuboctahedra

The samples were prepared as described in section 3.1.1. The nitrogenized particles [Dmi03] are expected to be mostly single crystalline and $L1_0$-ordered (fig. 6.1). Of the approximately 100 nanoparticles imaged, most were orientated in the typical [011]-zone axis or slightly tilted. Only very few were found in the [001]-zone axis and one was observed lying in the [111]-direction. These statements are valid for the Scherzer images taken before the focal series acquisition.

According to [Dmi06a] the EDX analysis yields a composition of 50% Fe and 50% Pt ± 5 at%. The TEM overview image and the associated size distribution are shown in fig. 4.13. The LogNormal fit y = y0 + A/(sqrt(2*p)*w*x)*exp(-(ln(x/xc))$^2$/(2*w$^2$)) yielded y0 = 2.21886 ± 0.78581, xc = 5.73156 ± 0.03166, w = 0.06994 ± 0.00593 and A = 35.55568 ± 2.48644. A mean diameter of 5.73 $nm$ ± 5.5% was obtained.

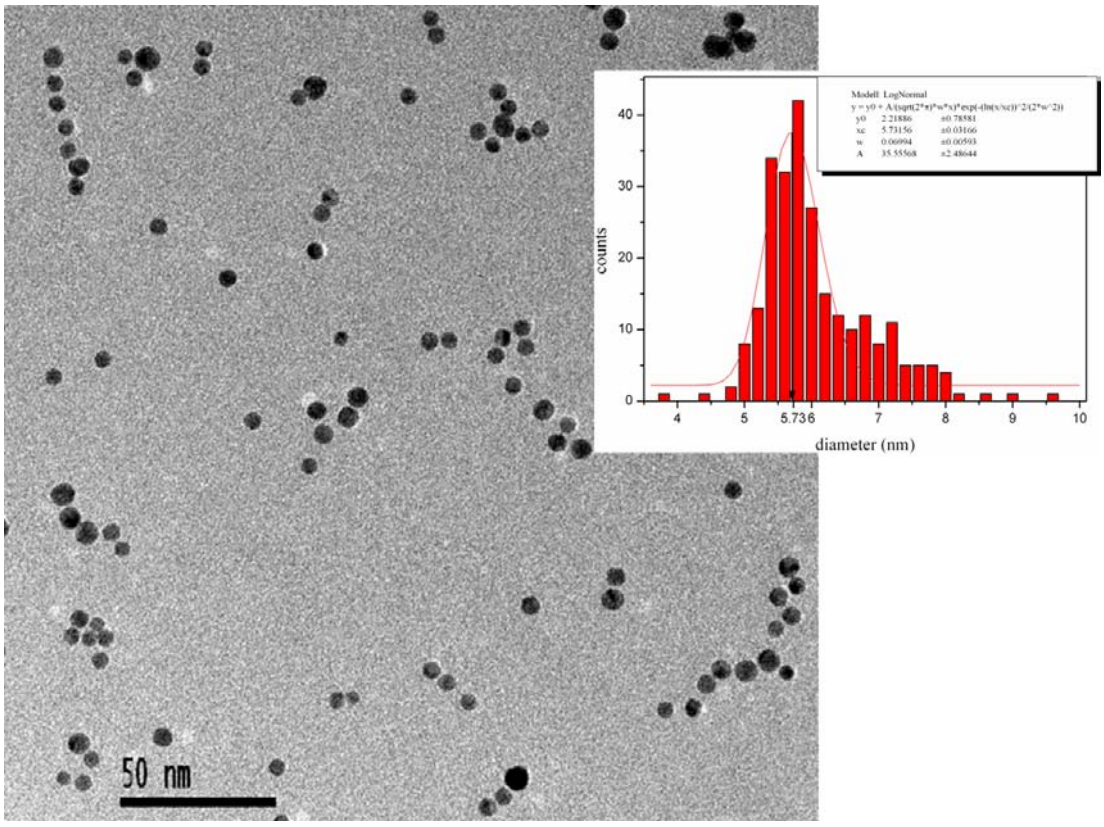


**Figure 4.13:** TEM overview image of the gasphase prepared sample (magnification: 63k) and associated size distribution.

### 4.3.1 Lattice structure

In this section the mean lattice parameter for an ensemble of EWR particles was determined by FFT analysis and compared to the bulk value. Furthermore the mean lattice parameter of one single well-oriented ($L1_0$-ordered) particle (series23) is investigated by the three different methods described in section 4.1. In addition a direction dependent analysis of the lattice parameters **a** and **c** was performed. Furthermore the lattice relaxation for this particle was investigated.
As expected [Sta03c, Dmi03] the lattice structure of the gasphase synthesized particles was observed to be either fcc or fct.

#### Mean lattice parameter a of several gasphase prepared NPs

To determine the mean lattice parameter **a** the EWR images were FFT analyzed. The particles were not stable enough on their zone axis, therefore a direction dependent analysis could not be done and the average over all directions $<\mathbf{a}_{FFT}>$ = 0.397 nm ± 0.9% was determined. These results are also shown in fig. 4.14, with the standard deviation of all measured directions for one series as the error bar. With respect to the FePt bulk value of 0.381 nm the mean value of those series is enlarged by 4.1%.
In more detail, the mean lattice parameter for the six focal series (04, 15*, 16/16*(same focal series, different particles), 17*,19, 21) varies between 0.391 nm < $<\mathbf{a}_{FFT}>$ = 0.397 nm < 0.401 nm. With respect to the bulk lattice parameter this is an enlargement interval from +2.6% to +5.2%. In conclusion every single analyzed particle showed an lattice expansion out of the error bar with respect to the FePt bulk value. The question is if this is a real enlargement or only an artifact due to tilting of the particle.
The influence of tilt to the lattice constant was simulated by J.-O. Malm and M.A. O'Keefe [Mal97]. It was shown that images tilted by 15° yield a mean deviation of more than 1% for the lattice spacing measurement. The minimum and maximum values of single directions showed also deviations up to 10%. They concluded that the power spectrum is a good tool to determine average lattice constants. If the {111} and {200} diffraction spots (see for example fig. 4.16 b)) are not at the correct positions when imaging along the [110]-direction, simulations assuming different structural models to obtain the real crystal structure are required.
The reflection positions and angles between the directions were approximately evaluated to make sure that the structural data of the FFT analysis are related to the real lattice spacings. Consequently only particles with an "almost perfect" power spectrum (FFT pattern), like the "series23" and the "series62" particle, were further investigated to look

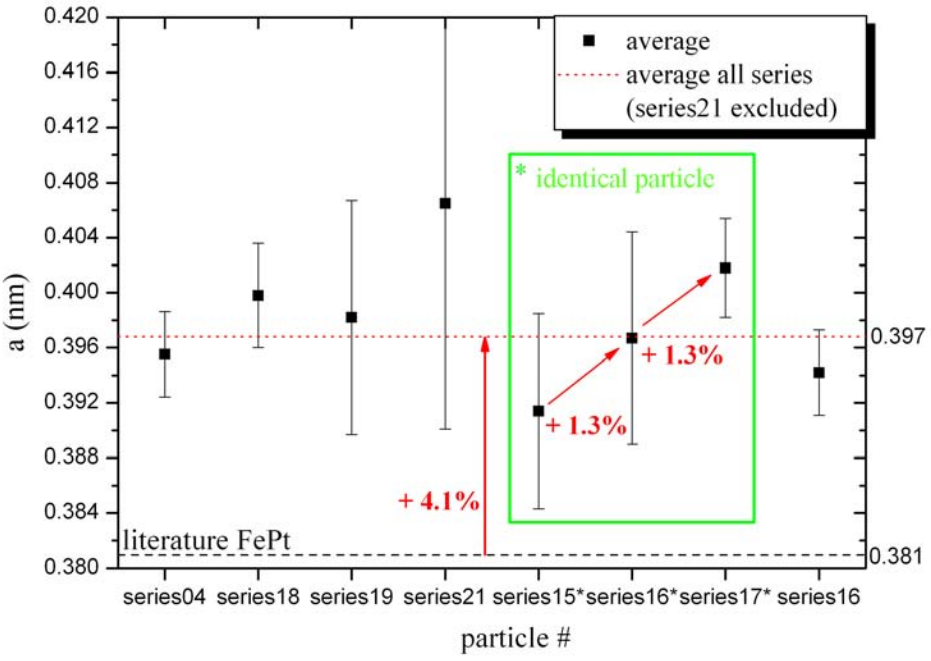


**Figure 4.14:** Mean lattice parameter $<\mathbf{a}_{FFT}>$ (FFT analysis) of different particles on the same substrate - series18 excepted (Scherzer image). The (green) box marks one particle, which was measured in three successive focal series.

for surface-layer relaxations. Therefore small tilting effects are already included in the error bar and the 4.1% expansion of the mean lattice parameter is a real expansion.
Is an expansion of that order specific for nanoparticles because of the smaller surface energy with respect to the bulk or because of the presence of oxygen as discussed for colloidal particles [Tro04], or is it due to the analysis and image acquisition method? If the third point proves true, the next question arises: Is this enlargement effect time dependent, i.e. the longer the particles are investigated under the beam, the larger is the measured lattice constant?

### Time dependence of lattice expansion?

The lattice parameters in fig. 4.14 were analyzed from focal series taken at the same day. For series15* to series17* the same area was illuminated and the same sample could be investigated. Obviously, for that particle, the lattice constant increases from series to series by 1.3%, a hint that expansion might be a function of time. To be able to see a possible

time dependence of the lattice constant the mean lattice parameters obtained by FFT analysis (fig. 4.14) were put in chronological order and linearly fitted, see fig. 4.15. Neglecting that series16 and series16* are different particles recorded in the same focal series the slope is 0.00106nm/series, which would be equivalent to a series dependent increase smaller than 0.3% in the lattice constant. Thus it is smaller than the measured 1.3% of the series15*-series17*. Another point to mention is, that not all series were taken at the same sample position, so the time of beam radiation on the respective sample area is unknown. And although this linear fit has a positive slope, there are successive series where the mean lattice constant decreases with respect to the previous acquired focal series, e.g. series18 to series19. One may conclude that there is no prove for a time dependence of the lattice parameter expansion. This was only assumed for the series15*-series17* nanoparticle, whereas this apparent expansion lies completely within the error bar. Therefore, I conclude that no time dependence of the lattice expansion can be extracted by these data and other explanations as the presence of oxygen have to be considered. Experiments on the possible time dependence of the lattice parameter expansion require that the particle is stable on one zone-axis. The particle should also not lie to close to neighbor particles, so that sintering (see fig. 6.7 in Appendix: Sintering) is avoided [Tro04].

### Direction dependent analysis of the mean lattice parameter

The mean lattice parameter of the well orientated series23 fct particle, see fig. 4.16 is direction-dependently investigated by three methods in this section.
In the FFT-image the superstructure additional diffraction spots are clearly visible. The angles 54.74° ± 0.8% and 35.26° ± 0.8% which are the same for fcc- and fct-structures were measured. This particle is very well oriented in the [011]-zone axis. Table 4.2 shows the lattice constant and the $d_{hkl}$-spacing obtained from the FFT analysis. The error is given by the one-pixel uncertainty. It is maximal 3.8% for the {100}-direction. Within the error range all directions give the same lattice parameter, the mean value of all directions is 0.3864 nm ±1.2%. This value is enhanced by 2.2% with respect to the fcc FePt bulk value. Taking into account that this is a fct-structure, two different values of the lattice parameter have to be determined. In table 6.2 (Appendix) the values are listed for $c/a = 0.96$. For this c/a-ratio the reference value [Lan92] for **a** is 0.385 nm and 0.371 nm for **c**, the [100]-direction, respectively. This consideration results in two new mean values, 0.3817 nm ± 2% for the c-direction, 0.3887 nm ± 1% for the other directions and c/a = 0.98 ± 3%.

The common c/a-values for fct FePt bulk material reported from literature [Thi98, Vis95] are between 0.96 and 0.98. With respect to those values the structure could be identified as fct.

| orientation | $d_{hkl}$ (nm) | resulting a (nm) |
|---|---|---|
| 022 | 0.1377 | $0.3895 \pm 1.4\%$ |
| 011 | 0.2754 | $0.3895 \pm 2.8\%$ |
| 200 | 0.1908 | $0.3816 \pm 1.9\%$ |
| 100 | 0.3817 | $0.3817 \pm 3.8\%$ |
| 111 | 0.2213 | $0.3833 \pm 2.2\%$ |
| 111 | 0.2267 | $0.3926 \pm 2.2\%$ |
| average | - | $0.3864 \pm 1.2\%$ |

**Table 4.2:** Lattice parameters $d_{hkl}$ and $<\mathbf{a}_{FFT}>$ resolved from FFT analysis the of series23 particle.

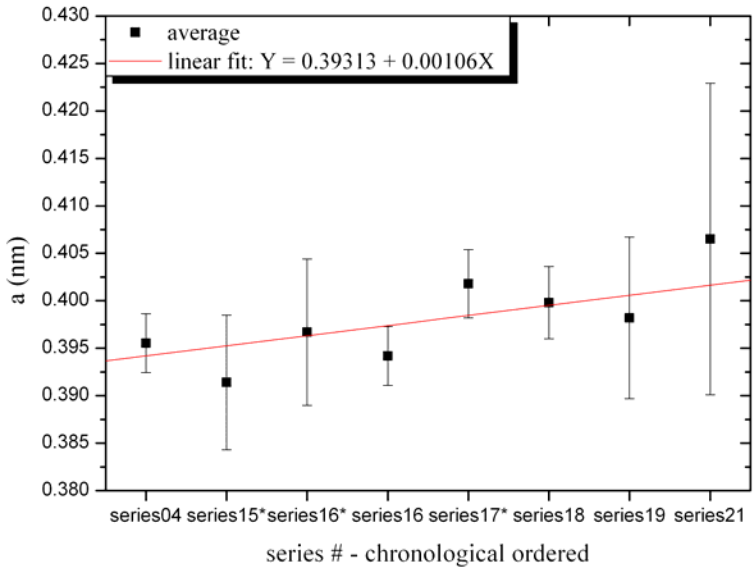


**Figure 4.15:** Lattice parameter as resolved from exit wave reconstructed particles displayed in chronological order of the focal series acquisitions. Series16* and series16 are different particles recorded in the same focal series.

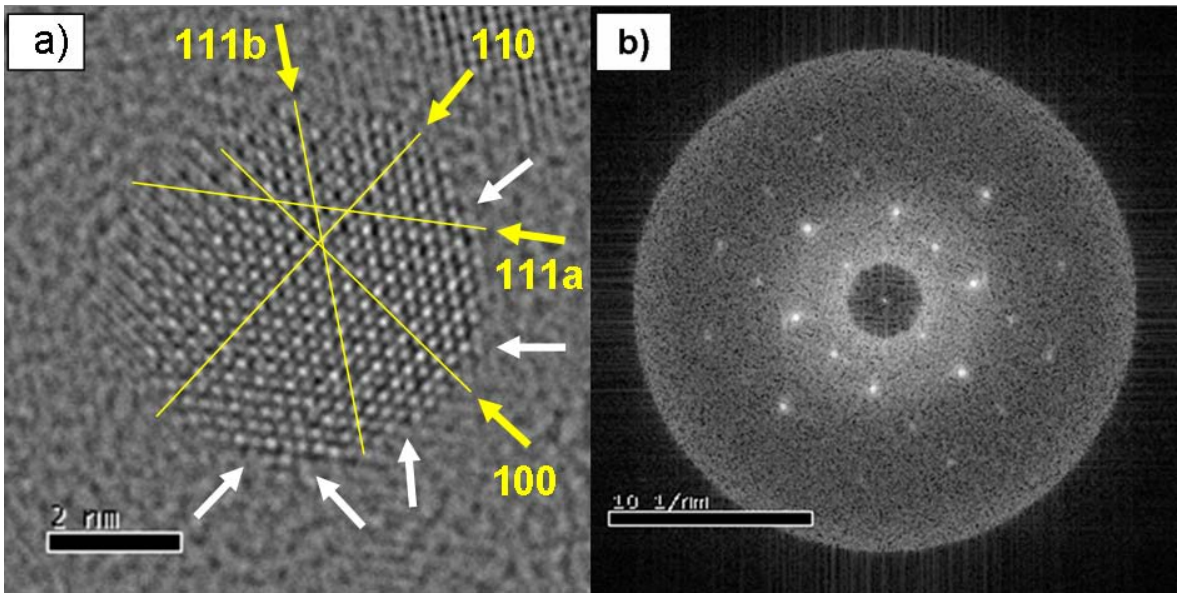


**Figure 4.16:** a) Exit wave reconstructed phase image of one $L1_0$-ordered gasphase particle in [011]-direction. The linescan directions are indicated by (yellow) lines and arrows, the (whites) arrows hint at missing atom columns on the edges. b) FFT of the series23 phase image - the fct superstructure reflections are clearly visible (comp. to fig. 6.6 b) in Appendix).

| direction | $d_{hkl}$ (nm) | **a** (nm) | d(FFT ls) | $\mathbf{a}_{FFT}$ (nm) |
|---|---|---|---|---|
| 100 | 0.1918 | 0.3836 | 0.1915 | 0.3830 |
| 110 | 0.1379 | 0.3900 | 0.1398 | 0.3954 |
| 111a | 0.2233 | 0.3868 | 0.2248 | 0.3894 |
| 111b | 0.2282 | 0.3953 | 0.2248 | 0.3894 |
| all directions | - | 0.3889 $nm \pm 1.3\%$ | - | 0.3893 $nm \pm 1.3\%$ |

**Table 4.3:** Averaged linescan (ls) analysis data of the series24 $L1_0$-ordered particle and average lattice parameter yielded from the FFT of the linescans.

The lattice parameter was not only investigated with this FFT method but also by analyzing linescans in four directions of the phase image (fig. 4.17). Additionally, those linescans were also Fourier transformed. This kind of FFT was done in order to look for relaxation phenomena, which would give more peaks in the spectrum for the relevant spatial frequency interval. As already described in section 4.1 the accuracy in the FFT was not good enough, so that only one frequency - the reciprocal of the averaged lattice spacing - for a whole linescan - was resolved. The results from the linescan and the corresponding FFT are given in table 4.3. For the linescans after 400% magnification of the image the

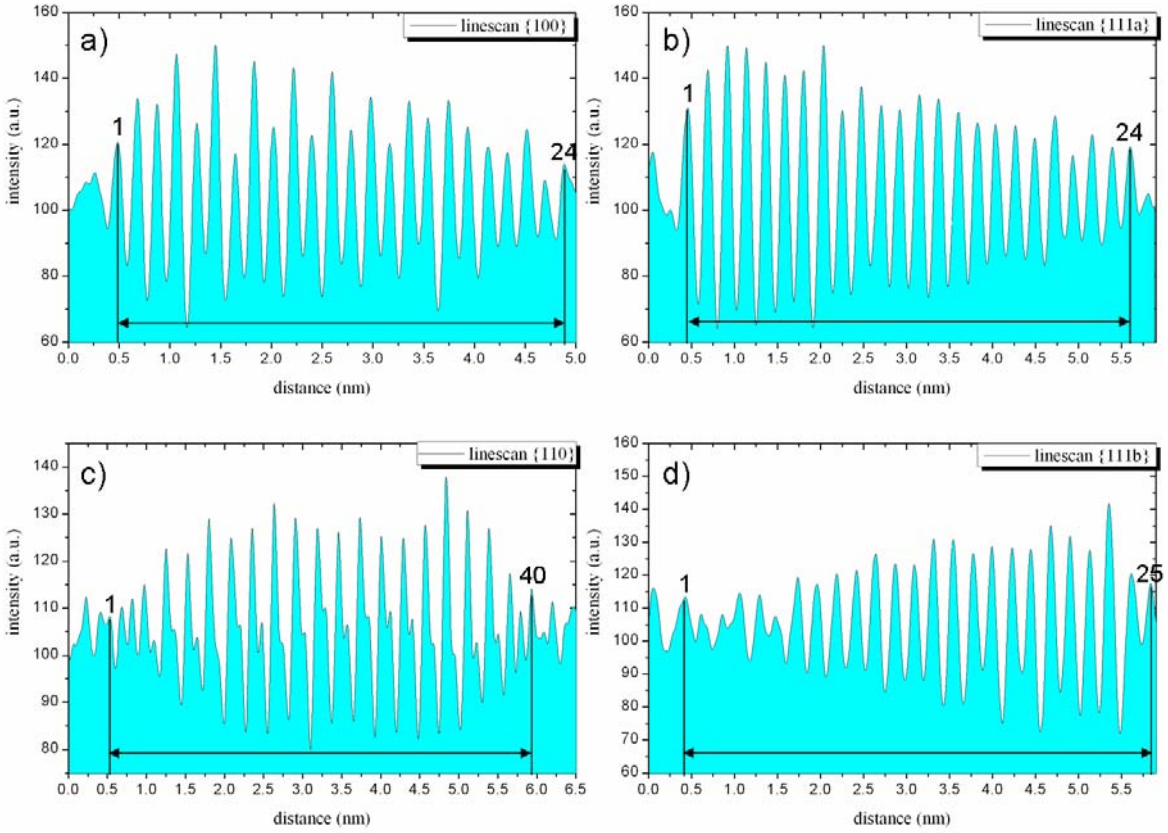


**Figure 4.17:** Viewgraph of the linescans taken in the four directions as indicated in fig.4.16 a). The apparent shift of the Fe sublattice will be shown to be an artefact of the analysis in section 4.3.2.

integration width was chosen as 300 pixel (for a quick investigation) in all directions. The measured spacings in [100]-direction are the spacings between the <200>-layers and the ones in the [110]-direction between the <220>-layers, respectively. The error bar was estimated by comparing two linescans along the same columns. The averaged deviation between those two scans was taken as the error bar, since this error was slightly larger than the value corresponding to one pixel. The error is relevant for the layer-to-layer measurements (next section), see fig. 4.18 but not for the lattice parameter given by the average spacings obtained from all linescan intervals. These measurements averaged over all directions (fig. 4.3) give a mean lattice constant $<\mathbf{a}_{ls}> = 0.3889$ nm $\pm$ 1.3% and $<\mathbf{a}_{FFTls}> =$ 0.3893 nm $\pm$ 1.3%, so it is identical to $a = 0.389\ nm$ within the error and enhanced by 0.6% with respect to the mean value from the FFT analysis of the bright field image.

Also, this analysis of the [100]-direction yields smaller lattice parameters. Distinguishing the **a**- and **c**-direction I find the mean values of <**c**> = 0.3833 nm and <**a**> = 0.3921 nm ± 1.5%. The average of the 110, 111a and 111b values in columns $d_{hkl}$ and $d_{FFT}$ differ by 0.7%. <a> = 0.3921 nm is in the error bar with respect to $<a_{FFT}>$= 0.3887 nm ± 1% from the FFT image analysis. These values are identical. An averaging of the results of all three analyzing methods gives: <a> = 0.391 nm, <c>=0.383 nm and c/a = 0.98 for the particle of fig. 4.16.

### 4.3.2 Surface Layer Relaxation

The series23 particle was investigated in detail to identify a possible surface layer relaxation. For a quick investigation of the surface layer relaxation the same linescans of 300 pixel width as already used for the averaging part were analyzed maximum by maximum. The resulting relaxation is shown in fig. 4.18 and the respective investigated layers are marked in the linescan overview image, see fig. 4.17. Mind that in those two figures a), b) and c) do not stand for the same directions. Along the [100]-direction (fig. 4.18 )a compression behavior for the outermost layers of up to -5% is observed. The mean value 0.192 nm is increased by 3.5% with respect to the FePt bulk value for the fct-phase 0.1855 nm. Similarly to spacings along other directions large variations are also observed in the core. An expansion up to +8% compared to the mean value is found (This layer interval of 0.2075 nm d-spacing is increased by 11.8% with respect to the Pt-bulk value). An unphysically large oscillation of the d-spacing is observed in the [110]-direction. The oscillation varies between ±24% of the mean value which definitely indicates an artifact in the analysis. The reason for this apparently erroneous analysis is discussed below (p. 75).
The mean lattice spacing 0.1379 nm is enhanced by 1.3% compared to FePt in the fct phase and by 0.8% compared to $FePt_3$. The largest spacing values are found in the middle part of the particle whereas the outermost layers are compressed up to 7% with respect to the mean value.
As described before, the linescans along $d_{200}$ and $d_{220}$ do not show a relaxation. Linescan 111a reveals an expansion of the top two layers by 6.5% and a suppression of a similar size on the opposite surface. The mean value 0.223 nm corresponds best to the $FePt_3$ bulk value of 0.2234 nm. From the $L1_0$-structure one would expect the value 0.2195 nm for FePt so the measured mean lattice parameter would be enlarged by 1.8% and the largest spacings by 8.2%. In this direction there was no relaxation tendency to recognize, since there were both compression and extension found for the outermost layers and those values

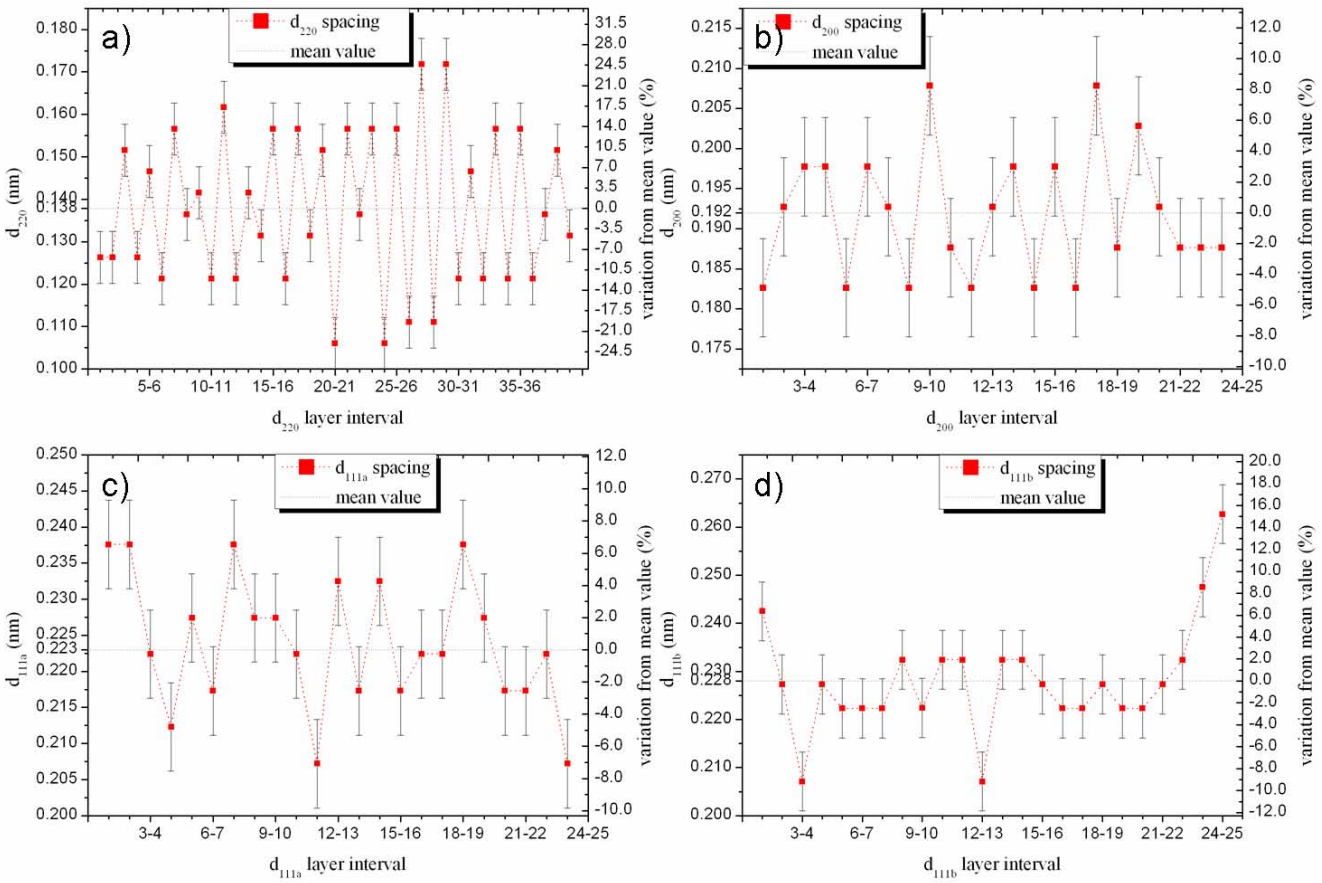


**Figure 4.18:** Layer resolved analysis of the four linescans as indicated in fig.4.16a). Here a) shows $d_{220}$ *spacing*, b) $d_{200}$ *spacing*, c) $d_{111a}$ *spacing* and d) $d_{111b}$ *spacing*. Hereby the indices a and b in the $d_{111}$*spacing* indicate the linescan.

were also found in the core.

The 111b-direction, see fig. 4.18 d), shows surface layer relaxation. The data for the 111b-linescan can also be found in table 4.5 and additionally the ratio of the first four layer intervals for the outermost 5 layers can be found in table 4.6. For gasphase prepared icosahedra a 9.4% outward relaxation of the surface layer compared to the inner layers was measured in 111-direction [Wan06]. In case of the series23 particle an outward relaxation of 6.3% compared to the mean value was measured at one surface (layer interval 1-2).
With respect to $d_{111} = 0.2223\ nm$ which was a typical value for the inner layers this gives a 9.1% outward relaxation - almost the identical value as measured for the icosahedra [Wan06].
The inner layers of this truncated cuboctahedron are mostly slightly extended by 1% with respect to the bulk values (FePt: $d_{111}^{fcc}$=0.2200 nm, $d_{111}^{fct}$ = 0.2195 nm ($c/a = 0.96$)) whereas

this extension is 10.2% for the surface layer. To understand the large variations of the lattice plane spacings one has to consider that the composition in the nanoparticle may not be uniform. There are planes with pure Pt, pure Fe, or mixed composition. Consequently, the spacings will vary due to the different atomic radii of Fe and Pt. In figure 4.19 and table 4.7 different compositions of two successive $< 111 >$-layers are assumed and the resulting spacings for different crystal planes are listed. For the FePt-Pt layer spacing the lattice parameter for $FePt_3$ was used, the one of $FePt_{fcc}$ for the pure Fe-pure Pt layer interval and $FePt_{fct}$ for FePt-FePt accordingly. Fig. 4.16 a) - following the 111b linescan direction - illustrates that the last two measured layers only consist of few atom columns, layer 25 presumably only of one. There are also missing edge atom columns indicated by arrows.

The comparison of the two outermost layer-intervals of the 111b-linescan to bulk d-spacings (table 4.4) shows that even assuming pure Pt-layers at the surface the surface spacing is enlarged at least by 6.9%. Only interval 2-3 is in very good accordance with the Pt-bulk value.

In case of the icosahedra a Pt-surface segregation model was developed to explain the observed relaxation. In conclusion, for the cuboctahedron also surface segregation of Pt may be the origin of the large outward relaxation found in the 111b-direction.

| layer interval | 1-2 | 2-3 | 23-24 | 24-25 |
|---|---|---|---|---|
| $d_{111} - spacing$ (nm) | 0.242 | 0.2273 | 0.2475 | 0.2627 |
| $d_{111}/Fe * 100\%$ | 46.6 | 37.7 | 49.9 | 59.1 |
| $d_{111}/Pt * 100\%$ | 6.9 | 0.4 | 9.4 | 16.1 |
| $d_{111}/FePt_3 * 100\%$ | 8.3 | 1.7 | 10.8 | 17.6 |
| $d_{111}/FePt_{fcc} * 100\%$ | 10.0 | 3.3 | 12.5 | 19.4 |
| $d_{111}/FePt_{fct} * 100\%$ | 10.2 | 3.6 | 12.8 | 19.7 |

**Table 4.4:** Percentage expansion of the outermost $d_{111}$-layer intervals of particle in fig. 4.16 with respect to $d_{111}$ spacings for different $Fe_xPt_{1-x}$ layers (fig. 4.7).

In summary in section 4.3.1 it was shown that this $L1_0$-ordered truncated cuboctahedron has a lattice constant increased by 1.5% for the **a**-direction ($\mathbf{a}_{fct} = 0.385nm$) and by 3.5% for the **c**-direction ($\mathbf{c}_{fct} = 0.371nm$), respectively. The overall expansion of the lattice plane spacing in the **a** and **c** direction cannot be attributed to a "large surface relaxation" - which was not observed. My analysis rather indicates an oscillatory behavior of the lattice parameter within the particle with an enhanced average value. The <111>-surface planes showed an outward relaxation whereas all other directions showed an inward relaxation with respect to the mean as well as to the bulk value.
The observed surface compression of layers may be explained in terms of calculated results of the surface relaxation and electronic structure of Zr(0001)[Yam94]. There an increase in the local density of states for the surface atoms at the Fermi level relative to the bulk atoms was observed. This increase is found to be closely related to the existence of surface states and resonances around the Fermi level. It was shown that the unreconstructed hcp structure of a clean Zr(0001) surface with more than 4% surface layer contraction is the energetically most favorable structure. Accordingly this could be an explanation for the observed contractions of the outermost layers of the nanoparticle and would support the argument that surface tension exerts a compressive stress on nanoparticles. Thus the origin of the outward surface layer relaxation - if it really exists - of the <111>-planes remains an unsolved problem.

| layer interval | $d_{hkl}$ (nm) | variation from mean value (%) |
|---|---|---|
| 1-2 | 0.2425 | 6.3 |
| 2-3 | 0.2273 | -0.4 |
| 3-4 | 0.2071 | -9.2 |
| 4-5 | 0.2273 | -0.4 |
| 5-6 | 0.2223 | -2.6 |
| 6-7 | 0.2223 | -2.6 |
| 7-8 | 0.2223 | -2.6 |
| 8-9 | 0.2324 | 1.8 |
| 9-10 | 0.2224 | -2.5 |
| 10-11 | 0.2324 | 1.8 |
| 11-12 | 0.2324 | 1.8 |
| 12-13 | 0.2071 | -9.2 |
| 13-14 | 0.2324 | 1.8 |
| 14-15 | 0.2324 | 1.8 |
| 15-16 | 0.2273 | -0.4 |
| 16-17 | 0.2223 | -2.6 |
| 17-18 | 0.2223 | -2.6 |
| 18-19 | 0.2273 | -0.4 |
| 19-20 | 0.2223 | -2.6 |
| 20-21 | 0.2223 | -2.6 |
| 21-22 | 0.2273 | -0.4 |
| 22-23 | 0.2324 | 1.8 |
| 23-24 | 0.2475 | 8.5 |
| 24-25 | 0.2627 | 15.1 |

**Table 4.5:** Data for the 111b-linescan.

| (1-2)-(2-3) | (2-3)-(3-4) | (3-4)-(4-5) | (24-25)-(23-24) | (23-24)-(22-23) | (21-22)-(22-23) |
|---|---|---|---|---|---|
| 6.7% | 9.8% | -8.9% | 6.1% | 6.5% | 2.2% |

**Table 4.6:** Relative d-spacings for 111b-linescan.

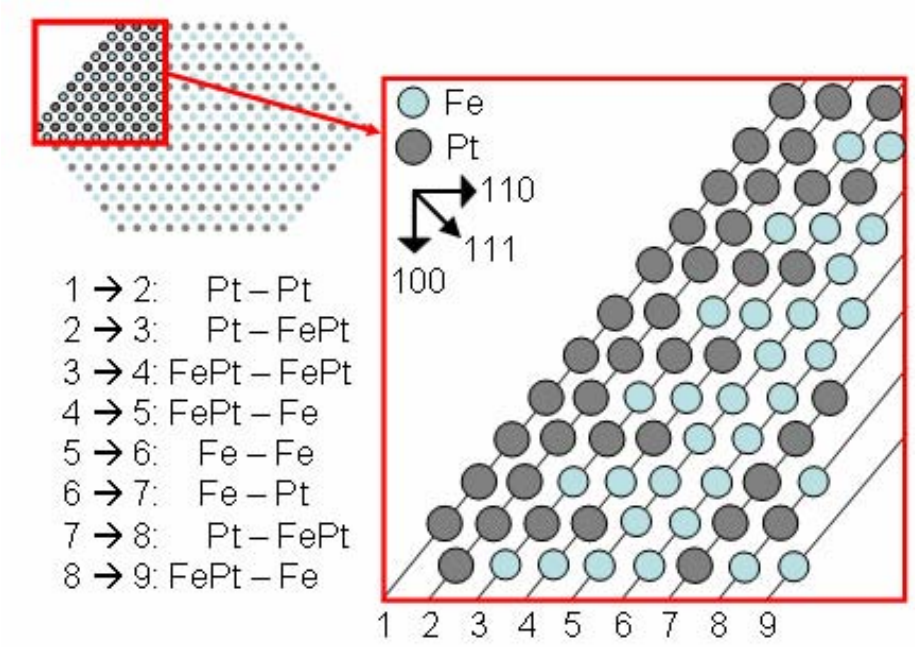


**Figure 4.19:** Schematics of the surface region of a $L1_0$-ordered particle. Different compositions of the top <111>-layers result also in different spacing between the layers. In Table 4.7 the corresponding lattice spacings and constants are given.

| layers | Pt-Pt | Fe-Fe | Pt-FePt | Fe-Pt | FePt-FePt |
|---|---|---|---|---|---|
| phase | fcc | fcc | fcc | fcc | fct |
| $d_{111}$ (nm) | 0.2263 | 0.1651 | 0.2234 | 0.2200 | 0.2195 |
| $d_{001}$ (nm) | - | - | - | - | 0.371 |
| $d_{100}$ (nm) | - | - | - | - | 0.385 |
| $d_{002}$ (nm) | 0.1960 | 0.1430 | 0.1935 | 0.1905 | 0.1855 |
| $d_{200}$ (nm) | 0.1960 | 0.1430 | 0.1935 | 0.1905 | 0.1925 |
| $d_{110}$ (nm) | - | - | - | - | 0.2722 |
| $d_{011}$ (nm) | - | - | - | - | 0.2671 |
| $d_{220}$ (nm) | 0.1386 | 0.1011 | 0.1368 | 0.1347 | 0.1361 |
| $d_{022}$ (nm) | 0.1386 | 0.1011 | 0.1368 | 0.1347 | 0.1336 |
| a($d_{hkl}$) (nm) | 0.392 | 0.286 | 0.387 | 0.381 | 0.385[1] |

[1] 0.371 *nm* for the c-direction (001) respectively

**Table 4.7:** $d_{hkl}$ bulk spacings for $Fe_xPt_{1-x}$ layers. $c/a = 0.96$ for fct.

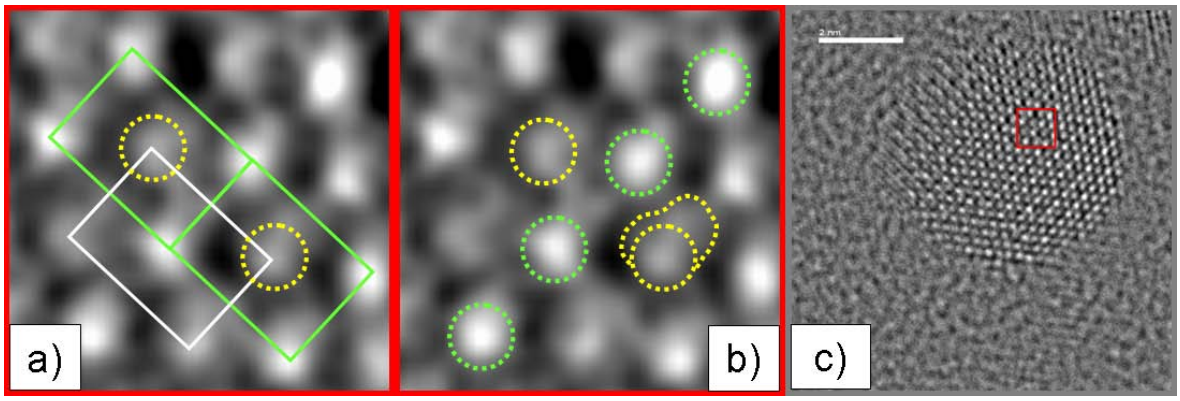


**Figure 4.20:** a), b) Extracted and magnified image of framed part in c). c) Reconstructed phase image of $L1_0$-ordered particle(gasphase).

### Artifacts of analysis

This section deals with a detailed discussion of the double peak structure observed in the [110]-linescan for the series23 particle shown in fig. 4.17 c).
This double peak structure and also the phase image suggest a shift of the Fe <110>-layers to one side with respect to the Pt-layers, that means that the Fe-sublattice would be shifted with respect to the Pt-sublattice. However, this would seem unphysical. In the $L1_0$ superstructure the Fe-layers lie symmetric between Pt-planes (100). One outer layer might consist of more Pt than the corresponding opposite layer resulting in a shift of the Fe-sublattice towards this direction. The intensity (Z-contrast) analysis of the phase image, however, does not allow to confirm this idea. The atomic columns of the outermost layers are not as clearly resolved as those in the middle of the particle. Also the diffractogram (FFT) shows no additional problems either.

Before speculating about physical origins of this unusual apparent shift of the Fe-sublattice in the [110]-direction, a detailed examination of the analysis method was executed. A square in the middle of the particle was magnified, see fig. 4.20 and two unit cells of the Pt-sublattice (green) and one of the Fe-sublattice (gray) were outlined(a). The center of the "Pt-unit cells" is marked with yellow circles. If the Fe-layers were really shifted against the Pt-layers the Fe-columns would not be positioned in the circles. However, they are well centered as expected for the $L1_0$-structure. The intensity distribution is not a circle but something like a circle with a tail - as marked for one column in fig. 4.20 - in one direction (top right) which sometimes even reaches the frame of the Pt-unit cells. This intensity distribution guides the eye to see the position of the Fe-layers closer to the Pt-layers in the top right direction although they are not. For the linescan, which

had an integration width of 300 pixels, this could be a problem as well. The software measures the intensity distribution and weights it over the width of the linescan resulting in a shifted peak for irregular distributions in the intensity linescans, as it was observed for the 110-linescan here. For single layer linescans of only a few pixels integration width, as done for the colloidal series62 particle, this is no problem for the distance measuring, as long as the smearing is uniform in one direction. Even if the maxima are weighted to the wrong positions, the relative distance is not influenced. Thus this possible artifact has to be considered in case of intensity linescans taken over layers staggered against each other. The strongly oscillating lattice spacing measured in the [110]-direction is an artifact and no physical phenomenon.
The origin of the irregular intensity distributions at the atom column position has to be discussed . This effect is stronger for the Fe- than for the Pt-columns. Four explanations are likely:

1. The nanoparticle rotated by a few degrees during the focal series acquisition.
2. The astigmatism and coma free corrections with the exit wave reconstruction software are not optimized at this resolution, or the limit of the reconstruction is already reached.
3. The atoms are not aligned in their columns.
4. This particle might be twinned.

Checking the first and the last image of the focal series confirms point 1. The fringes in the upper part of the particle are an additional hint for assumption 1. Normally, if the particle remains perfectly on zone axis there must not be any fringes left. In conclusiona tilt around the [100]-axis or a twinning have to be considered. The tilt, however, cannot be large because of the high quality of the FFT. To investigate point 3 tomography combined with the acquisition of focal series has to be done. Point2 could not be rechecked at this time.

### Concentration gradient - Pt-enriched surface layers?

In the following section the series23 will be discussed in more detail, in order to see whether there exists a concentration gradient or not. The inner part of the particle has bulk-like $d_{111}$-spacings. For the $L1_0$-order (in [100]-direction), the <220>-layers should consist of alternate pure Fe- and pure Pt-layers which is also evident in the phase image (fig. 4.16a).

However, for the bottom part of the particle the order [Dmi03] seems to be worse compared to the the middle part of the particle. Especially, the last complete surface layer (23 in the 111b-direction) yields a higher Z-contrast (intensity) compared to the inner layers. One would rather expect a flat envelope of the intensity profile, because the number of Pt- and Fe-columns in one <111>-layer should be approximately the same and for the edges the intensity should decrease due to the geometric structure.
This also confirms the model for the Pt-segregation to the surface layers, at least for the end section of the 111b-linescan. At the beginning the noise in the linescan signal was relatively high and the intensity signal weak. Presumably the atom columns in that part of the particle consist mainly of Fe-atoms or of very few atoms.
Also the presence of oxygen as a reason for this relaxation has to be considered [Tro04]. Due to the small Z = 16 of oxygen the phase of the exit wave is hardly visible. XMCD measurements executed in my group yield a surface oxidation of those particles. Due to the surface sensitivity of the x-ray magnetic circular dichroism of approximately 3-4 nm [Ant06a] (in electron yield) it was found, that the particles were oxidized at the surface but not throughout the whole particle. In conclusion an oxidation of the particles could only explain larger surface layer spacings but not the observed oscillatory behavior. Within the framework of my thesis this point could not be investigated further.

### 4.3.3 Summary

In this section it was shown that:

1. The averaged lattice parameter of one particle prepared by gasphase condensation was found to be the same within the errors by three different analysis methods.

2. The averaged lattice constant from several particles $<\mathbf{a}_{FFT}> = 0.397 \pm 0.9\%$ nm is increased by 4.1% with respect to the FePt bulk value, assuming a fcc lattice.

3. Separation for **a** and **c** for one particle shows that a difference as small as 2% in c(0.383 nm) and a(0.391 nm) of a $L1_0$-structure ($c/a = 0.98$) could be resolved.

4. Surface layer relaxation was only observed for the [111]-direction, the layers in other directions rather showed an oscillatory behavior as known from bulk surfaces.

5. Too large integration widths over more than one column might lead to artifacts in the intensity profiles if the reconstruction of the phase image does not yield equally round intensity distributions. In that case deceptive lattice spacings can be measured.

## 4.4 Spherical Chemical Disordered FePt Colloids

In this section the results of the layer resolved investigations for colloidal $Fe_xPt_{1-x}$ nanoparticles (see section 3.1.2) are presented. According to the ratio of the precursors sample MO20 should have a 50% Fe and 50% Pt stoichiometries. This value could not be confirmed by EDX analysis due to charging effects. The large contamination and the charging indicate a presence of organic material (surfactants) although the TEM grids for both samples were washed in acetone to remove dispensable ligands before. The second sample MO10 yielded no homogenous distribution in size and chemical composition. Charging again influenced the EDX measurements. An exemplary ratio of 36% ± 5at. %Fe and 64% ± 5at. %Pt was measured, i.e. the nanoparticles have a composition similar to $FePt_3$. TEM images of both samples are given in fig. 3.2 in the experimental techniques chapter. Sample MO10 was not homogenous in shape and size, the nanoparticles in sample MO20 had a diameter of 2 - 3 nm.

### 4.4.1 Lattice Structure

This section first deals with the determination of the mean lattice parameter from the FFT for both samples and the layer resolved analysis for the series62 particle. From the FFT measurements the fcc structure was clearly identified. One example for a nice FFT is given in fig. 4.21 for the series62 particle. The angles between the reflection spots are in very good correspondence to the literature values for the [011]-direction and deviate by 1.6 % maximal.

Our experiments in Berkeley exhibited a rate of yield for well- reconstructed particles of $10\% - 20\%$ with respect to the total number of acquired focal series. For the MO20 sample the analysis by exit wave reconstruction did not provide improved results with respect to the Scherzer images (section 4.4.1). The Scherzer images of the MO10 sample (fig. 4.22) were analyzed by FFT in addition to the focal series reconstruction to obtain better statistic information.

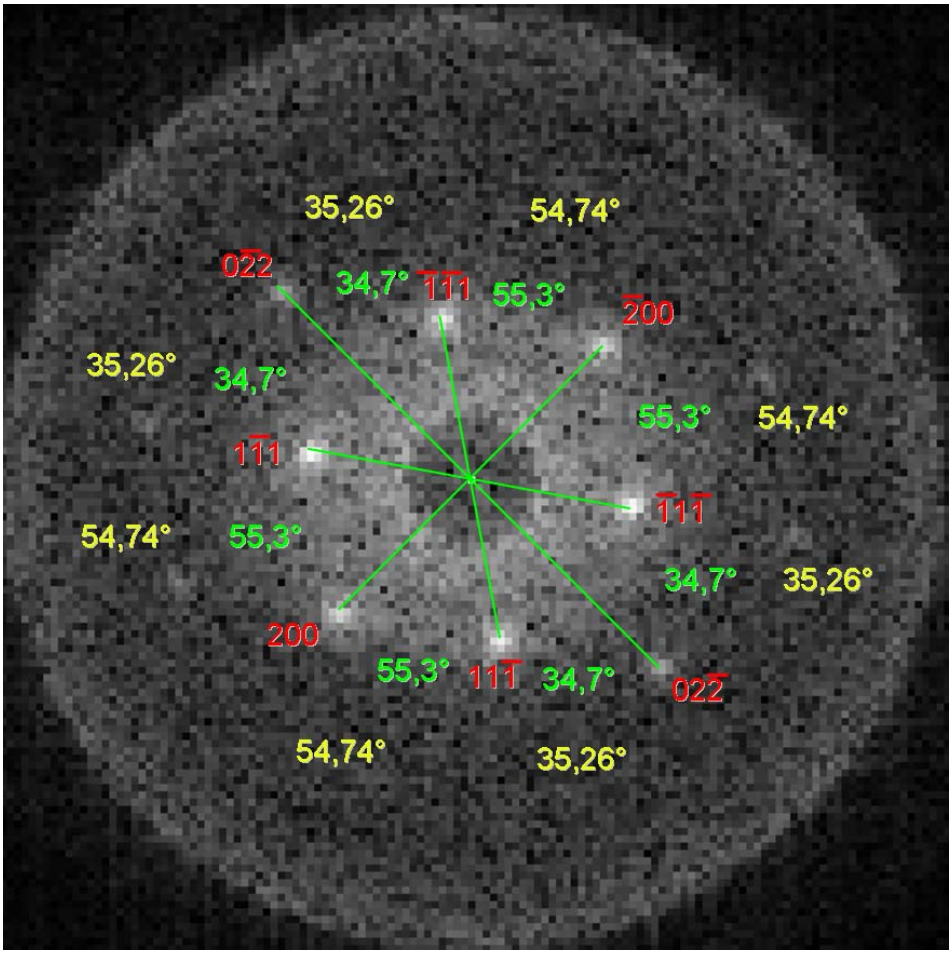


**Figure 4.21:** : fcc phase identification by FFT analysis. FFT image of the series62 particle. The yellow angular values are taken from [Wil96], the green are the measured ones. The reflections are indicated red.

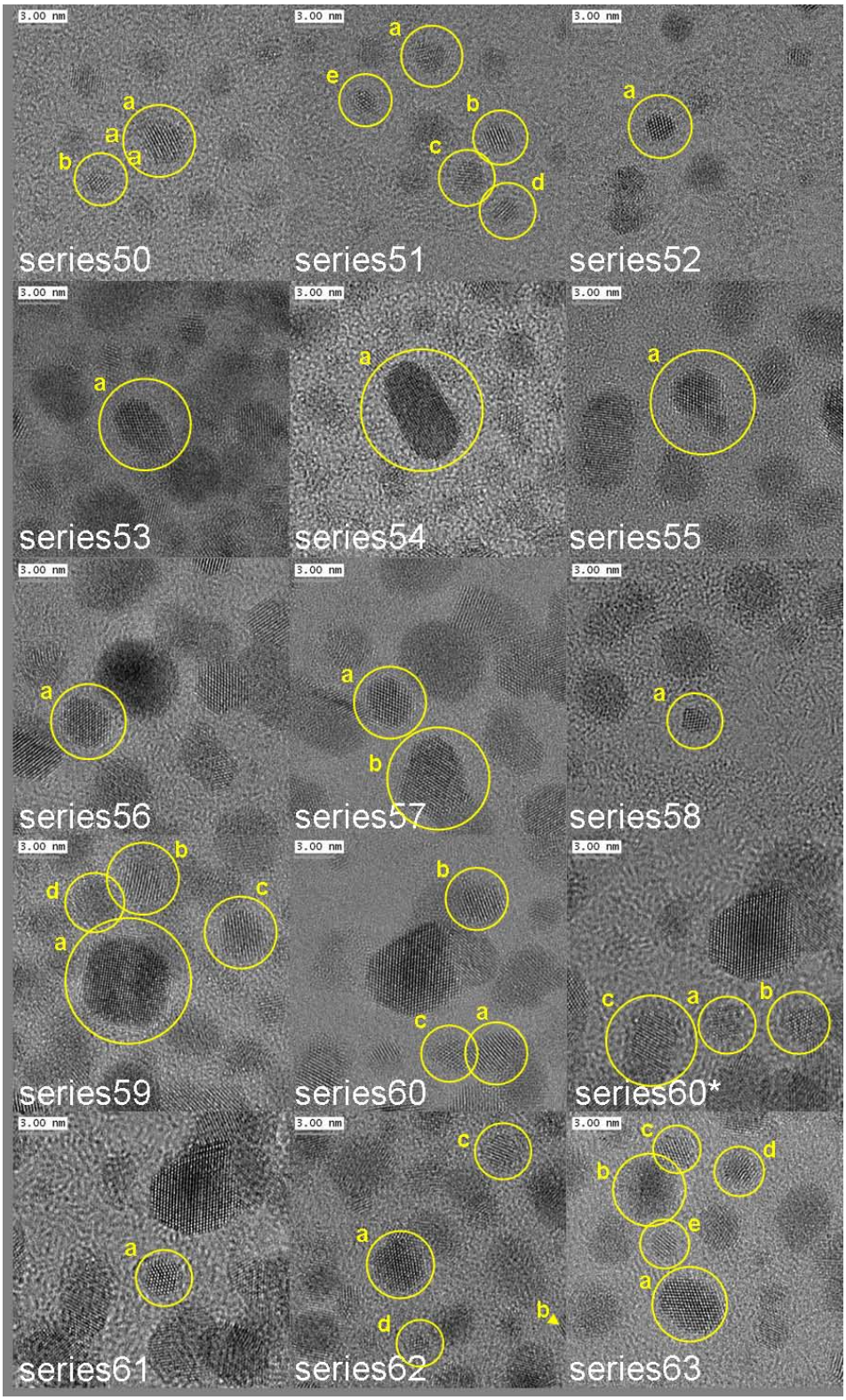


**Figure 4.22:** Overview of the Scherzer images of sample MO10. The yellow circled particles were FFT analyzed, see fig. 4.23.

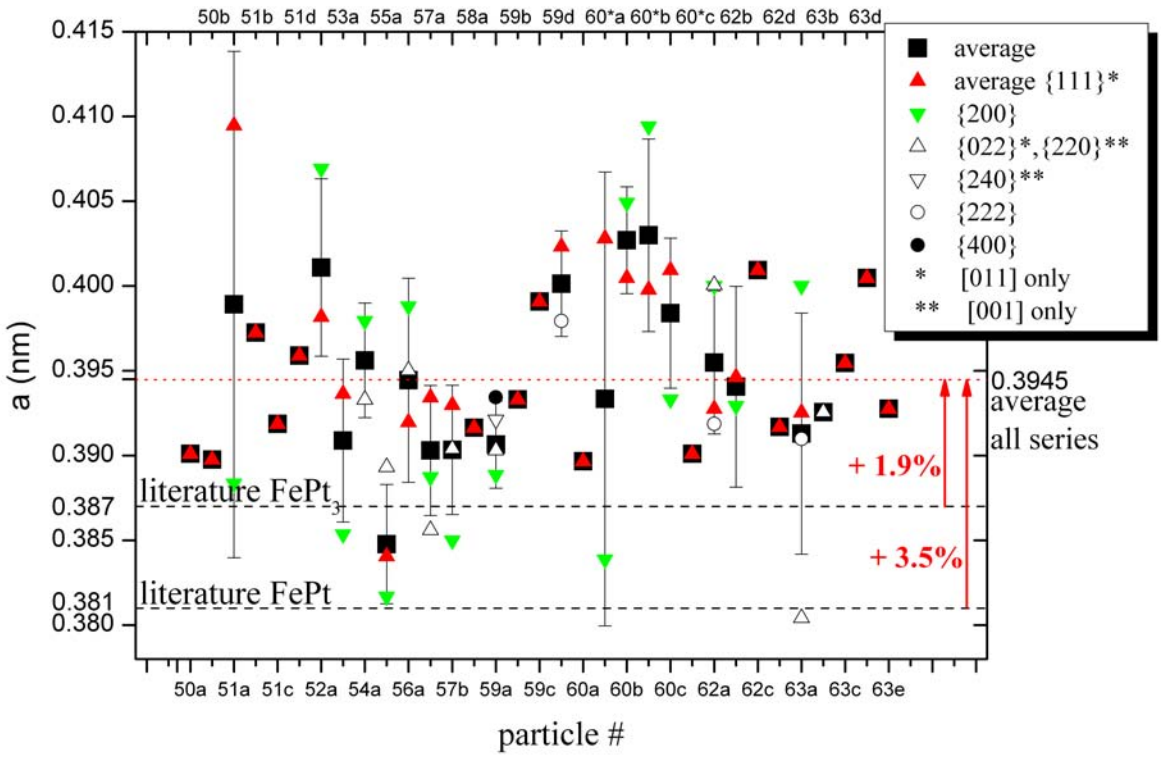


**Figure 4.23:** . Lattice parameter **a** of colloidal particles (fig. 4.22) as resolved from FFT analysis of the Scherzer images.

### Determination of the mean lattice constant

Figure 4.23 displays the results for the FFT analysis of the Scherzer images yielding a mean value of 0.3945 nm ± 1.1 % for the lattice parameter **a**. With respect to the bulk values for FePt and $FePt_3$ this is an enlargement of 3.5% and 1.9%. The FFT analysis of the exit wave reconstructed images leads to a slightly changed result. Compared to the Scherzer value the lattice constant $a = 0.4001\ nm \pm 0.7$ % is enlarged by 1.4 % (fig.4.24). For both cases the mean value of all series was created by averaging all single series mean values and the standard deviation concerning the mean value represents the error bar. The FFT analysis of both the Scherzer images and of the reconstructed images yield an enlargement of the lattice constant with respect to the bulk. The measured lattice constant is even enlarged up to 2.1% with respect to the bulk value for Pt **a** = 0.392 nm [Kit02] (table 4.8).

The two figures 4.22 and 4.24 also display that the values of the lattice constant a for the different directions are not distributed uniformly around the mean value. Therefore the enlargement of the lattice constant is determined to be direction independent. From the FFT analysis of the series62particle a mean lattice constant $<\mathbf{a}_{FFT}> = 0.4019$ nm ± 0.9%

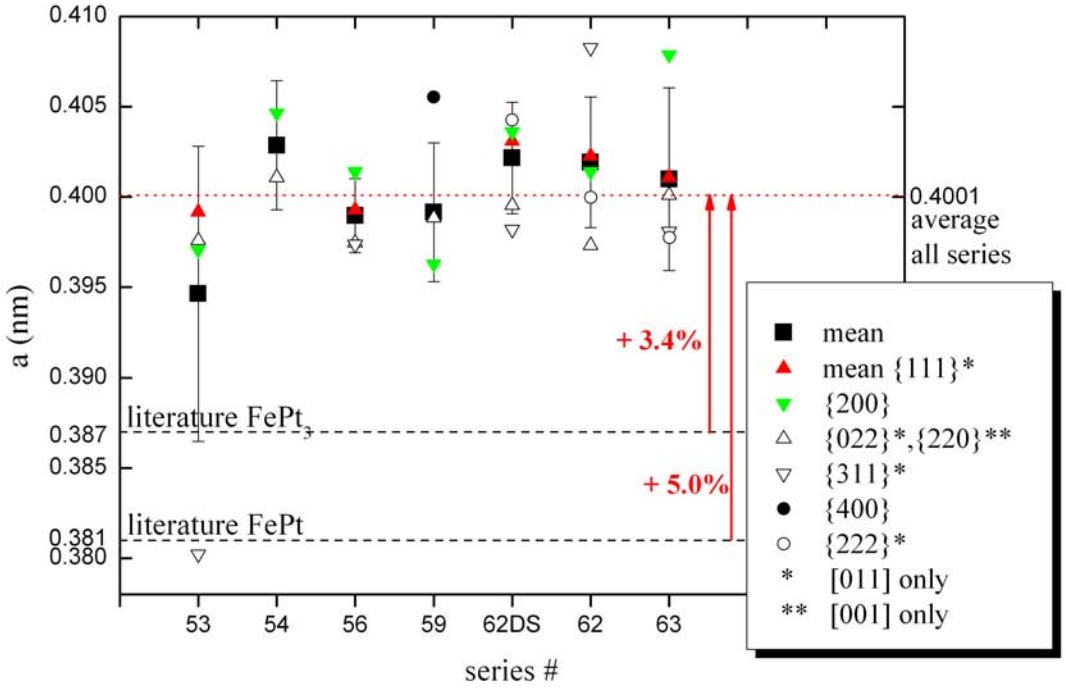


**Figure 4.24:** Lattice constant of colloidal particles averaged over all measured directions in the the FFT of the exit wave reconstructed phase images.

was obtained. Therefore the mean lattice constant is enhanced by 5.5% with respect to the FePt-bulk value and by 3.9% with respect to the $FePt_3$-bulk value. It is also enlarged by 2.5% compared to the lattice parameter for Pt.

### Linescan analysis for the series62 particle

According to the good orientation and quality of the reconstructed phase image of the series62 particle it was further analyzed by linescans. As discussed in section 4.3.2 a large integration width might lead to artifacts, i.e. an averaging of smaller linescans of smaller integration width is preferable. For this particle both methods (large integration width and averaging of smaller integration widths) were performed and compared (table 4.9).

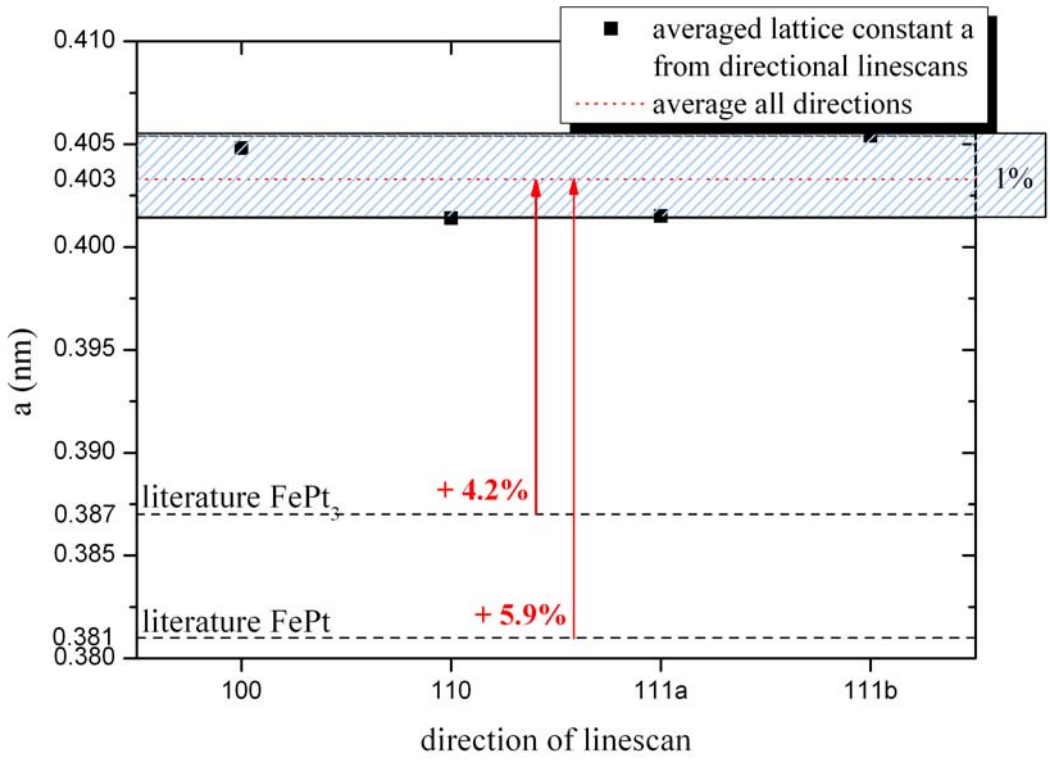


**Figure 4.25:** Averaged lattice constant a of series62 particle as resolved from linescans taken in the four directions indicated in fig. 4.29.

| | | Scherzer | EWR | series62 |
|---|---|---|---|---|
| | average | $0.3945nm \pm 1.1\%$ | $0.4001nm \pm 0.7\%$ | $0.3999nm \pm 0.9\%$ |
| $Fe$ | 0.286 nm | 38% | 39.9% | 39.8% |
| $FePt$ | 0.381 nm | 3.5% | 5.0% | 5.0% |
| $FePt_3$ | 0.387 nm | 1.9% | 3.4% | 3.3% |
| $Pt$ | 0.392 nm | 0.6% | 2.1% | 2.0% |

**Table 4.8:** Percentage value of the lattice parameter as resolved from the FFT analysis of the Scherzer and exit wave reconstructed images and from linescan analysis of the series62 particle compared to different $Fe_xPt_{1-x}$-bulk values [Lan92, Kit02].

The mean value from the linescans with the large integration width (method one) was resolved by dividing the distance between the outermost columns by the number of columns minus one. For the second method (described in more detail in section 4.4.2) all single d-spacings measured for one direction were averaged. That means the standard deviation

with respect to the mean value represents the error bar. In case of a reconstruction with uniform intensity distributions at the positions of atomic columns equal results are expected (see section 4.3.2).

Fig. 4.25 shows the mean values of the lattice constant as obtained from the 4 linescan directions (marked in fig. 4.29) with the larger integration widths (method one). In this case the mean values for each direction vary by 1% maximum. For the other method the largest difference is 3.4%. Apart from the [100]-direction the mean lattice constants determined by the two methods are identical (deviation $< 0.4\%$). This enlargement is due to different numbers of layers covered by the linescans. For the second method an additional "surface layer", which was not detectable in the "method one linescan" was included in the [100]-direction. Neglecting this layer yields a mean lattice parameter of $<\mathbf{a}_{ls}> = 0.4084\text{nm} \pm 5.5\%$, i.e. the deviation to method one becomes smaller than 0.9% for this direction.

The newly calculated mean value for method two $<\mathbf{a}_{ls}> = 0.4041$ nm $\pm$ 0.8% varies by less than 0.2% from the mean value of method one.

| direction | a (nm) | i. w. (pixels) | a* (nm) |
|---|---|---|---|
| 100 | 0.4048 | 400 | 0.4146 $\pm$ 8.4% |
| 110 | 0.4014 | 250 | 0.4009 $\pm$ 2.7% |
| 111a | 0.4015 | 200 | 0.4029 $\pm$ 2.8% |
| 111b | 0.4054 | 300 | 0.4041 $\pm$ 2.0% |
| all directions | 0.4033 $\pm$ 0.5% | - | 0.4056 $\pm$ 1.5% |

**Table 4.9:** Averaged line scan analysis of the series62 particle for four directions (i.w. = integration width). "**a***": Mean lattice parameter **a** from averaging over several linescans of with a l0pixel integration width each.

In conclusion both methods yielded identical mean lattice constants. Furthermore no artifacts in the reconstructed phase image as found in section 4.3.2 have to be considered for the further relaxation investigations of surface layer relaxation (compare also fig. 4.33 e)).

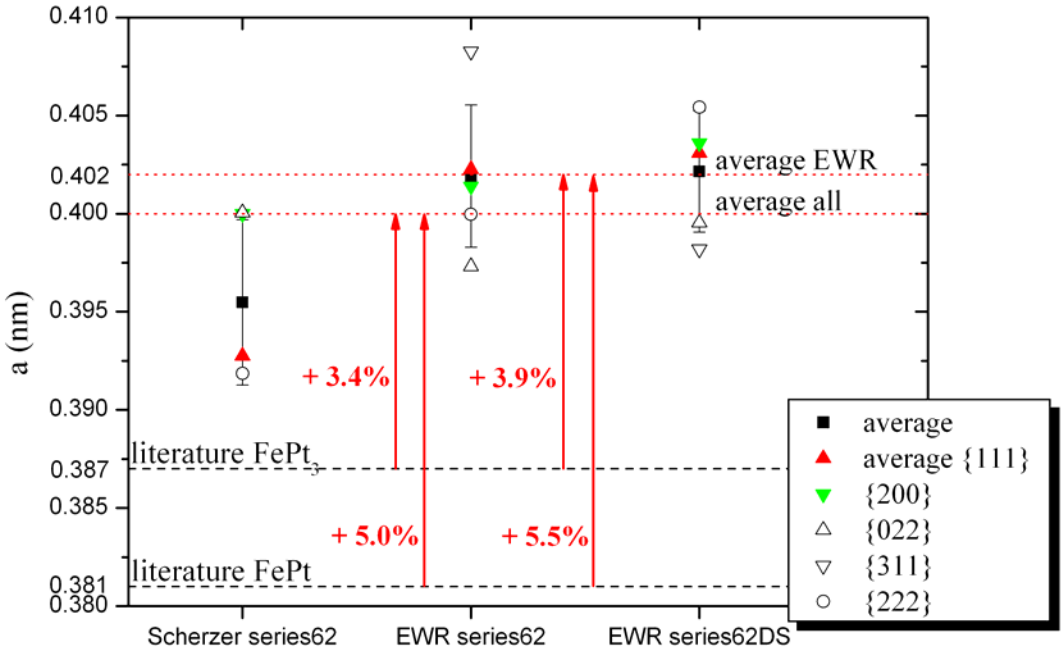


**Figure 4.26:** Lattice constant **a** as resolved from FFT analysis of the Scherzer image and from two different exit wave reconstructions of the same focal series.

### Reproducibility of results

An interesting question is in how far the results obtained from the exit wave reconstructed images are reproducible. To address this question the series62 was reconstructed by D. Sudfeld and me using different parameters, e.g. the amount of PAL/MAL iterations, the number of images and the focal step size. Although the so yielded phase images obtained different intensities (phase values) for the atomic columns the mean value was determined identically ($<\mathbf{a}_{FFT}>$ = 0.402nm ± 0.04 %). The lattice constant obtained from the Scherzer image is $<\mathbf{a}_{FFT}>$ = 0.3955nm ± 1.1% and therefore smaller by 1.6%. This discrepancy of approximately 1.5% between the Scherzer values and the EWR values seems to be systematic (compare section 4.4.1). 1% variation can be explained by the different sampling rates of the images (Scherzer: 0.02 nm/pixel, EWR phase image: 0.0202 nm/pixel), i.e. the real discrepancy is smaller than 0.5%. Following up on this observation and also with respect to the observation for the gasphase particles (section 4.3.1) the question arises again if there is a time dependence due to the electrons since the Scherzer

images were usually acquired before the focal series. This difference, however, is smaller than any error bar and not discussed. As already mentioned before this phenomenon has to be investigated in greater detail, e.g. by successive acquisitions of focal series of the particle. The obtained reconstructed images have to be tested accurately concerning changes in the shape of the particles. Those have to be taken into account when speculating about the reasons for changes in the lattice constant.

### SampleMO20

As mentioned above the exit wave reconstruction yielded no improvement in the images for the MO20 sample. Either the program (TrueImage) had problems with those tiny particles of 2-3 nm diameter or more probably, the particles were not stable enough under the electron beam. Only the analysis of three particles in series27 and not of four as indicated (fig. 4.27) was possible. The particle c in this series shows two directions but could not be indexed in the FFT. The same problem occured in the series32 and series33 analysis. The fringes were too weak to identify them in the FFT image. Therefore another check in the Scherzer images was performed for series32 (indicated as series32S in fig. 4.28).
A FFT analysis of the particles (a, b, d in fig. 4.27) and of the Scherzer image of series32 leads to $<\mathbf{a}_{FFT}> = 0.3987\text{nm} \pm 1.6\%$ (1.6% = standard deviation). The error bars in this analysis are around 4.5% for the single directions, i.e. no accurate determination of the mean lattice parameter was possible. The obtained values, however, hint at an enlargement of the lattice parameter again. The mean value is enlarged by 1.7% even with respect to the Pt-bulk value.

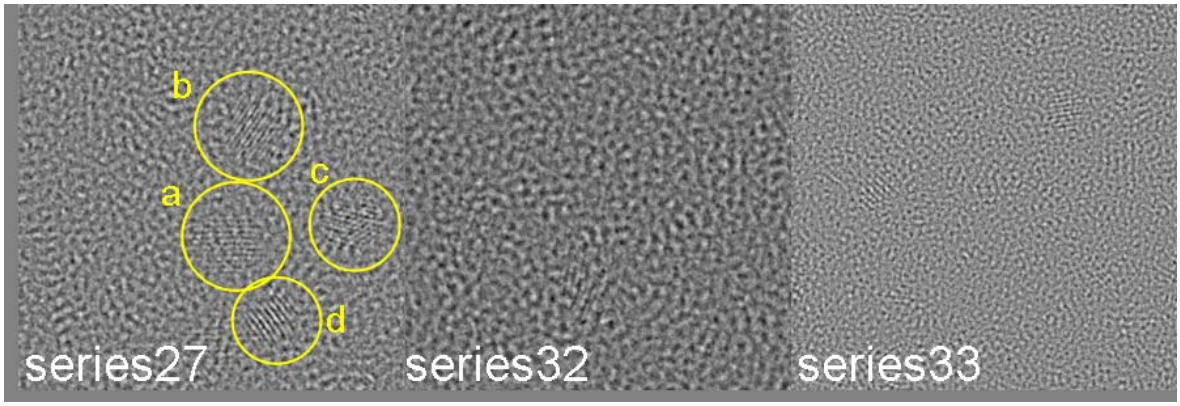


**Figure 4.27:** Overview of the EWR phase images of sample A1. The (yellow) circles in series27 indicate the FFT analyzed particles of this series.

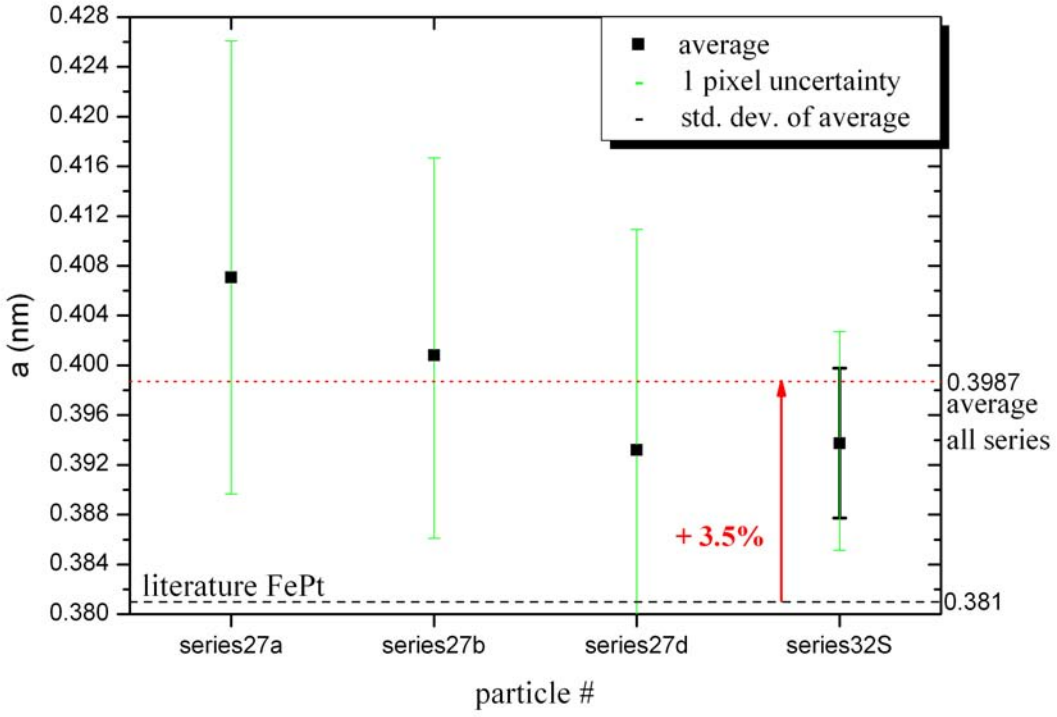


**Figure 4.28:** Mean lattice constant a as averaged out of direction dependent FFT analysis of three particles in series27 EWR phase image (fig. 4.27) and of one particle in the series32 Scherzer image.

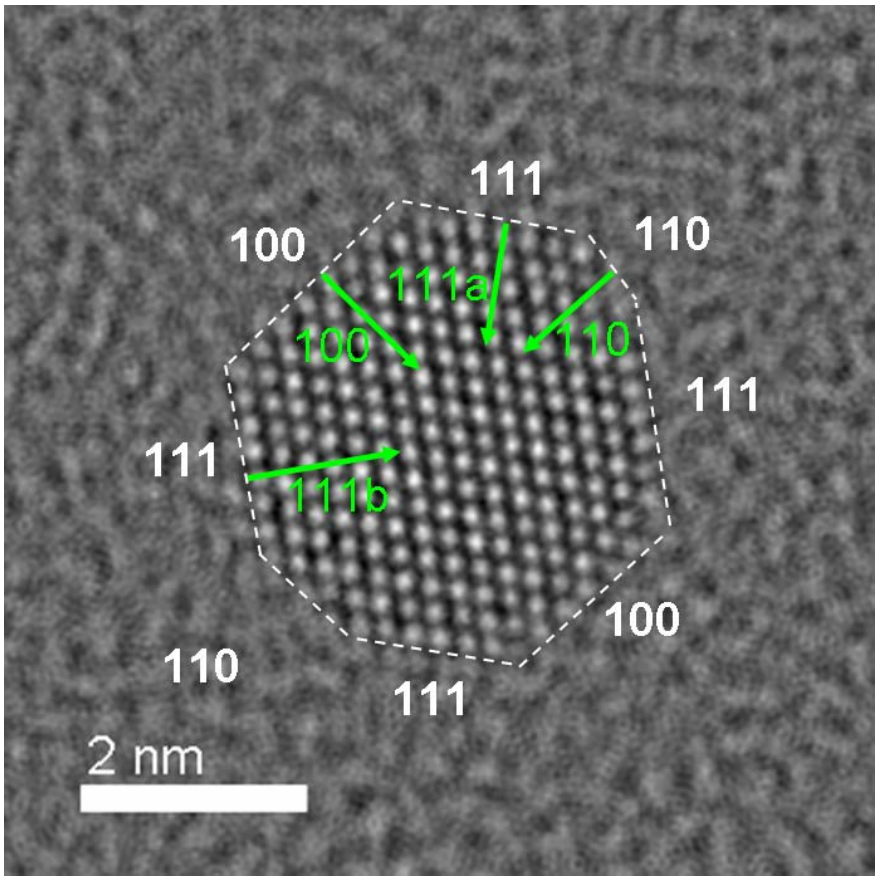


**Figure 4.29:** Indication of the facets of the (colloidal) series62 particle and of the linescan directions for the relaxation analysis.

### 4.4.2 Surface Layer Relaxation

Intensity linescans of an integration width of only ten pixels were taken along all four directions of the series62 particle (fig. 4.29). Due to the the perpendicular directions [110] and [100] the linescans along the [110]-direction are taken along a <200>-layer and those along the [100]-direction along a <220>-layer (fig. 4.30). Every single linescan is marked and numbered in this figure. The $d_{111}$-layers are numbered as well as shown in the two bottom images (111a and 111b d-spacing in fig. 4.30). This numeration of the 111-layers is in accordance to the layer intervals for the relaxation analysis (fig. 4.32 and fig. 4.31). Along the two other directions, [110] and [100] , the layer numbers in one direction are chosen identical to the linescan numbers of the perpendicular direction. (The layer numbers are also marked in 4.32).

The linescans along the 111 directions give the $d_{111}$-spacing multiplied by a factor three, because only every third layer (column) is measured. To directly get the $d_{111}$-spacings from

the linescans either the integration width has to be increased or three or more successive linescans have to be averaged. As discussed in section 4.3.2 a large integration width might lead to artifacts in the determination of the $d_{hkl}$-layer spacing. Therefore a number of adjacent 10pixel width linescans of the same length and all covering the same number of layers was averaged (fig. 4.31) and further investigated. The resulting $d_{hkl}$-layer spacings are shown in fig. 4.32.

The error bars for the single d-layer spacings are due to the 1-pixel uncertainty. For the mean values of the d-layer spacings and the lattice parameter, respectively, the standard deviation represents the error bar. For the [100]-direction the linescans 8-18 were averaged and the layer to layer distances determined. The results for this and the two [111]-directions are shown in table 4.10. The numbers of the layers are not in conformity with those marked in fig. 4.30. Layer number 1, in [100]-direction, in this sketch is identical to layer number 2 for the relaxation investigations. In conclusion layer number 20 in the investigation is identical to layer number 19 in the sketch. In fig. 4.31 c) this is indicated. The red numbers (1-19) show the numeration in the sketch and the black ones (1-20) show the numeration used for the relaxation analysis.

The additional "layer" was discovered in the averaged [200]-linescan and was not recognized by eye in the phase image, i.e. the intensity (phase signal) is weak. DERIP did not detect this "layer" as shown in fig. 4.33 f) either. Varying the contrast, shown in the same figure a)-c), yields at least two additional outermost atom columns (new "layer" one - best visible in c)), i.e. this layer is not complete, several atom columns are missing.

It is not clear if it has ever been complete. The atom columns could have also been moved from other positions of the particle, e.g. from the edges of two surface layers. The significant missing of edge atomic columns is reported in literature, e.g. [Wan06] and was also observed for this particle.

According to the phase signal (intensity) the additional "layer" either contains only a few atoms or the layer consists mainly of Fe, due to the smaller Z-contrast. Again, the presence of oxygen has to be considered, too.

Taking the additional layer into account a mean value of $<\mathbf{a}_{ls}> = 0.207$ nm $\pm$ 8.3% is resolved. With respect to this mean value layer interval 1-2 is increased by 26.7%. The other outermost layer interval 19-20 is enlarged by 14.5% but in this case, apart from the edge columns, layer 20 is complete. Neglecting the outermost layer intervals on both sides of the particle the mean value can be calculated to 0.2023 nm $\pm$ 4% which is equal to a lattice parameter of 0.404 nm $\pm$ 4%. The layer intervals between layer 3 and 17 vary around 0.202 nm $\pm$ 2.4%. With respect to this value layer interval 17-18 is compressed by 10%. This interval, however is the only one with $d_{200}$-layer spacing of 0.1818 nm. Compared to

the $FePt_3$ bulk value $d_{200}^{fcc} = 0.1935$ nm [Lan92] it is compressed by -6%. The other layer intervals deviate by +4.4% from this value and by 3% from the Pt bulk value $d_{200}^{fcc} = 0.196$ nm [Kit02].
In conclusion for the [100]-direction a surface layer relaxation up to 26.4% was observed with respect to the mean d-layer spacing, whereas mostly all the inner layer spacings diversify around a mean value which is increased by 3% with respect to the Pt bulk value.

| layer interval | $d_{200}$ (nm) | $\Delta$ (%) | $d_{111a}$ (nm) | $\Delta$ (%) | $d_{111b}$ (nm) | $\Delta$ (%) |
|---|---|---|---|---|---|---|
| 0-1 | - | - | 0.2424 | 4.3 | 0.2374 | 1.8 |
| 1-2 | 0.2626 | 26.7 | 0.2374 | 2.1 | 0.2374 | 1.8 |
| 2-3 | 0.2121 | 2.3 | 0.2171 | -6.6 | 0.2273 | -2.6 |
| 3-4 | 0.2070 | -0.1 | 0.2424 | 4.3 | 0.2373 | 1.8 |
| 4-5 | 0.2020 | -2.6 | 0.2272 | -2.3 | 0.2323 | -0.4 |
| 5-6 | 0.1969 | -5.0 | 0.2374 | 2.1 | 0.2323 | -0.4 |
| 6-7 | 0.2070 | -0.1 | 0.2323 | -0.1 | 0.2373 | 1.8 |
| 7-8 | 0.1970 | -5.0 | 0.2272 | -2.3 | 0.2273 | -2.6 |
| 8-9 | 0.2020 | -2.6 | 0.2272 | -2.3 | 0.2323 | -0.4 |
| 9-10 | 0.1969 | -5.0 | 0.2374 | 2.1 | 0.2323 | -0.4 |
| 10-11 | 0.2020 | -2.6 | 0.2272 | -2.3 | 0.2323 | -0.4 |
| 11-12 | 0.1970 | -5.0 | 0.2323 | -0.1 | 0.2273 | -2.6 |
| 12-13 | 0.2121 | 2.3 | 0.2323 | -0.1 | 0.2373 | 1.8 |
| 13-14 | 0.2020 | -2.6 | 0.2323 | -0.1 | 0.2273 | -2.6 |
| 14-15 | 0.1970 | -5.0 | 0.2323 | -0.1 | 0.2323 | -0.4 |
| 15-16 | 0.2071 | -0.1 | 0.2272 | -2.3 | 0.2424 | 3.9 |
| 16-17 | 0.2020 | -2.6 | 0.2424 | 4.3 | - | - |
| 17-18 | 0.1818 | -12.3 | 0.2323 | -0.1 | - | - |
| 18-19 | 0.2171 | 4.7 | - | - | - | - |
| 19-20 | 0.2374 | 14.5 | - | - | - | - |

**Table 4.10:** Data from 100- and 111-linescan analysis. # of layer interval as given in fig. 4.32. $\Delta$ : variation from mean value.

| layer interval | layer interval* | $d_{hkl}$ (nm) | $\Delta$ (%) |
|---|---|---|---|
| 0.5-1.5 | 1-3 | 0.2828 | -0.3 |
| 1-2 | 2-4 | 0.2677 | -5.6 |
| 1.5-2.5 | 3-5 | 0.2979 | 5.1 |
| 2-3 | 4-6 | 0.2828 | -0.3 |
| 2.5-3.5 | 5-7 | 0.2778 | -2.0 |
| 3-4 | 6-8 | 0.2879 | 1.5 |
| 3.5-4.5 | 7-9 | 0.2828 | -0.3 |
| 4-5 | 8-10 | 0.2828 | -0.3 |
| 4.5-5.5 | 9-11 | 0.2828 | -0.3 |
| 5-6 | 10-12 | 0.2778 | -2.0 |
| 5.5-6.5 | 11-13 | 0.2828 | -0.3 |
| 6-7 | 12-14 | 0.2878 | 1.5 |
| 6.5-7.5 | 13-15 | 0.2878 | 1.5 |
| 7-8 | 14-16 | 0.2828 | -0.3 |
| 7.5-8.5 | 15-17 | 0.2778 | -2.0 |
| 8-9 | 16-18 | 0.2777 | -2.0 |
| 8.5-9.5 | 17-19 | 0.2879 | 1.5 |
| 9-10 | 18-20 | 0.2879 | 1.5 |
| 9.5-10.5 | 19-21 | 0.2777 | -2.0 |
| 10-11 | 20-22 | 0.2878 | 1.5 |
| 10.5-11.5 | 21-23 | 0.2929 | 3.3 |
| 11-12 | 22-24 | 0.2727 | -3.8 |
| 11.5-12.5 | 23-25 | 0.2778 | -2.0 |
| 12-13 | 24-26 | 0.2979 | 5.1 |
| 12.5-13.5 | 25-27 | 0.2980 | 5.1 |
| 13-14 | 26-28 | 0.2879 | 1.5 |
| 13.5-14.5 | 27-29 | 0.2727 | -3.8 |
| 14-15 | 28-30 | 0.2778 | -2.0 |

**Table 4.11:** Data from the 110-linescan analysis. Layer interval: layer interval with respect to fig. 4.32. Layer interval*: layer interval with respect to the layer numbers marked in fig. 4.30. $\Delta$: variation from mean value.

For the [111]-directions a significant surface layer relaxation was not observed (fig. 4.31 and table 4.10). The lattice layer spacings randomly spread around the mean value. The maximum variations from the mean value are +4% for the 111b-direction and -6.6% for the 111a-direction. In case of the 111b-directions apart from the d-layer spacing of interval 15-16, the value of the other surface layer spacing can be also found in the core of the particle. In this direction for both surface layers the next layer spacing is increased with respect to the mean value. Remarkable is the lattice spacing decrease from layer 15-16 down to layer interval 13-14 by -6.6% over this distance. A similar trend can be found for the layer intervals 19-20 down to 17-18 in the 100-direction and for the layer intervals 0-1 up to 2-3 for the 111a-direction, respectively. For the second direction the decrease is -11.6%. These outermost layer spacings can be also found in the middle part of the particle. The mean curve of all given linescans in the [110]-direction has a profile which is not interpretable because the local peak shape of the maxima is not unique. Caused by this, the arithmetic mean value could not be determined (see average curve in fig. 4.31d)). It is easy to find that all intensity peaks are shifted randomly against each other. A separate averaging of the even numbered and of the odd numbered linescans was done. Those averaged linescans yielded the $d_{110}$-layer spacing because only the next but one layers were measured. In fig. 4.32d) both obtained results were plotted. This leads to a strange numbering of the layer intervals. It is corrected in table 4.11 with respect to the linescan numbers in [100]-direction extended by two additional layers non-marked in the image.
The results for the [110] direction differ from those of the other three directions since the outermost layer intervals have approximately the values of the mean layer spacing ($d_{110}$ = 0.2835 nm).
The largest $d_{110}$-layer spacings ($d_{110}$ = 0.298 nm) are found for the non surface layer intervals 3-5, 24-26 and 25-27. These values are enlarged by 5.1% with respect to the mean value. Besides, the outer layer intervals are compressed, e.g. 2-4 by -5.6%. A similar behavior can be found for the layer intervals 27-29 and 22-24 which are compressed by -8.9% with respect to the adjacent intervals 25-27 and 24-26, respectively. These correlations hint at a movement of atom columns in the common layers 27 and 24 towards one preferential side each. Indeed larger spacings (dark areas) can be seen in fig. 4.29 regarding the area below the "111b-arrow". Due to the *mean* - along several atom columns - lattice spacings yielded from the averaged linescans a direct transfer of the obtained spacing information to the phase image is not possible.
Therefore every linescan has to be analyzed separately to determine the d-layer spacing which could not be performed in this thesis.
The different spacings can be attributed to the different stoichiometry of Fe and Pt atoms

in the columns. Figure 4.33 a)-d) shows the identical phase image with different contrasts. Image a) displays the different chemical compositions of the atomic columns. Pt rich columns can be identified by a brighter phase signal. It becomes obvious that the brightest columns are distributed randomly within the particle, whereas the surface layers preferably include columns of weaker intensity. This effect is also induced by the almost perfect truncated octahedron-like structure of the particle. Due to this structure for a particle of uniform chemical distribution the phase signal is equal for the center columns and declines approaching the facets of the particle. An example of such an intensity profile was found in fig. 4.31 b). The small variations are due to the non uniform stoichiometry and the number of atoms in one column.

| direction | 100 | 110 | 111a | 111b |
|---|---|---|---|---|
| average | 0.4146 nm ± 8.3% | 0.4009 nm± 2.7% | 0.4029 nm±2.8% | 0.4041 nm ± 2.0% |
| $Fe_{100}$ | +45% | +40.2% | +40.9% | +41.3% |
| $Fe_{50}Pt_{50}$ | +8.8% | +5.2% | +5.7% | +6.1% |
| $Fe_{25}Pt_{75}$ | +7.7% | +3.6% | +4.1% | +4.4% |
| $Pt_{100}$ | +5.8% | +2.3% | +2.8% | +3.2% |

**Table 4.12:** Percentage value of the lattice parameter as resolved from the linescan analysis of the series62 particle compared to different $Fe_xPt_{1-x}$-bulk values [Lan92, Kit02].

### 4.4.3 Summary

For the spherical colloidal particles in this section the following can be concluded:

1. A detailed FFT analysis of the reconstructed phase images revealed a mean lattice constant of 0.400 nm which is enlarged by 3.4% with respect to the $FePt_3$ bulk value.

2. Not conform to the expectation that nanoparticles consist of Pt-enriched surfaces, a lattice relaxation was only observed for the 100-direction, the layers in other directions rather showed random distributions.

3. Pt-segregation to the surface layers could not be confirmed by the experimental data.

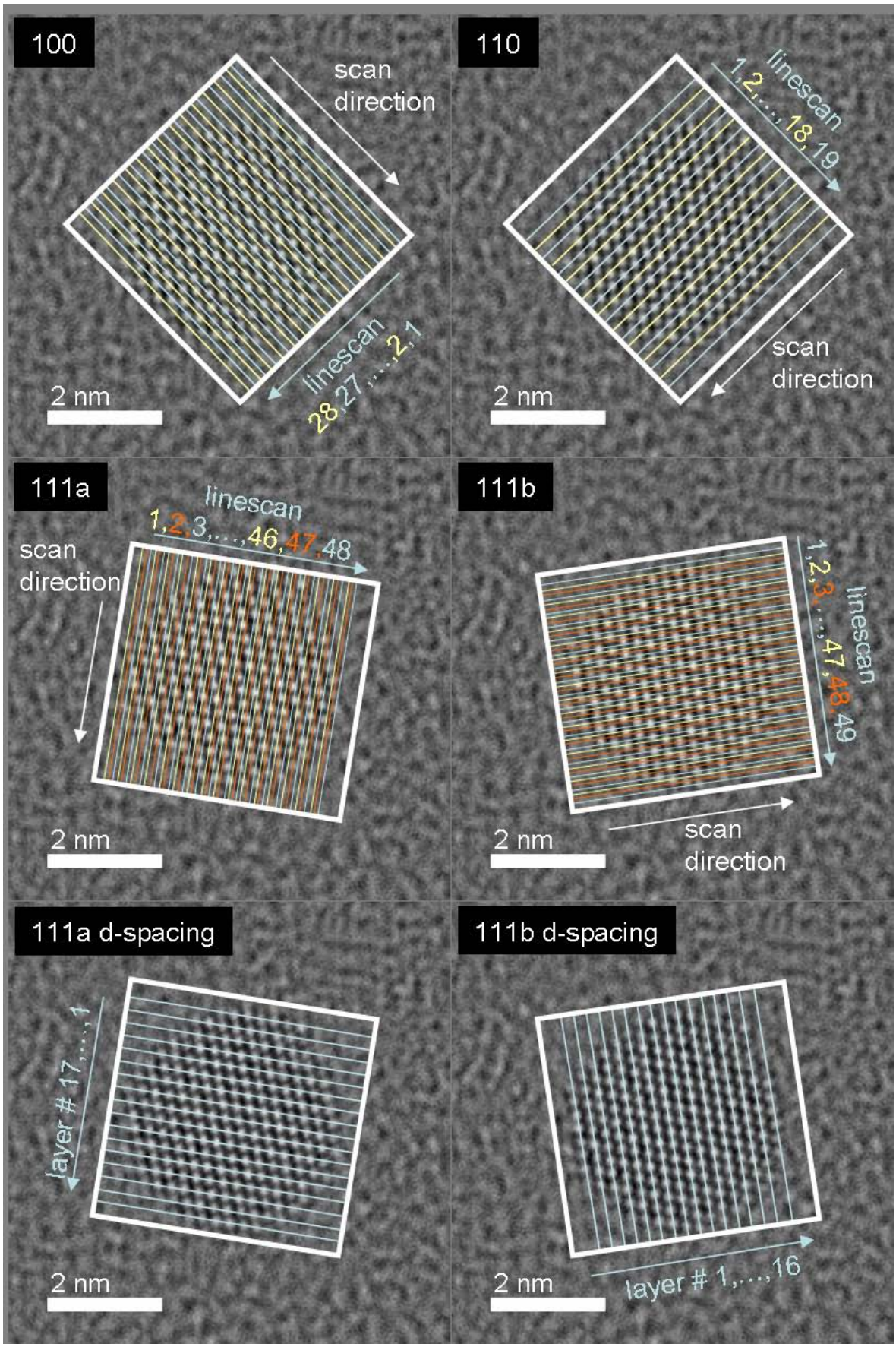


**Figure 4.30:** Indication of the facets of the series62-particle and of the linescan directions for the relaxation analysis.

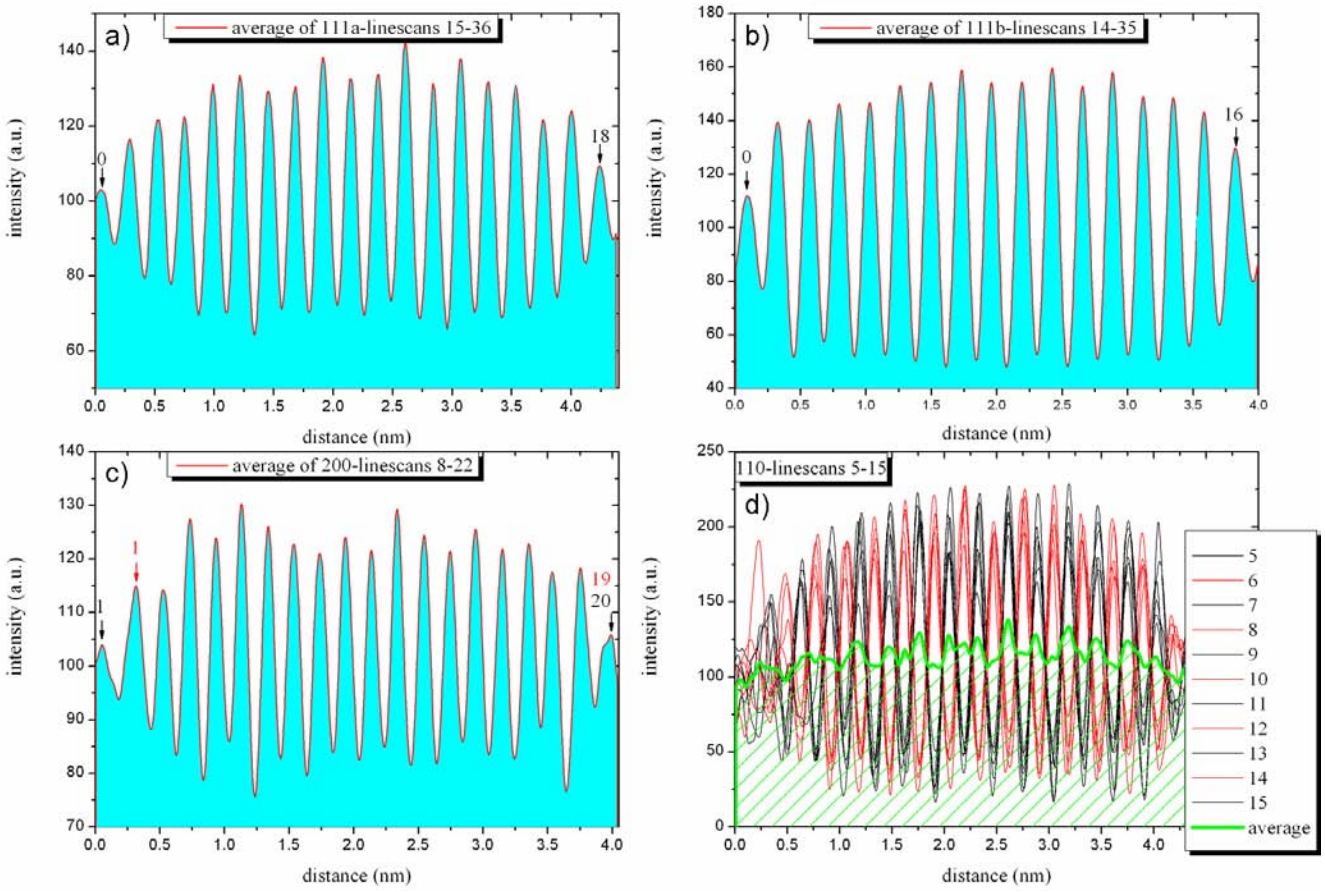


**Figure 4.31:** Viewgraph of the linescans taken in the four directions as indicated in fig. 4.30.

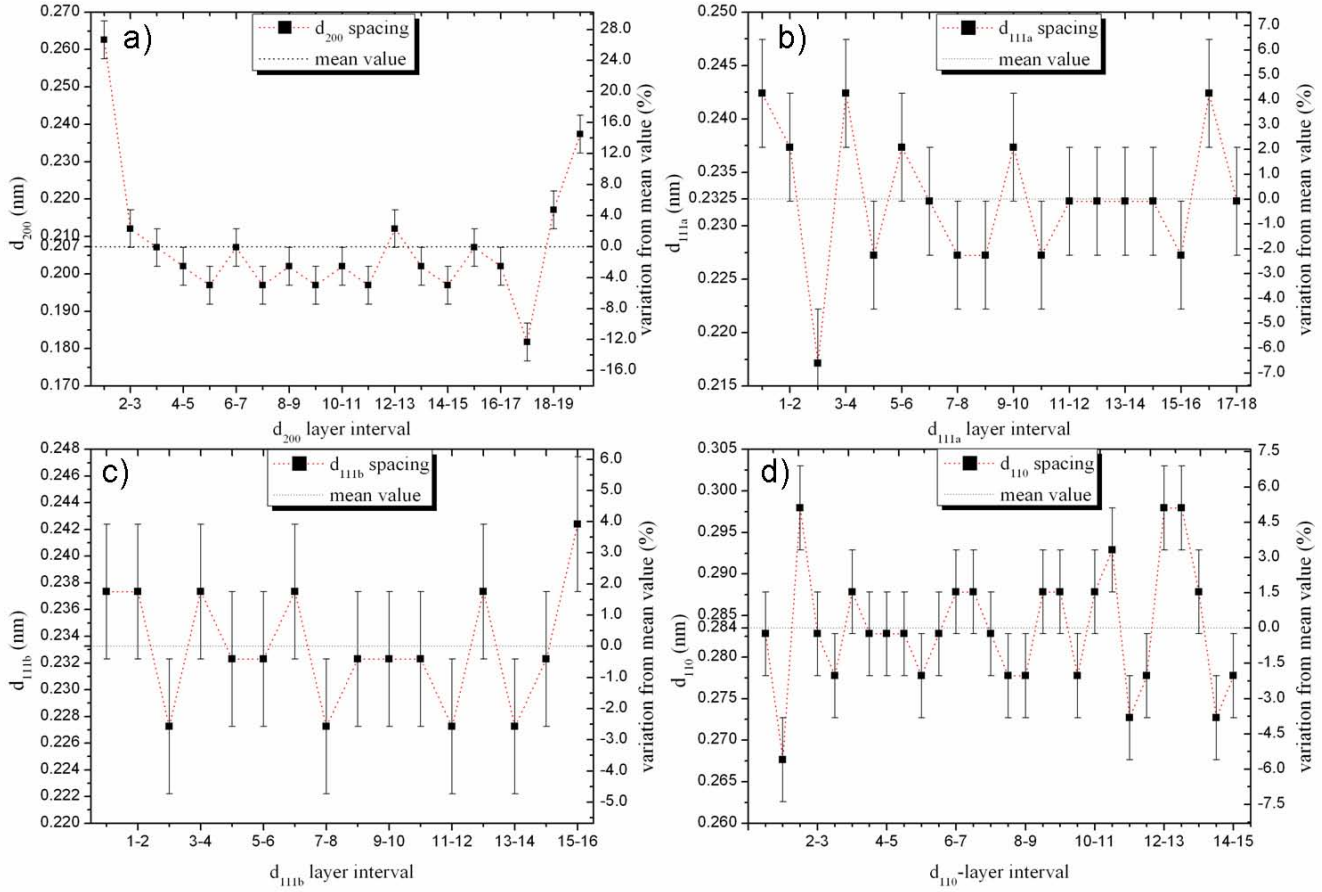


**Figure 4.32:** Layer resolved analysis of the four linescans as indicated in fig. 4.30. Here a) shows $d_{200}$ *spacing*, b) $d_{111a}$ *spacing*, c) $d_{111b}$ *spacing* and d) $d_{110}$ *spacing*.

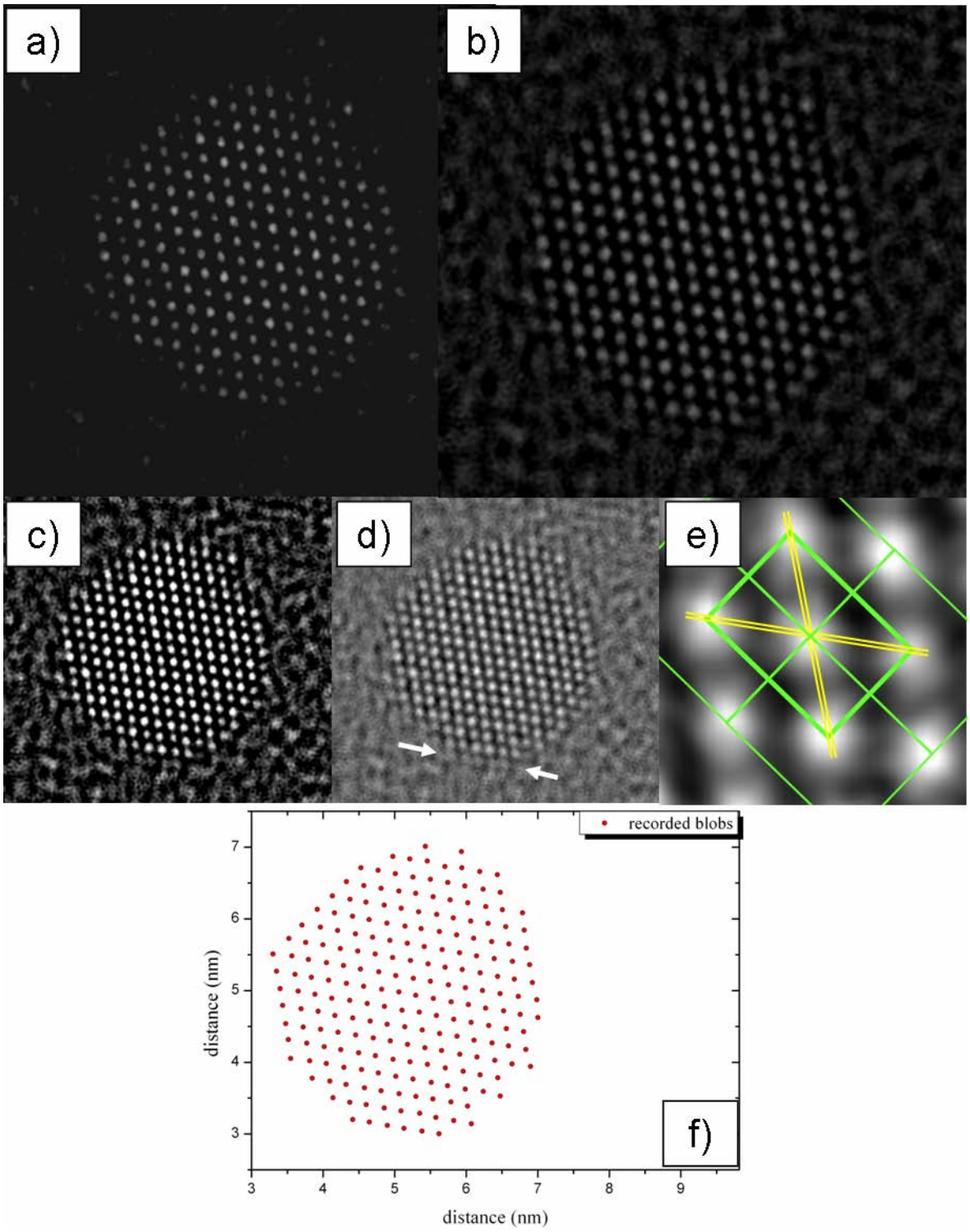


**Figure 4.33:** a)-c)Different contrast parameters for the reconstructed phase image, d) Phase image as resolved from exit wave reconstruction. The arrows mark an additional layer included in the 111a linescan not marked in fig. 4.30. e) Magnified cutout from d), the unit cells are pointed out, f) DERIP image of the series62 particle.

## 4.5 Simply Twinned Particles

It is very well known for gasphase particles that they have a tendency to be simply or multiply twinned for specific conditions (see fig. 6.1)[Dmi03]. Atomistic simulations suggest that multiply twinned structures are energetically favored for small metallic clusters [Mue05]. Experiments [Sta03c] on gasphase condensated FePt nanoparticles showed multiply twinned structures up to 5.9 nm diameter while larger particles of 7.6 nm prepared at higher gas pressures are single crystalline. For wet chemical synthesized FePt nanoparticles with surfaces modified by organic ligands the single crystallinity down to sizes smaller than 3 nm in diameter has been reported [Sta03a].
During my investigations I found colloidal as well as gasphase-prepared simply twinned particles. An example is shown in fig. 4.35. a) and b) show the colloidal particle and the corresponding FFT, c) and d) the gasphase condensated particle and the corresponding FFT.
Both particles were orientated in the [011]-direction and are twinned along a <111>-plane. This plane is marked by a (green) box, this box also marks the common [111]-direction. The arrows show the common <111>-layers (yellow) and the deviating [111]-directions (red).
Unfortunately the Exit Wave reconstruction was not possible for the colloidal particle and only two Scherzer images (particle 60*a and 61a) could be recorded (fig. 4.35 a)).
Fig. 4.34 shows the results. A tilt of that particle was observed under the electron beam: In a different Scherzer image of focal series60 , acquired approximately two minutes before the Scherzer image series*60, only the upper part of the particle shows lattice fringes, whereas the analyzed particle of series60*a shows 111-fringes all over the particle. The twin boundary was observed for the first time in the series61 Scherzer image (fig. 4.22, particle 61a). The diameter of this particle is approximately 2.5 nm, which is well below the "single crystal" limit reported in [Mue05]. As shown in fig. 4.34 the mean value for the lattice parameter for both Scherzer images is 0.3961nm ± 1%. The lattice parameter of series61 is increased by 1.4% with respect to the one of series60*. Both values however are within the error bars. Nevertheless this increase for successive focal series should be regarded more closely, since a time dependent structural relaxation under the e-beam may be at its origin.

The FFT analysis was also performed separately for the top and the bottom part of the particle. Both lattice parameters deviate only by 0.5%.
The mean value of the lattice parameters resolved of other particles in the MO10 sample are within 0.4% identical to the mean value determined here.

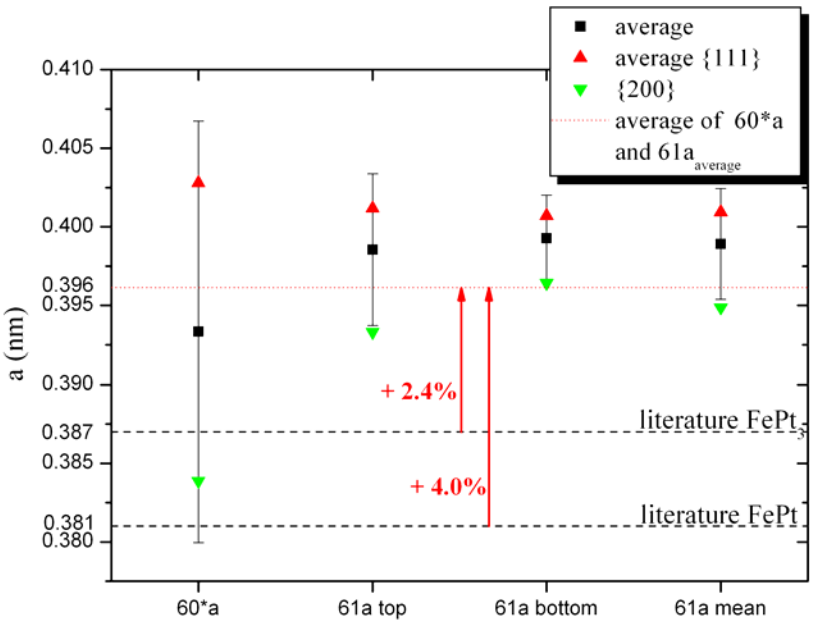


**Figure 4.34:** . Lattice parameter for a simply twinned colloidal particle (series61) resolved from directional FFT analysis. The error bar represents the standard deviation.

In fig. 4.14 the mean lattice parameter of the twinned particle prepared by gasphase synthesis is shown (series16). The diameter of this particle is approximately 7 nm and the simply twinned structure it is in good accordance to the experimental results mentioned in [Mue05]. Fig. 4.36 shows that the particle facets are not very well defined. No surface layer is complete, single atom columns are distributed at the surface facets. It seems that the bottom <111>-layer interval has a larger $d_{111}$-layer spacing than the <111>-layers inside the particle. Due to the small phase signal of this surface layer, its relaxation could be rather attributed to the presence of oxygen than to a Pt-segregation.
One also notices that the atom columns are not perfectly aligned. This misalignment at the ends of the layers is also observed for the top <111>-layers.
The displacement of the atom columns is most likely connected to sintering processes (see fig.6.7). In this figure three successive EWR phase images are presented. Unfortunately, the orientation of the particles was not stable during the acquisition of three focal series. The comparison of series16 and series17, however, reveals a changed boundary structure. Even the bending of layers can be observed.

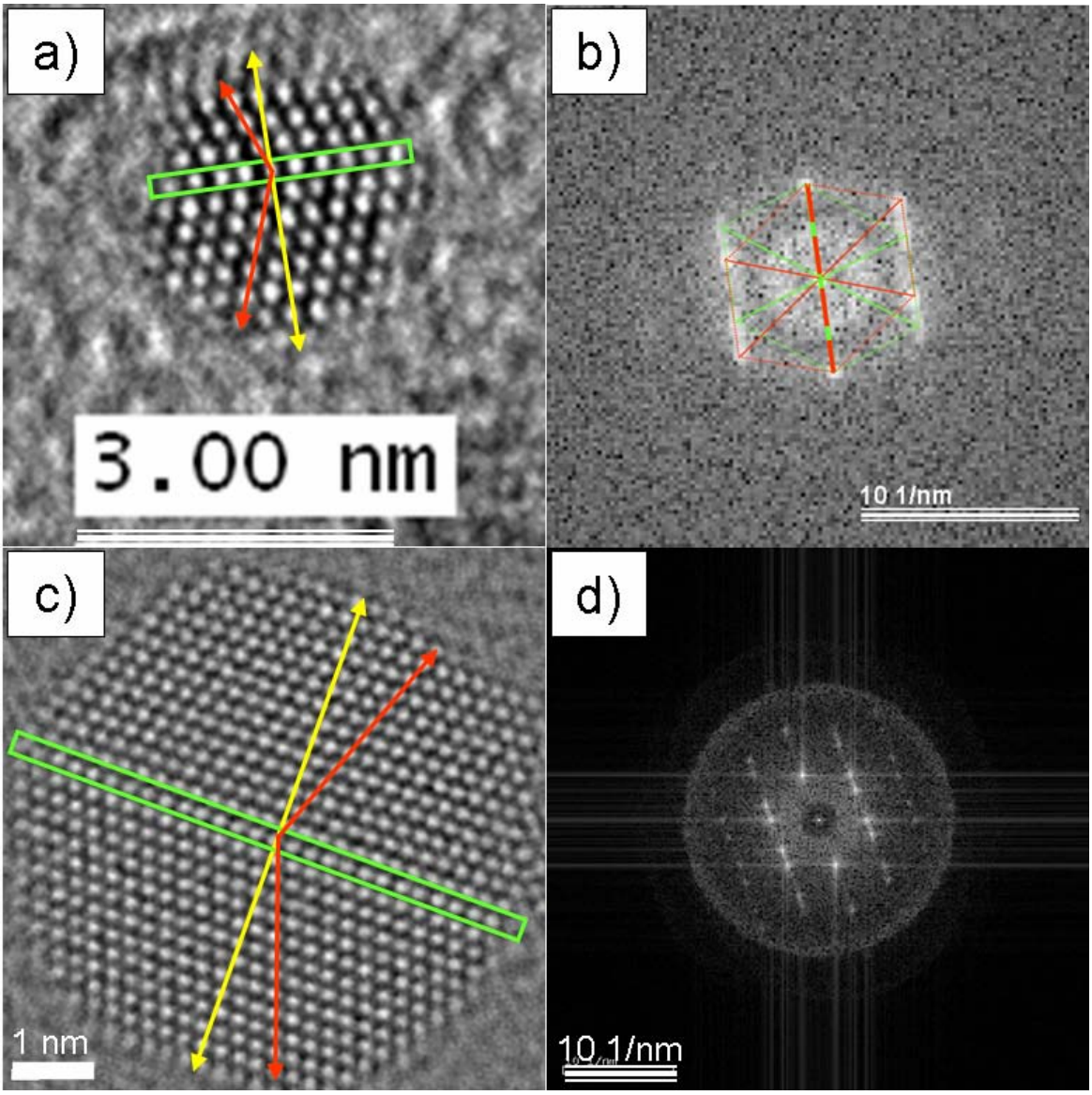


**Figure 4.35:** Two twinned particles in [011]-zone axis. a) colloidal particle (series61) b) FFT of series61 particle c) gasphase particle (series16) d) FFT of series16 particle

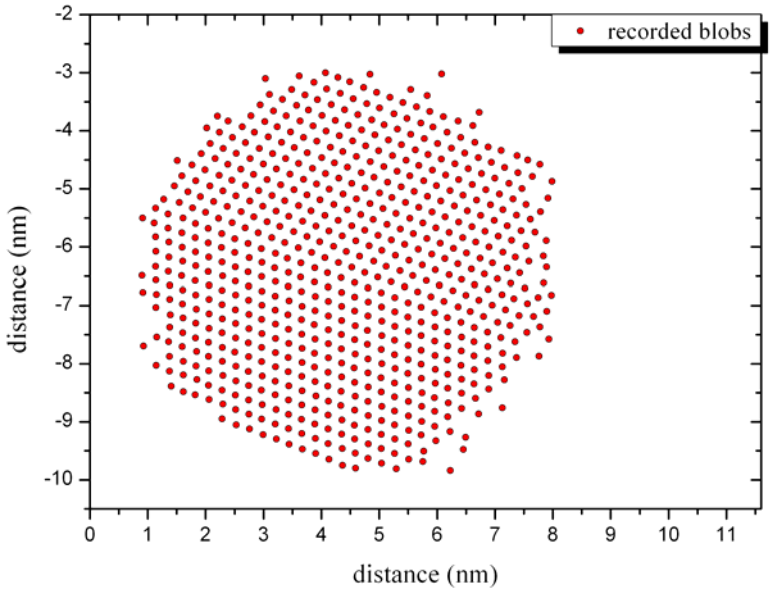


**Figure 4.36:** Scaled "blobs image" of the Series16 gasphase particle, which is also shown in the Derip acquisition scheme, see fig. 4.4.

# Chapter 5

# Conclusion

The aim of this thesis was to analyze gasphase and wet chemical prepared $Fe_xPt_{1-x}$ nanoparticles (NPs) with respect to the influence of composition gradients and shell-wise layered structures on the lattice parameter. High Resolution Transmission Electron Microscopy (HR-TEM) was used for the analysis. Traditional HR-TEM images (lattice images) were interpreted by visual inspections. Further improvements included the development of indirect methods and a quantitative comparison of simulated images with experiments. Recently it became possible to recover the full phase and amplitude information of the electron wave exiting the sample (Exit Wave Reconstruction (EWR)) by recording a focal series of HR-TEM images. With this technique the shape and the separation of lattice planes could investigated with sub-Angstrom resolution and without disturbing delocalization effects. To determine the mean lattice parameter of the NPs three different analysis methods were used and compared to each other. Within the error bars every method revealed the same result. As a result of this detailed analysis the lattice structure in different crystallographic directions is presented for one gasphase (fig. 4.18) and one colloidal (fig. 4.32) NP. It is demonstrated that apparently unphysical results can be removed by an even more refined analysis and that in focal series tilts or movements of the particle which are not visible in the FFT may produce such artifacts.
From my analysis no evidence for a surface layer relaxation in general was found. The layer spacing rather shows small oscillations within the error bar around the mean lattice parameter of the core. In future investigations more detailed statistic analysis of the surface relaxation may have to be done, to clarify the existence of a surface relaxation in FePt nanoparticles. One should note, however, that my detailed investigations revealed that no particle is like the other.
A general lattice expansion of up to 4% compared to the bulk was determined. The origin

of this expansion could not be identified. The presence of oxygen may play a role. On the other hand the lattice expansion in the NPs may be driven by surface effects. Due to the limitation of the nanoparticle there might be a "surface relaxation" as observed in metallic bulk systems throughout the particle. To investigate this in more detail, the three dimensional shape and the atomic composition of the NPs must be known. In conclusion the combination of quantitative HR-TEM using the Z-dependence of the phase signal, EWR and tomography, as discussed in this thesis is a promising method to fully reveal the structure of NPs.

# Chapter 6

# Appendix

## A-1 Microscope Parameters

**Table 6.1:** specific microscope parameters

| microscope | CM300 | TecnaiF20 ST |
|---|---|---|
| voltage (kV) | 300 | 200 |
| electron wavelength (pm) | 1.97 | 2.51 |
| $C_S$ (mm) | 0.6 | 1.2 |
| semiconvergence angle $\alpha$ (mrad) | 0.2 | 0.1 |
| defocus spread (nm) | 1.5 | 10 |
| information limit (nm) | 0.08 | 0.15 |
| sampling rate (Å/pixel) | 0.202 | 0.216 |

## A-2 Structural Data for FePt

**Calculation of $d_{hkl}$ for fcc and fct structures**

fcc:

$$d_{hkl} = \frac{a}{\sqrt{h^2 + k^2 + l^2}} \tag{6.1}$$

fct:

$$1/d_{hkl} = \sqrt{\frac{h^2 + k^2}{a^2} + \frac{l^2}{c^2}} \tag{6.2}$$

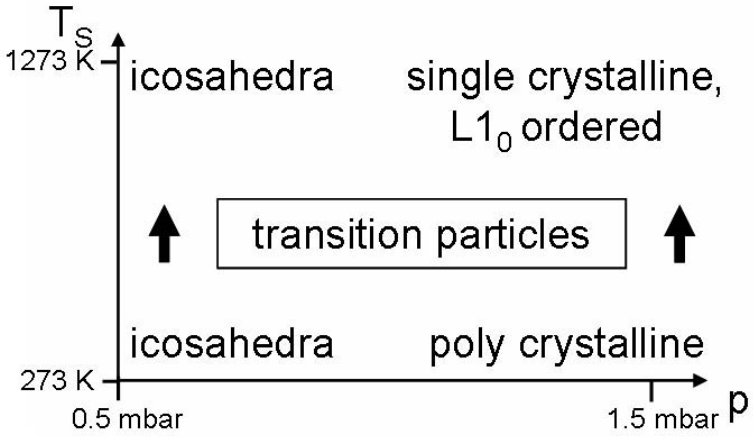


**Figure 6.1:** This sketch shows that the structure of the gasphase condensated particles is dependent on two parameters: the sinter temperature $T_S$ (273 K $< T_S <$ 1273 K ) and the basic pressure p (0.5 mbar $<$ p $<$ 1.5 mbar)[Dmi03].

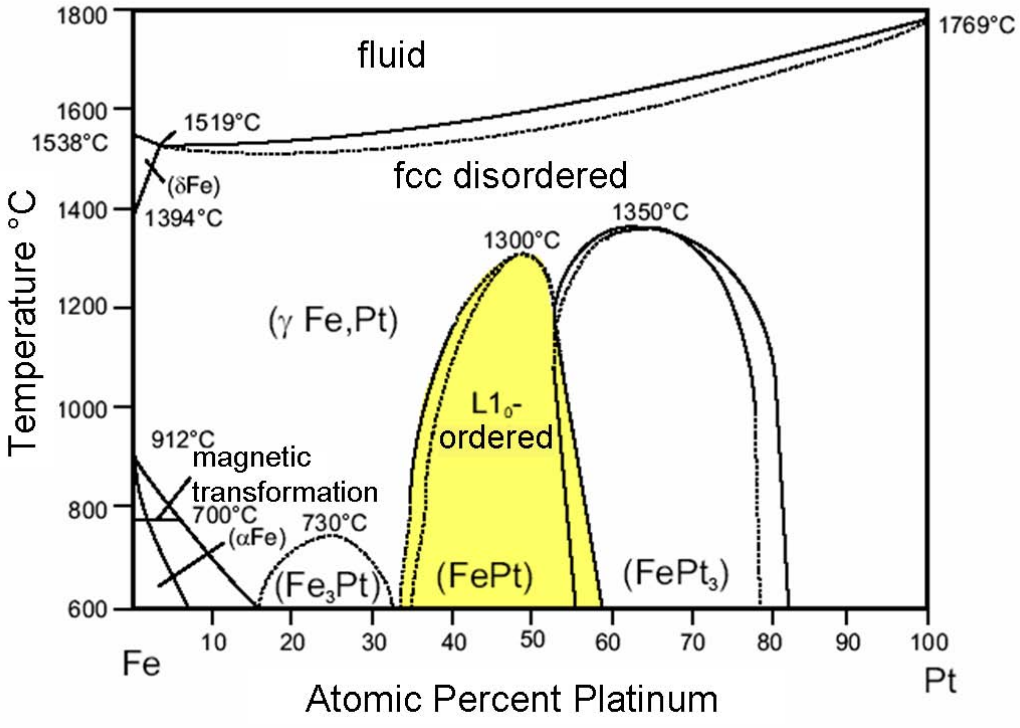


**Figure 6.2:** Binary phase diagram of $Fe_xPt_{1-x}$ alloys for T $\geq$ 873 K [Wha98, Rel95, Sta03b].

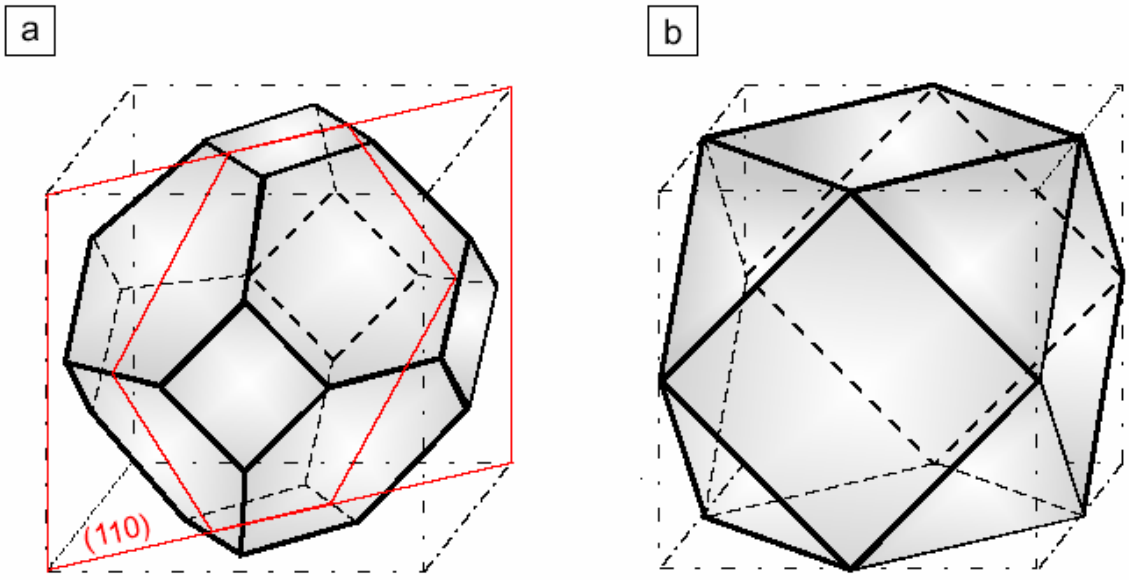


**Figure 6.3:** Sketch of a truncated octahedron (a) and of a cuboctahedron (b) (adapted from [Sta03b]. In (a) a cut along a <110>-layer is displayed by red lines. NP are often observed to be orientated along a [110]-zone axis, i.e. [111]-facets and [100]-facets are found at the edges. The NPs also tend to have [110]-facets due to the missing of the edge atom columns between two [111]-facets.

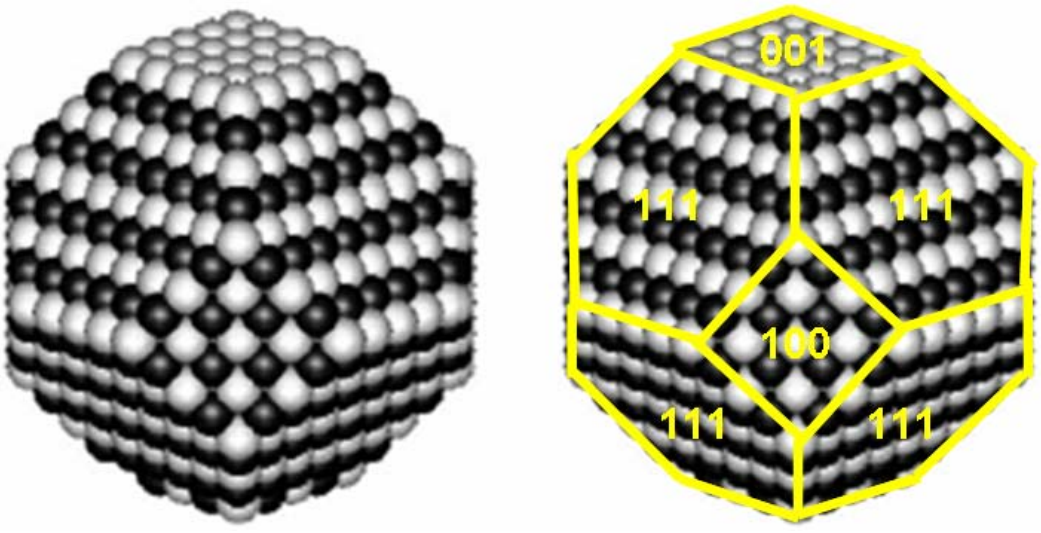


**Figure 6.4:** Indication of facets for a truncated octahedric particle.

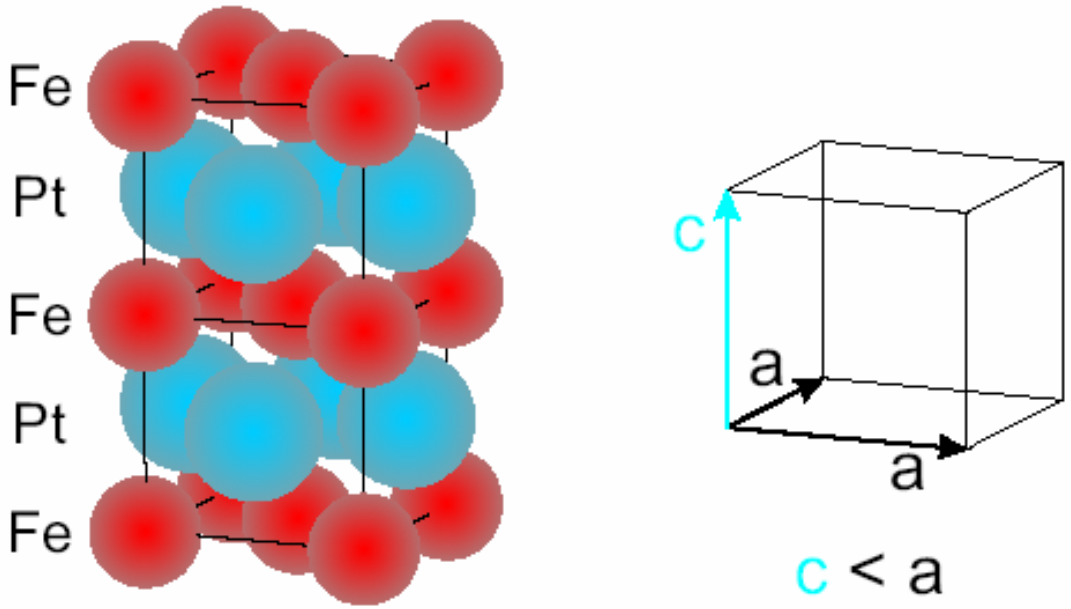


**Figure 6.5:** Schematic view of the $L1_0$-structure. Fe- and Pt- atom layers alternate along the [001]-direction. The structure is tetragonal distorted (c < a due to the different atom radii of Fe and Pt). Adapted from [Sta03b].

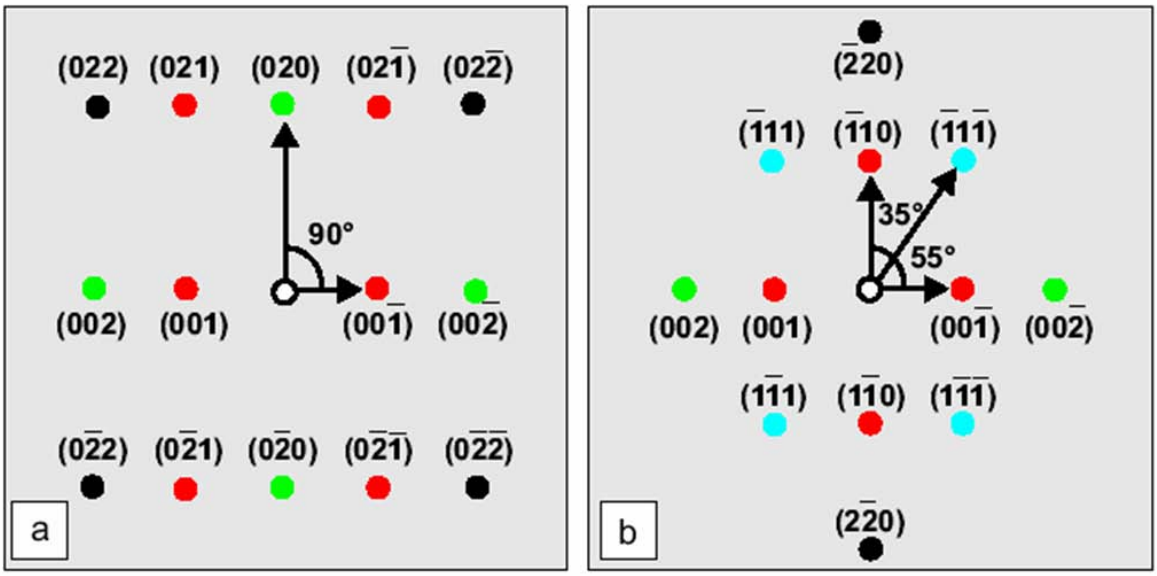


**Figure 6.6:** Diffraction pattern for fcc single crystalline structures along the [100]-zone axis (a) and along the [110]-zone axis (b). The reflections are marked by different colors for different directions. The red marked reflections are only visible in the $L1_0$-structure and are forbidden for the disordered fcc structure. Adapted from [Sta03b].

| fcc ($a = 0.381\ nm$) | | | | fct ($a = 0.385\ nm, c = 0.371\ nm$) | | | |
|---|---|---|---|---|---|---|---|
| h | k | l | $d_{hkl}$ (nm) | h | k | l | $d_{hkl}$ (nm) |
| 1 | 0 | 0 | - | 1 | 0 | 0 | 0.3850 |
| 0 | 1 | 0 | - | 0 | 1 | 0 | 0.3850 |
| 0 | 0 | 1 | - | 0 | 0 | 1 | 0.3710 |
| 1 | 1 | 0 | - | 1 | 1 | 0 | 0.2722 |
| 1 | 0 | 1 | - | 1 | 0 | 1 | 0.2671 |
| 0 | 1 | 1 | - | 0 | 1 | 1 | 0.2671 |
| 1 | 1 | 1 | 0.2200 | 1 | 1 | 1 | 0.2195 |
| 2 | 0 | 0 | 0.1905 | 2 | 0 | 0 | 0.1925 |
| 0 | 2 | 0 | 0.1905 | 0 | 2 | 0 | 0.1925 |
| 0 | 0 | 2 | 0.1905 | 0 | 0 | 2 | 0.1855 |
| 2 | 1 | 0 | - | 2 | 1 | 0 | 0.1722 |
| 1 | 0 | 2 | - | 1 | 0 | 2 | 0.1671 |
| 0 | 1 | 2 | - | 0 | 1 | 2 | 0.1671 |
| 2 | 0 | 1 | - | 2 | 0 | 1 | 0.1710 |
| 1 | 2 | 0 | - | 1 | 2 | 0 | 0.1722 |
| 0 | 2 | 1 | - | 0 | 2 | 1 | 0.1710 |
| 2 | 2 | 0 | 0.1347 | 2 | 2 | 0 | 0.1361 |
| 2 | 0 | 2 | 0.1347 | 2 | 0 | 2 | 0.1336 |
| 0 | 2 | 2 | 0.1347 | 0 | 2 | 2 | 0.1336 |

**Table 6.2:** Calculated $d_{hkl}$-layer spacing of the allowed miller indices for stoichiometric FePt bulk (fcc and fct structure) [Lan92].

## A-3 Sintering

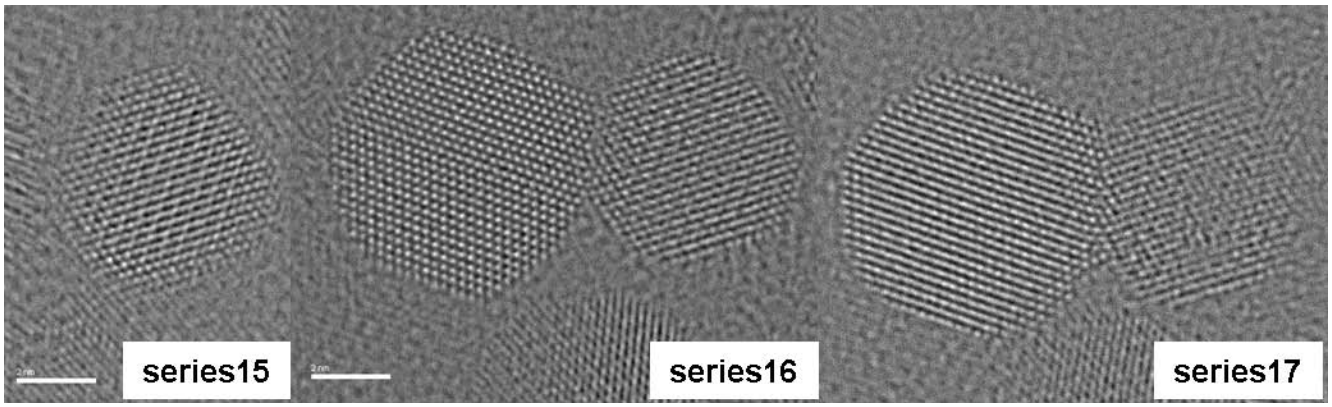


**Figure 6.7:** Three exit wave reconstructed phase images of three successive focal series showing the same NPs. The time frame for the acquisition of the three series is approximately 8 minutes. In series15 only the right of the two nanoparticles clearly visible in the other two series is shown. Sintering of the nanoparticles can be observed.

# A-4 Analysis by FFT of Linescans

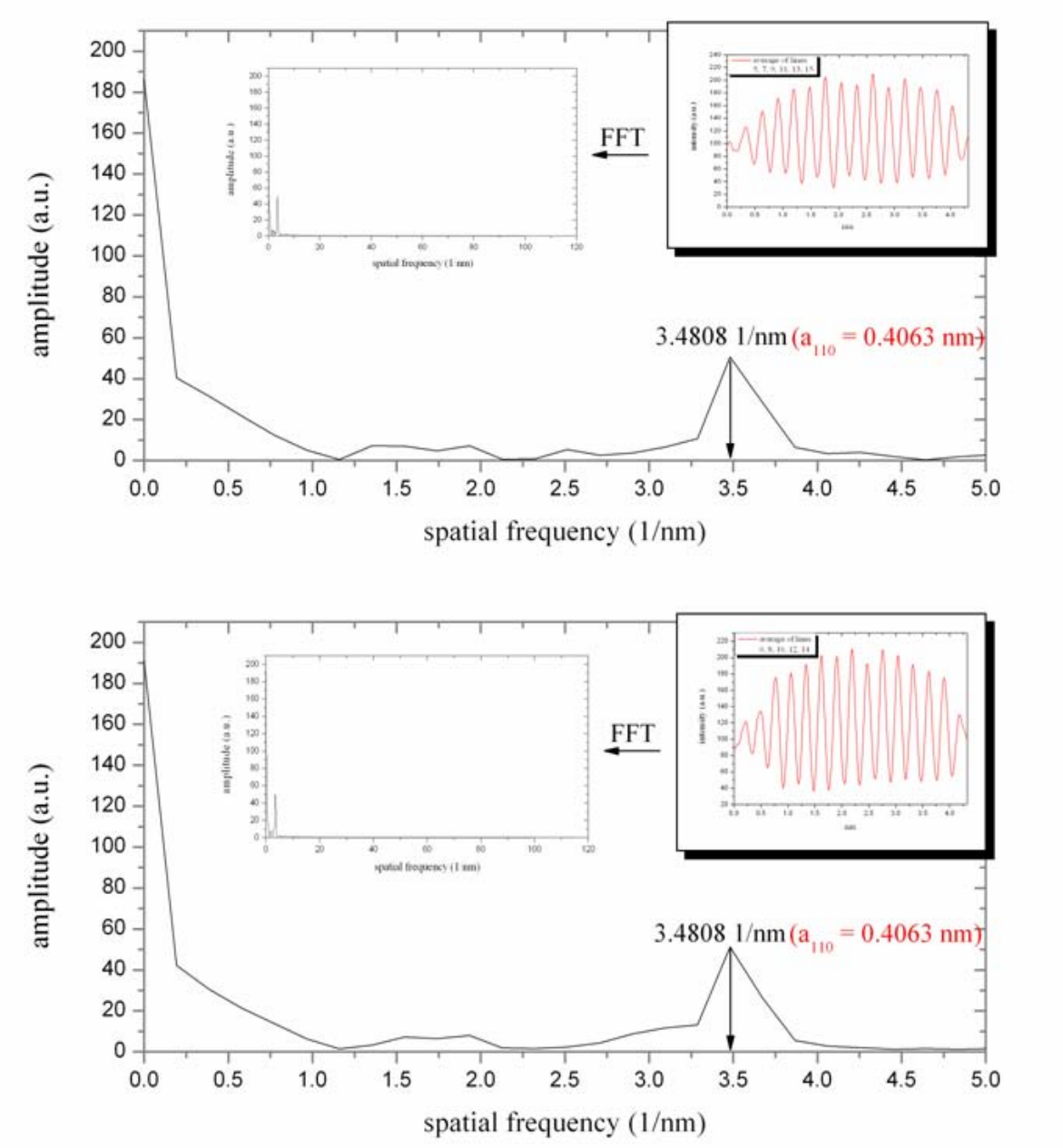


**Figure 6.8:** FFT analysis for two different averaged linescans for the identic scandirection.

# A-5 EWR Using TrueImage

The TrueImage software is continously improved. The general information given here is typical for all software versions. At NCEM I used version 2.4.4. It is always helpful to have a look in the corresponding manual, too.

## A-5.1 Focal-series acquisition at the TEM

Before starting for a focal series acquisition the microscope has to be carefully aligned to the optimum. That means gun tilt and gun shift routines have to be done, the sample has to be set to the eucentric height, condenser and objective astigmatism has to be corrected as well as the 2-fold-astigmatism and coma (if possible). Also the pivot points have to be checked. Since those procedures are slightly different for each microscope no more detailed information will be given in this context. There is always some help-menu in the software of the microscopes where all steps can be looked up. The CM300 microscope at NCEM also has some special software as an additional script in the DigitalMicrograph programm for correcting astigmatism and coma more easily.

## A-5.2 EWR with TrueImage

In Figure 6.9 the control panel of the the TrueImage version used @NCEM is shown. On the right side the images will be loaded and shown. On the left side are the parameter settings, the correction and the output options. They are described in a little more detail in the according sections.

### Renaming the file extension

The first thing to do before enabling the TrueImage options is to change the file extension to ".dm2" of the uploaded focal series. Note that the image acquisition computer is a Macintosh which does not export file extensions. Another reason is, that @ the CM300 microscope not the TrueImage acquisition software is used, but also a script for DigitalMicrograph which exports the recorded images as ".dm2" files. Since TrueImage is a software working on a "Windows"-system this annoying step has to be done. The easiest way to do this is to use the "DOS-shell". There it's possible to change the file extensions of whole folders. Only a few short instructions are necessary:

1. open "command prompt": start → programs → accessories → command prompt

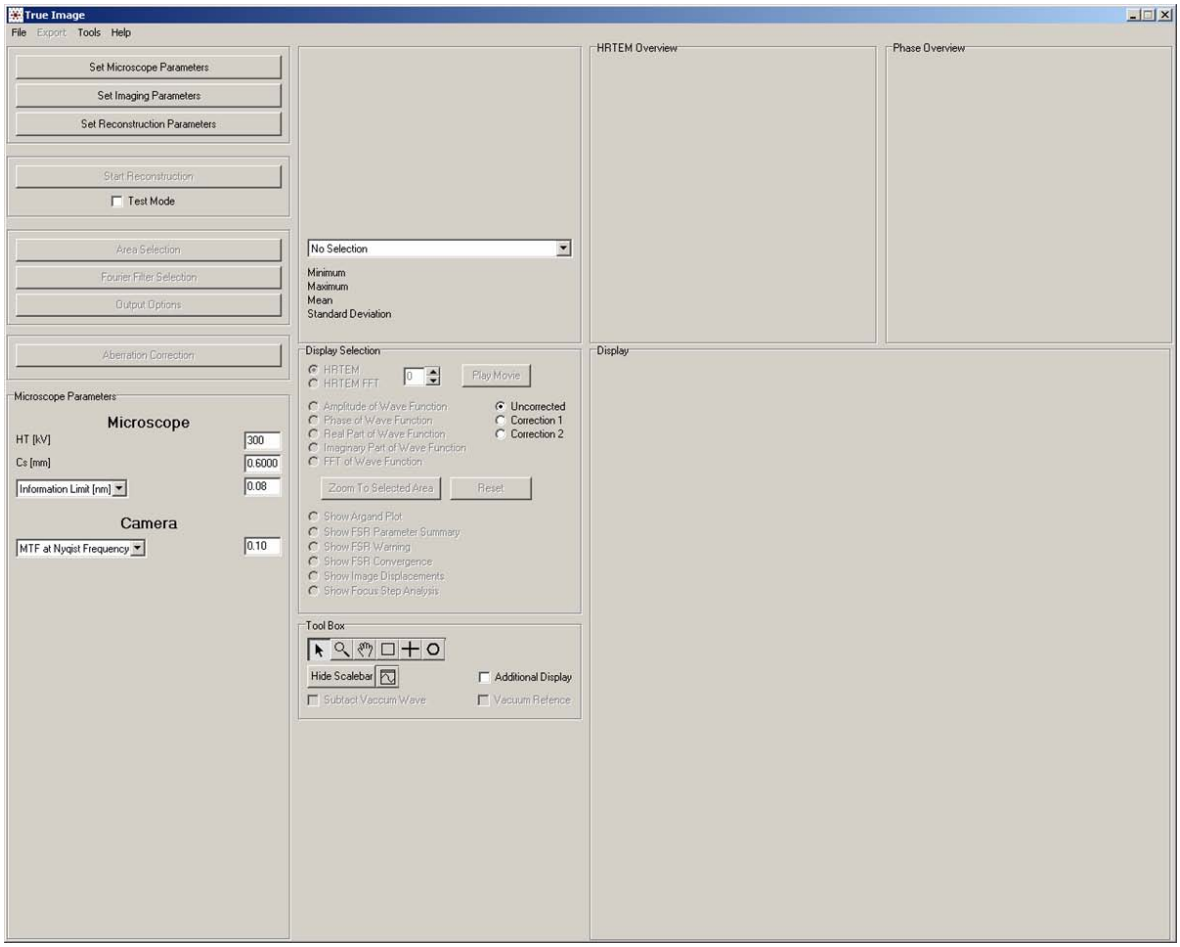


**Figure 6.9:** TrueImage control panel for version 2.4.4 as it is displayed when TrueImage is opened.

(in the German Windows version: Start → Programme → Zubehör → Eingabeaufforderung accordingly)

2. choose the partition of your hard disc where the folders with the focal series images are stored, typically "C:" or "D:" by entering *C:* (*D:*), then press "return"

3. change directory to the folder address: *cd␣"C:* $\cdots$.foldername*"* press "return"

4. now you are in that folder: enter: *rename *.*␣*.dm2* press return

5. if more folders have to be changed the ↑-button can be used, then former commands are shown by simply pressing it several times; another possible command is: *cd␣..* which allows for going to one directory above.

**remark:**␣ means blank

### Convert data

**Important:** The files have to be numbered sequently starting with 001.*extension*. TrueImage needs data in Raw- or in Tietz-Format which means .dat extension of the files. So the images in dm2-format have to be converted. This can be done with the "Convert Digital Micrograph Files"-button which appears when the "tools"-option is selected as shown in figure 6.10. As soon as this option is checked another window will open. Here the folder of the focal series is to be selected first, then the first picture with extension "...001.*dm*2" which will appear in this window has to be marked and then the form *"variable header .dat"* has to be chosen. Once the focal series is converted into the *.dat-format* it can be loaded into TrueImage under "File". Load the focal series. See Figure 6.11. As before also the first image of that series has to be selected. Now, the first image of the focal series will be opened in the Display-area. The up/down-arrows can be clicked to display the next or previous image of the serious. *"Play Movie"* allows continuous displaying.

### Setting center of reconstruction area

Having all images of the focal series checked the center of the reconstruction area has to be defined. This is done by clicking in the center of the image in an older version of TrueImage, in the version used at Berkeley *"Select Area"* had to be used. In this version the advantage is that you can see this selected area also by changing the image numbers. So it is possible to make sure that your area of interest stays in the frame. Make sure that the frame is not set too close to the edge of the image. Due to the *point-spread-function*

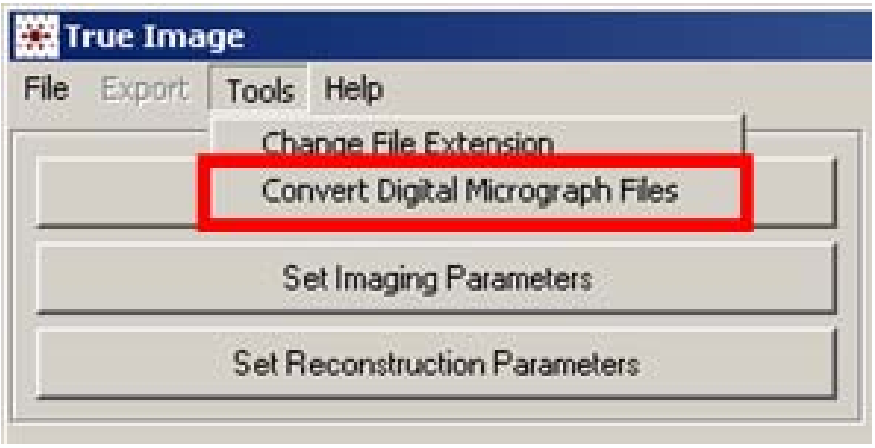


**Figure 6.10:** *"tools"*-options in TrueImage: changing of file extensions and converting of Digital Micrograph (.dm-files) into .dat-files is possible.

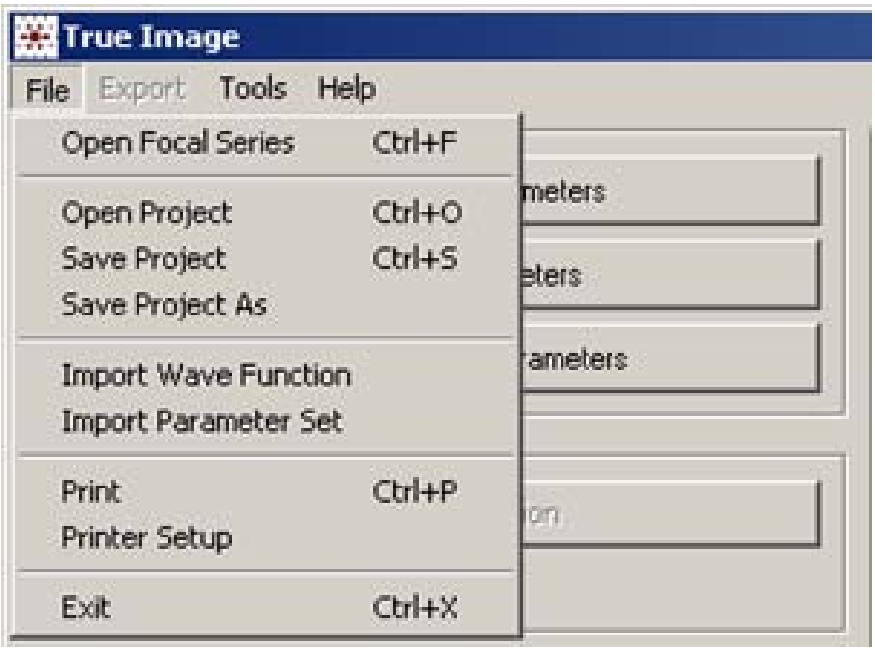


**Figure 6.11:** *"files"*-options in TrueImage: Loading of a focal series, opening/saving of projects and import of wave functions and parameter sets is possible.

(chapter 2.1.3) the information is not complete in the border area of an image and this leads to errors in the reconstruction. If the object drift is too strong, so that the structure moved out of the field of view during the focal series acquisition only a reduced number of images can be used for the reconstruction, however there have to be at least *ten images* for TrueImage to work.

### Scaling of the gray levels

Once the series is loaded, check *"Histogram - Full Area"*(see fig. 6.12) to get the histogram of the displayed image. Two red lines indicate the minimum and maximum of the gray levels used for the display. By click and drag (left mouse button) the display minimum and maximum can be individually redefined as indicated with the two blue arrows in fig. 6.12. This redefinition will set all images of the focal series to the same normalized minimum and maximum.

### Microscope Parameters

Press *"Set Microscope Parameters"* so that the Microscope Parameter window opens and edit it for the relevant microscope. In fig. 6.9 this window is opened (left side) with parameters for the CM300 microscope. The parameters to edit are:

**HT:** High Tension of the microscope in kV

**$C_s$:** Spherical Aberration of the objective lens of the microscope in mm

**Focus Spread/Information Limit:** Usual edit is the information limit which is determined by the High Tension and the focus spread of the microscope. The focus spread value corresponds to one half of the $(1/e)$-width of a Gaussian distribution of foci [Küb03].

**MTF:** Modulation Transfer Function of the CCD, has to be 1 for simulations.

### Imaging Parameters

Press *"Set Imaging Parameters"* so that the Imaging Parameter window opens. In fig. 6.13 left side this window is shown for the CM300 parameters.

**Sampling:** pixelsize in nanometers. It has to be rechecked regularly since the camera magnification has to be very accurate.

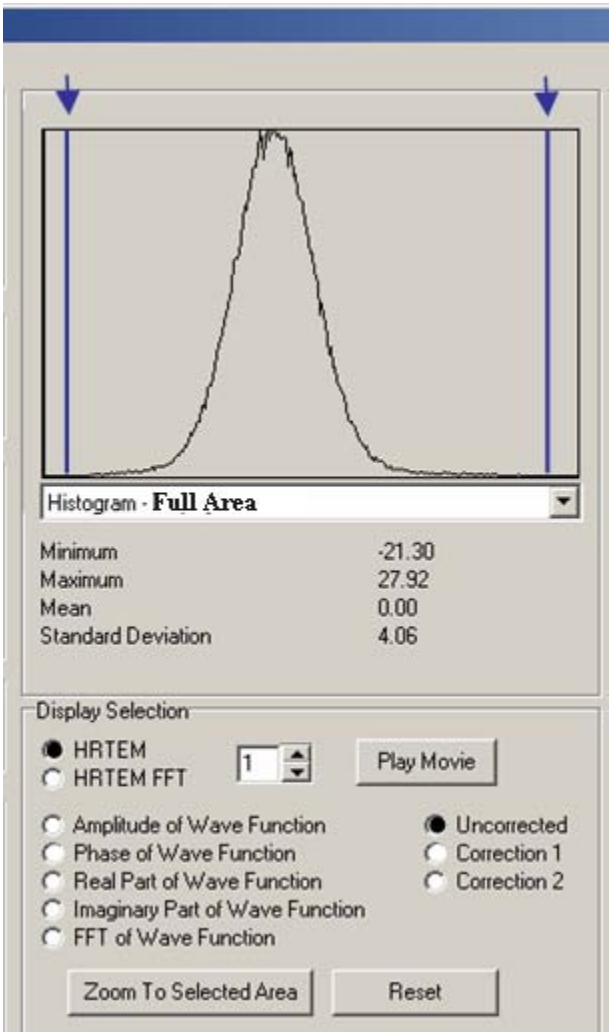


**Figure 6.12:** Area of the TrueImage control panel in which the scaling of the gray levels for all images of a series can be done. "*Play Movie*" allows for playing back all images continuously.

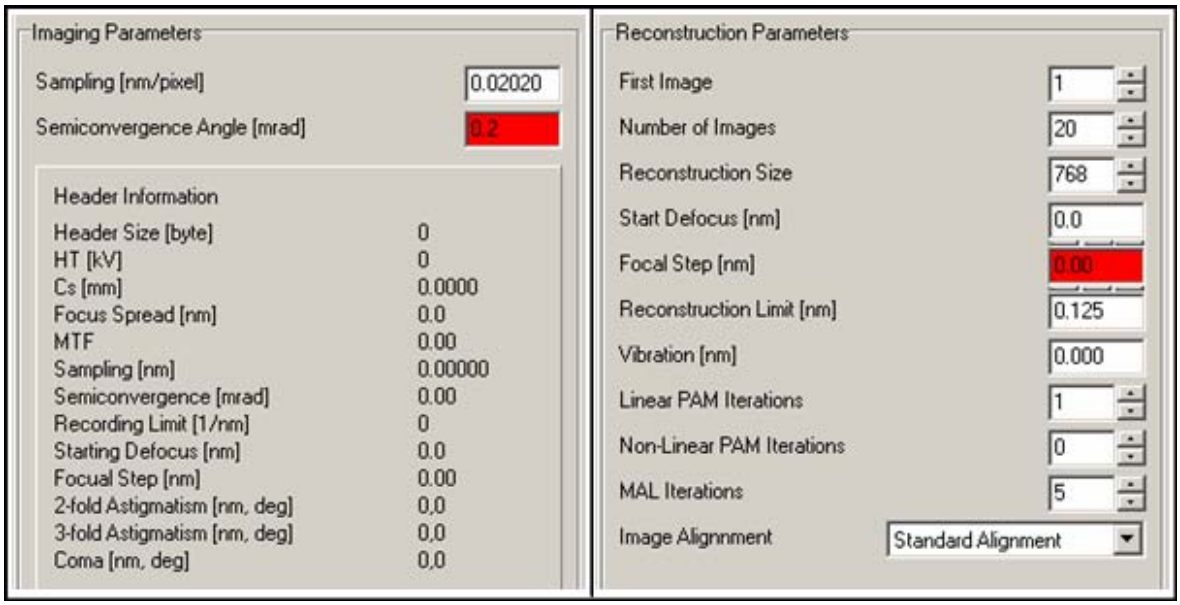


**Figure 6.13:** Parameter setting windows in TrueImage. See section A-5.2 (below) for a detailed description of the single parameters.

**Semi-Convergence Angle:** illumination convergence angle measured in mrad. As the value for the defocus spread it also corresponds to to one half of the $(1/e)$-width of a Gaussian distribution of incident angles.

### Reconstruction Parameters

Press *"Set Reconstruction Parameters"* to display the window for the Reconstruction Parameters.

**First Image:** First image to be used for the reconstruction. The highest image number is 11 since there have to be at least 10 images.

**Number of images:** Number of images used for the reconstruction. From 10-20.

**Reconstruction Size:** Size of the reconstruction area. The typical frame size for the reconstruction is $768pixel \times 768pixel$.

**Start Defocus:** The estimated defocus-value for the first image used in the reconstruction. Mind that underfocus values are negative.

**Focal Step:** Focal distance between to images. Negative value: Series taken towards increasing underfocus. Reasonable estimation of the focal step enables for faster,

better reconstruction results. See below for how to estimate the defocus values and the focal step size.

**Reconstruction Limit:** sets the limit for the reconstruction calculation. Should be equal to the information limit of the microscope. A slightly larger value is also possible.

**Vibration:** Vibration amplitude (one half of the $(1/e)$-width) for mechanical or electrical vibration in nm. Vibrations are considered to be isotropic but normally the value is set to zero. (No mechanical vibrations)

**Linear PAM Iterations:** Maximum number of pure PAM-iterations (see 2.2.2. Usually it is only used for faster convergence and is set to 2 at most.

**Non-Linear PAM Iterations:** Number of non-linear PAM-iterations. Usually 0.

**MAL Iterations:** Number of Mal-iterations also taking non-linear contributions fully into account. See 2.2.2 for more information on the MAL-method. Typically are 4iterations, but increasing the number up to 10 iterations is mostly more sufficient.

**Image Alignment:** Usually set to standard alignment for, here a cross-correlation between the images is initialized to compensate drift. For simulation data *"no image alignment"* has to be selected.

### Finding the right defocus values

Finding the defocus values is done with another program: MacTempas which unfortunately only works on Macs. There exists *"Focus Determination"* in the *"Process"*-menu in which can be chosen between the general parameter setting *"Find Focus Search Parameters"* (see fig. 6.14) and *"Find Focus From Image"* (see fig. 6.15). So it is reasonable to set the parameters first. The CM300-parameters are given in tab. 6.1. Also the inner peak should be excluded for the fitting procedure and maximum use of 3 peaks works well. Mind that the full defocus range of the series is be taken into account in the interval of smallest defocus and largest defocus, better determine this interval broad-minded. So for the focal series taken around CM300's Lichte-defocus which is approximately $-2700\mathring{A}$ the interval given in fig. 6.14 is unusable. More specifications can be done in *"Peak Finding Criteria"*.

As soon as all parameters have been set and the image whose defocus has to be estimated is opened, "*Find Focus Search Parameters*" has to be selected and a window as shown in fig. 6.15 appears. The "*Make CTF follow ring markers*"-box has to be checked then the calculated CTF due to the input parameters has to be fitted to the peak. The more

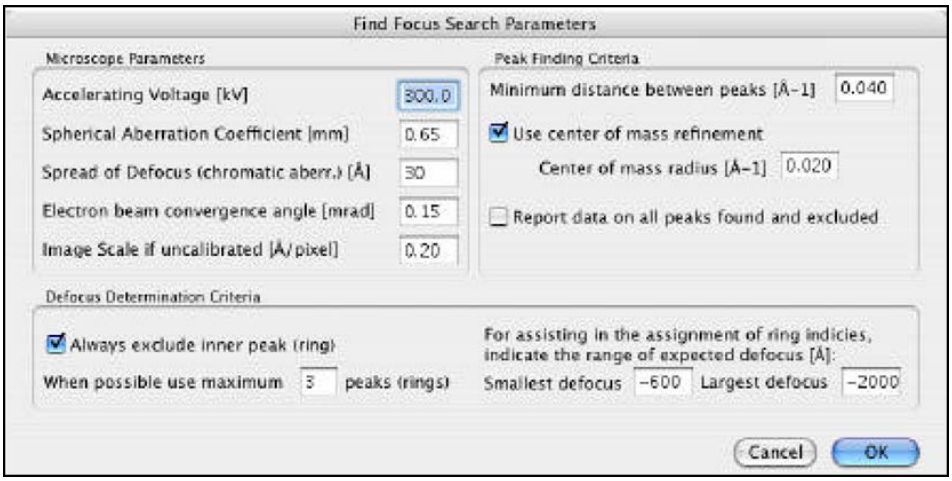


**Figure 6.14:** Window for setting the parameters defocus values in MacTempas. Here the parameters for the defocus-fitting can be set, so that they will be transferred to every focus-finding-process.

accordance between the both the more precise is the estimated defocus value. Look for the minima to optimize accordance. It is important not to weight the first maximum to strong, better go for the next ones. The calculated CTF (red-colored graph in figure) can be shifted by clicking and holding one of the numbered red lines that indicate the maxima. The defocus value is shown in the middle of that window.

### Focal-Step-Size Analysis

If the defocus determination is done for every image in a focal series a plot can be made $\Delta f(\textit{image no.})$. The slope of the linear fit is the focal-step-size. These plots enable also to see the images whose defocus values differ too far from the fit and might be unusable for the reconstruction. Depending of the quality of the focal series images a smaller amount of images leads to a better result concerning the focal-step-size.

### Check Input Parameters + Start Reconstruction

There are different checking options as to check the CTF referring to your input parameters. Therefore *"Show CTF"* has to be checked. In this CTF window another option can be checked: *"FFT"* to display a rotationally averaged line profile of the FFT. *"FFT-Peak"* allows for displaying the maximum intensity of the FFT for each radius. But the most important thing to check is your general parameters. To do this, *"Test Mode"* under *"Start Reconstruction"* has to be checked and *"Check Parameters"* has to be activated.

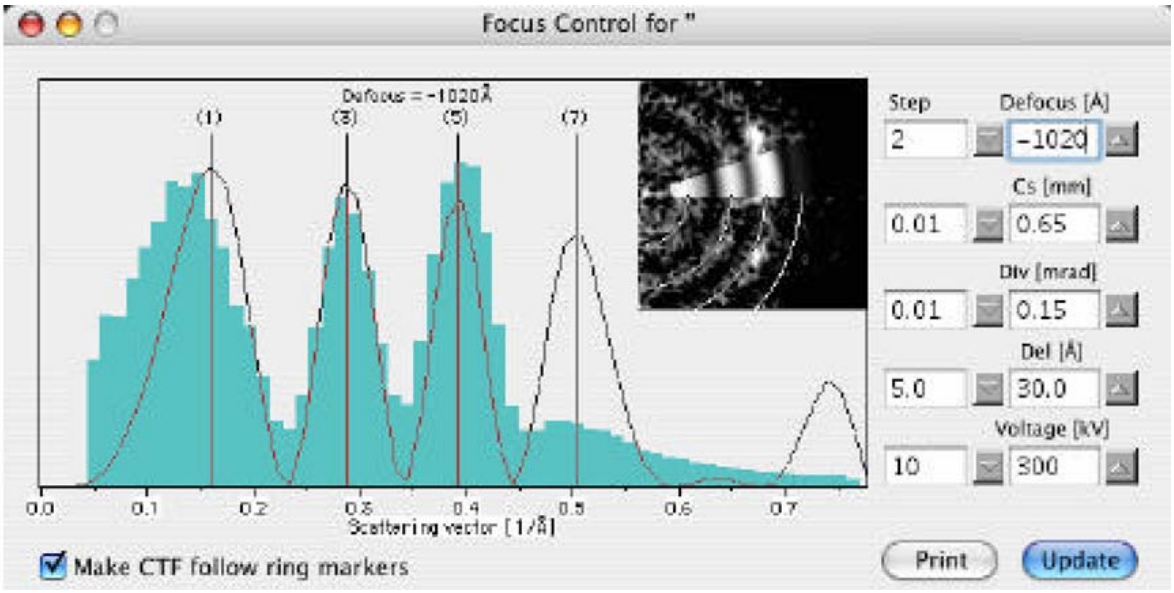


**Figure 6.15:** Focus Control in MacTempas. Defocus Determination is done as described in A-5.2. The other parameters on the right side are microscope-specific and define the form of the CTF. The defocus value is the unknown parameter in the CTF and is therefore estimated through this fitting process. The small square image in the right top corner of the inner box shows the CTF calculated from the image and in the small brighter angular range the CTF based on the input parameters.

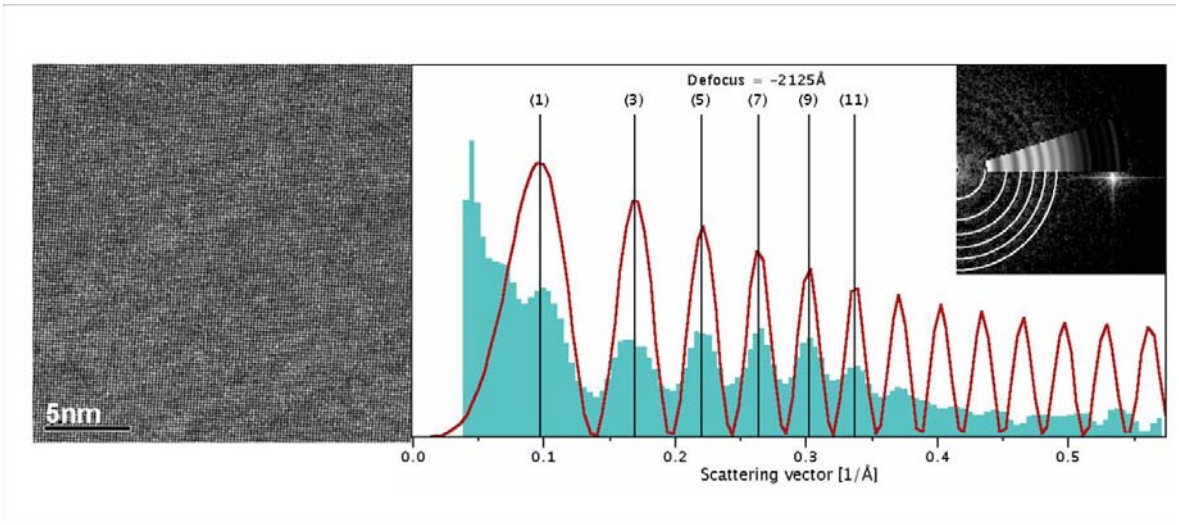


**Figure 6.16:** Defocus determination for sample.

Then the programme tests the input parameters. If nothing appears in the window on the left side, *"Show FSR Warning"* in the *"Display Selection"* has to be checked before, the reconstruction can be started. Therefore *"Test Mode"* has to be unchecked.

**Reconstruction Results**

When the reconstruction is finished the results have to be checked carefully before any aberration correction should be done. *"Show FSR Convergence"* gives you the mean square error, it should be lower than **0.01** for an optimal reconstruction, but that is hardly achievable for nanoparticles. Also the *"Focus Step Analysis"* should be compared to the input value. If it differs too strongly, the reconstruction has to be restarted with the corrected value. Also it is advisable to check the defocus value in the "*Aberration Correction*"-section. Therefor different steps have to be done:

1. choose the "*lens*" in the "*Tool Box*", click on the display, repeat till display only shows the area of interest of the structure. Important: Make sure that "*Phase of Wave Function*" or "*Amplitude of Wave Function*" is checked in the "*Display Selection*".
2. select "*Histogram - Display Area*"
3. vary "*Defocus*" in the "*Aberration Correction*" till the standard deviation in the histogram is minimal for the "amplitude"-image or maximal in the "phase"-image of the wave function
4. add this defocus-value (mind the algebraic sign) and add it to the start defocus value in "*Set Reconstruction Parameters*"
5. rerun the reconstruction

Now the results have to be checked again. If the mean square error is acceptable, the step size analysis matches with the input value and the defocus value has not to be corrected once again, the other aberration corrections can be proceeded."*Aberration Correction*" has to be checked. Here 2-fold astigmatism, coma and 3-fold astigmatism can be corrected. The procedure is the same as it is in 3.: Maximize standard deviation for phase-image and minimize for amplitude image. It is recommended to start with the amplitude-image. If the standard deviation is stable for a huge range, change to the phase-image for further corrections. Mind that all corrections have to be done in a reasonable array: Of course it is possible to correct coma with a value of more than 1000 nm, but this would mean

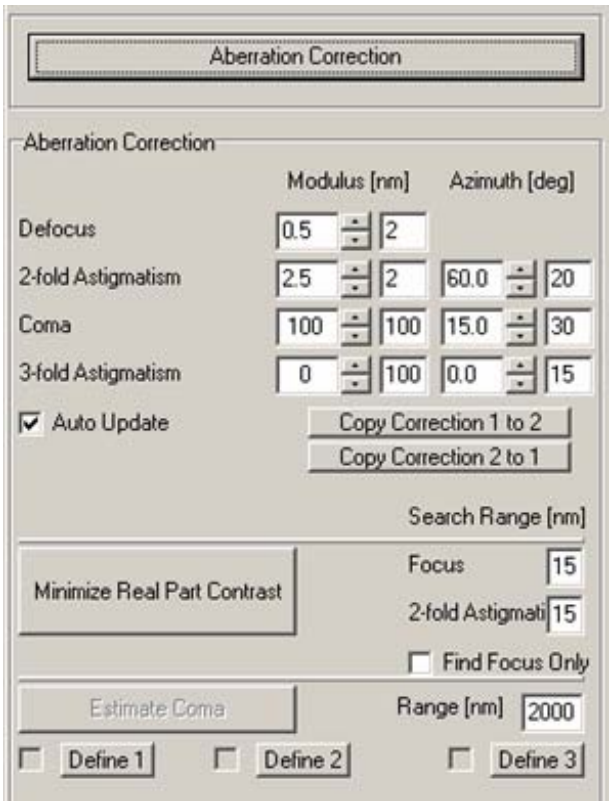


**Figure 6.17:** *"Aberration Correction"*in TrueImage: Correcting defocus, 2- and 3-fold astigmatism and coma is possible. If "*Auto Update*" is checked the image currently in the display will be updated automatically due to every correction step. An automatic estimation and coma is also possible.

the microscope was not very well aligned and so the efficiency of the reconstruction is questionable. There are no fixed values for the maximum correction values, yet experience has provided the following clues for maximal values:

**2-fold astigmatism:** 5 nm

**3-fold astigmatism:** 150 nm

**coma:** 500-700 nm

Iterative correction of the three values is also strongly recommended. Figure 6.17 shows the display for the *"Aberration Correction"*.

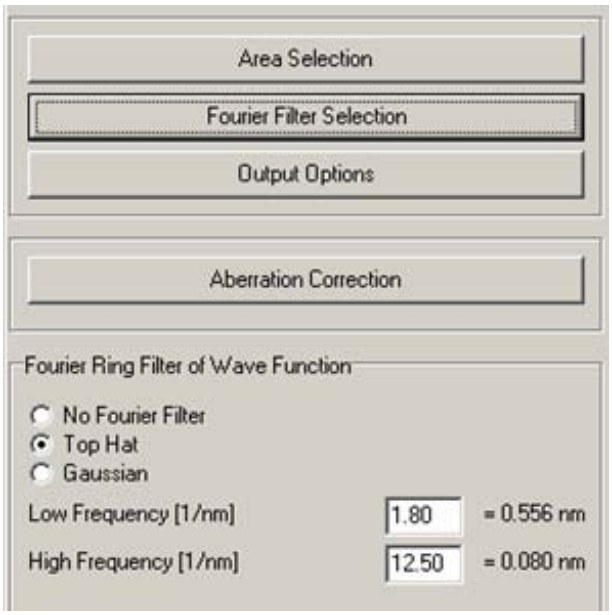


**Figure 6.18:** *"Fourier Filter Selection"*-window in TrueImage: Choosing of two different or no Fourier Filter is possible.

### Using Filters

After finishing the correcting procedure the reconstructed image can be "made perfect" using a filter, that means to cut off the high- and low-frequencies which could not be included in the reconstruction anyway. Attend: The lower the number of images used for the reconstruction the more the low-frequency limit is shifted to higher spatial frequencies. To use the filters check "*Fourier Filter Selection*" and the *"filter-display"* opens as shown in fig. 6.18. Besides "*No Fourier Filter*" there are the options: "*Gaussian*" and "*Top Hat*" which is usually used. The low- and high-frequency limits can be taken from the *".mal.log-file"* see **Saving Files**. The high-frequency level is due to the reconstruction process a little bit larger than $g_{max}$, the info limit of the microscope but can be also set to this value without making the result worse.

### Saving Files

In the older version of TrueImage a file name for the reconstruction will be asked before starting the reconstruction. This was not the case for the version of TrueImage I used @NCEM: Here the files had to be named afterwards, when saving the whole project or exporting some different files. Different output files will be generated, unfortunately the extensions differ between the different versions of TrueImage, the following list explains

the extensions of my used TrueImage version (Version 2.4.4 according to header info in *".mal.log"*-file).

**.dxy:** text file of image alignment and displacement data

**.ewf:** reconstructed electron wave function (exit wave)

**.mal.log:** test file with information on dampening fuctions, high- and low-frequency reconstruction limits and with positional alignment tables for each iteration step

**.mse:** text file with the mean square error of the wave function

**.step.log:** detailed information on focal step analysis, text file

**.ti:** Project files, such as files with extension *".fti"* in a former TrueImage version

To save the files check "*File*" and then "*Save Project as*". All the files named in the description are generated. Then it is also possible to save different parameter files, this option can be found in the" *Export*"-menu. "*File*" also allows for import other projects, wave functions and parameterfiles as can be seen in fig. 6.11. In "*Output Options*", which is shown in fig. 6.19, some settings for the output can be made. There is also the possibility of adding an extra phase-shift. Usually the phase- and amplitude-images are exported in the .tif-format.

It is also possible to export only the display-area. According to the manual this is possible with the "*Area Selection*"-option. The area defined there should be the area which is exported. By clicking on the display with the right mouse-button there is also the possibility of direct .bmp-export of the displayed area. "Working" in the display can be done with the tools from the "*Tool Box*" which is in analogy to the DigitalMicrograph tools.

### Closing Remark

This short manual for dealing with TrueImage Professional based on my experiences gives only a few hints for a succesful reconstruction and does not claim to be complete or 100% perfect. For more detailed information it is strongly recommended to read the relevant manual for the used version of TrueImage. Especially this version has some features as "*Show Argand Plot*" or "*Subtact Vacuum Wave*" which were specially programmed for NCEM and not a part of the normal TrueImage versions. A figure of the TrueImage control panel (fig. 6.20) with an opened EWR-project is shown to close this chapter.

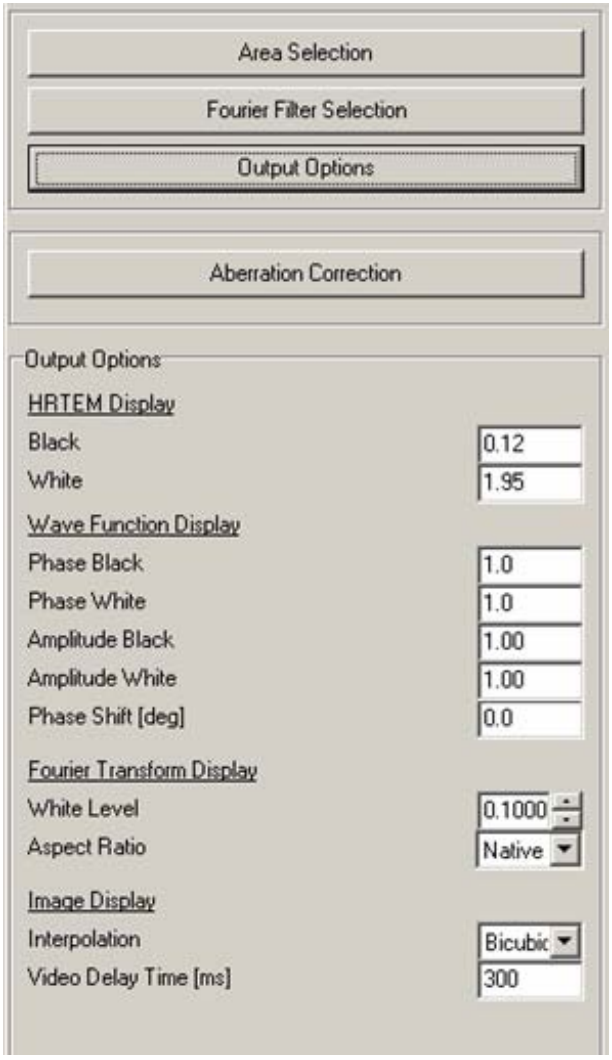


**Figure 6.19:** *"Output Options"*in TrueImage.

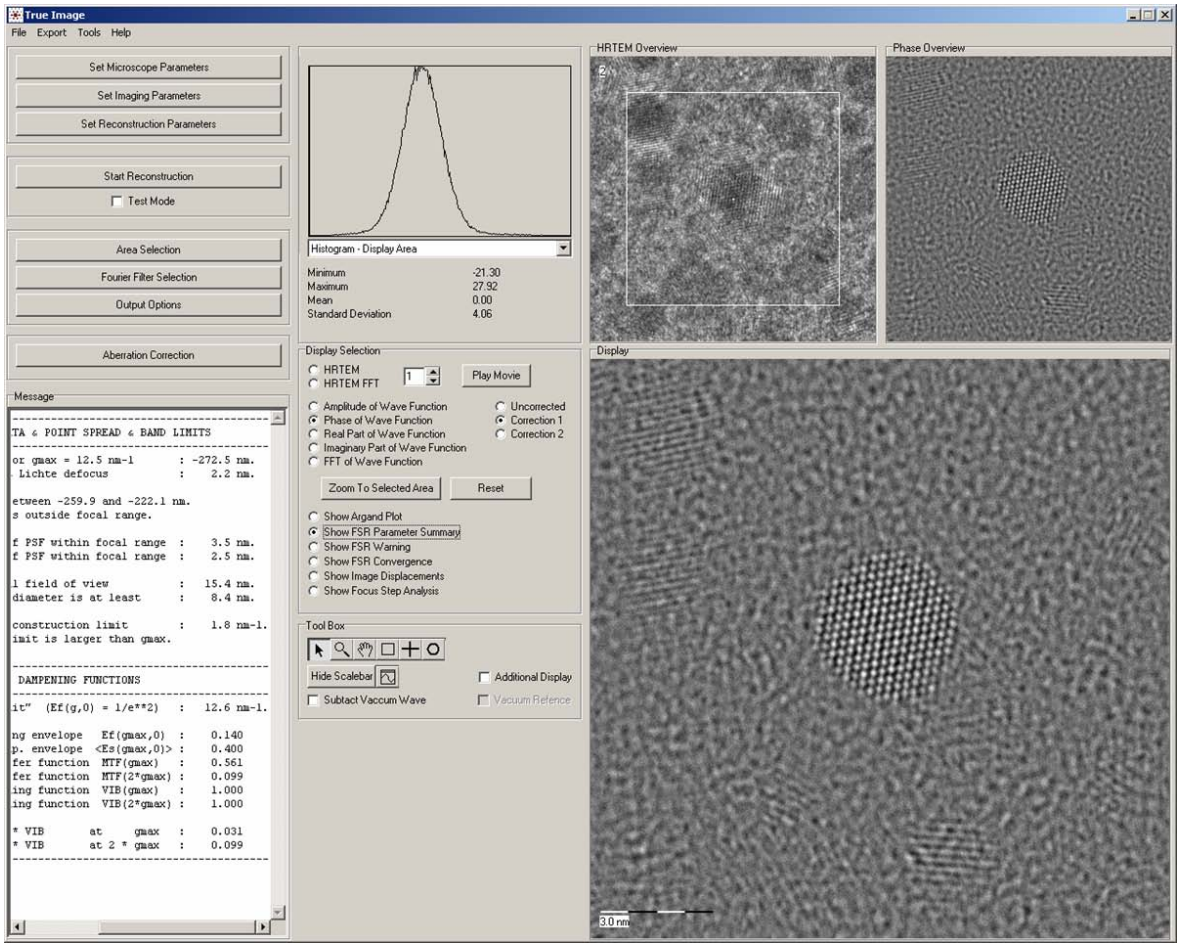


**Figure 6.20:** Control Panel of TrueImage for a opened project. Since "*Show FSR Parameter Summary*" is checked, this summary is displayed in the box on the left bottom side.

# Bibliography


[Ace05] M. Acet, C. Mayer, O. Muth, A. Terheiden, and G. Dyker, *Formation of extended ordered monolayers of FePt nanoparticles*, Journal of Crystal Growth **285**, 365 (2005).

[Ant06a] C. Antoniak, *private communication* (2006).

[Ant06b] C. Antoniak, J. Lindner, M. Spasova, D. Sudfeld, M. Acet, M. Farle, K. Fauth, U. Wiedwald, H.-G. Boyen, P. Ziemann, F. Wilhelm, A. Rogalev, and S. Sun, *Enhanced orbital magnetism in $Fe_{50}Pt_{50}$ nanoparticles*, Phys. Rev. Lett. **97**, 117201 (2006).

[Bal06] S. Bals, G. V. Tendeloo, and C. Kisielowski, *A New Approach for Electron Tomography: Annular Dark-Field Transmission Electron Microscopy*, Adv. Mater. **18**, 892 (2006).

[Boo00] C. B. Boothroyd, *Quantification of high-resolution electron microscope images of amorphous carbon*, Ultramicroscopy **83**, 159 (2000).

[Boo03] C. B. Boothroyd and M. Yeadon, *The phonon contribution to high-resolution electron microscope images*, Ultramicroscopy **96**, 361 (2003).

[Boo05] C. B. Boothroyd and R. E. Dunin-Borkowski, *The contribution of phonon scattering to high-resolution images measured by off-axis electron holography*, Ultramicroscopy **98**, 115 (2005).

[Coe96] W. M. J. Coene, A. Thust, M. O. de Beeck, and D. V. Dyck, *Maximum-likehood method for focus-variation image reconstruction in high resolution transmission electron microscopy*, Ultramicroscopy **64**, 109 (1996).

[Cow57] J. M. Cowley and A. F. Moodie, *The Scattering of Electrons by Atoms and Crystals. I. A New Theoretical Approach*, Acta Cryst. **10**, 609 (1957).

[Dmi03] O. Dmitrieva, *Hochauflösende Elektronenmikroskopie und Kontrastsimulation zur Strukturaufklärung an gesinterten FePt-Nanopartikeln*, Diplomarbeit, Universität Duisburg-Essen (2003).

[Dmi06a] O. Dmitrieva, *private communication* (2006).

[Dmi06b] O. Dmitrieva, M. Acet, J. Kästner, G. Dumpich, C. Antoniak, and M. Farle, J. Phys. D: Appl. Phys. (2006).

[Dmi06c] O. Dmitrieva, M. Acet, J. Kästner, G. Dumpich, and W. .Wunderlich, J. Nanop. Res. **1** (2006).

[Dyc96] D. V. Dyck, H. Lichte, and K. van der Mast, *Sub-Ångstrom structure characterisation: the Brite-Euram route towards one angstrom*, Ultramicroscopy **64**, 1 (1996).

[ea04] W. et al., J. Appl. Phys. **95** (5) (2004).

[Fc06] FEI-company, *FEI Software Overview*, (2006).

[Gro99] H. B. Groen, *Interface dislocation patterns studied with High Resolution TEM*, Doktorarbeit, Reichsuniversität Groningen (1999).

[How63] A. Howie, Proc. R. Soc. **A 275**, 268 (1963).

[Ish80] K. Ishizuka, *Contrast transfer of crystal images in TEM*, Ultramicroscopy **5**, 55 (1980).

[Jin02] J. R. Jinschek, C. Kisielowski, T. Radetic, U. Dahmen, M. Lentzen, A. Thust, and K. Urban, *Quantitative HRTEM investigation of an obtuse dislocation reaction in gold with a Cs corrected microscope*, in *Nanostructured Interfaces. Symposium (Mater. Res. Soc. Symposium Proceedings Vol.727)*, pp. 3–8 (2002).

[Küb03] C. Kübel, D. Tang, T. Fliervoet, and A. Thust, *TrueImage Professional - Step-by-Step Guide (Version 1.0.1 Beta)* (2003).

[Kila] R. Kilaas, *MacTempas User Manual* .

[Kilb] R. Kilaas, *MacTempasX*, http://www.totalresolution.com/ .

[Kir84] E. J. Kirkland, *Improved High resolution Image Processing Of Bright Field Electron Micrographs*, Ultramicroscopy **15**, 151 (1984).

[Kis] C. Kisielowski, E. C. Nelson, C. Song, R. Kilaas, and A. Thust, *Aberration corrected Lattice Imaging with Sub-Angstrom Resolution*, Microscopy and Microanalysis, Supplement 2, 6, 2000, 16 .

[Kis02] C. Kisielowski and J. R. Jinschek, *On the feasibility to investigate point defects by advanced electron microscopy*, in *4th Symposium on non-stoichiometrc III-V compounds, Asilomar, CA* (2002).

[Kis06a] C. Kisielowski, *Electron Crystallography*, pp. 17–29, Springer (2006).

[Kis06b] C. Kisielowski, *private communication* (2006).

[Kit02] C. Kittel, *Einführung in die Festkörperphysik 13. Auflage*, Oldenbourg München (2002).

[Lan92] H. Landolt and R. Börnstein, *Landolt-Boernstein New Series IV/5e*, Springer Berlin (1992).

[Lic91] H. Lichte, *Optimum focus for taking electron holograms*, Ultramicroscopy **38**, 13 (1991).

[Mal97] J.-O. Malm and M. O'Keefe, *Deceptive "lattice" spacings in high-resolution micrographs of metal nanoparticles*, Ultramicroscopy **68**, 13 (1997).

[Mue05] M. Mueller and K. Albe, *Lattice Monte Carlo simulations of FePt nanoparticles: Influence of size, composition, and surface segregation on order-disorder phenomena*, Phys. Rev. B **72**, 094203 (2005).

[O'K01a] M. A. O'Keefe, Microscopy and Microanalysis **7**, 916 (2001).

[O´K01b] M. A. O´Keefe, C. J. D. Hetherigton, Y. C. Wang, E. Nelson, J. H. Turner, C. Kisielowski, J. O. Malm, R. Mueller, J. Rignalda, M. Pan, and A. Thust, *Sub-Ångstrom high-resolution transmission electron microscopy at 300 keV*, Ultramicroscopy **89**, 215 (2001).

[Rei84] L. Reimer, *Transmission Electron Microscopy*, Springer Berlin Heidelberg (1984).

[Rel95] B. Rellinghaus, J. Kästner, T. Schneider, E. F. Wassermann, and P. Mohn, *Thermodynamic analysis of $Fe_{72}Pt_{28}$ Invar*, Phys. Rev. B **51**, 2983 (1995).

[Rel03] B. Rellinghaus, S. Stappert, M. Acet, and E. F. Wassermann, J. Magn. Magn. Mater. **266**, 142 (2003).

[Sch05] P. Schlossmacher, A. Thesen, and G. Benner, *A record-breaking new transmission electron microscope comes close to achieving the theoretical limit of image resolution*, Carl Zeiss SMT, European Semiconductor **27** (3) (2005).

[Sev03] D. Severin, Diplomarbeit, Universität Duisburg (2003).

[Sid] M. V. Sidorov, *ctfExplorer*, http://clik.to/ctfexplorer .

[SM04] V. Salgueiriño-Maceira, L. M. Liz-Marzán, and M. Farle, *Water-Based Ferrofluids from $Fe_xPt_{1-x}$ Nanoparticles Synthesized in Organic Media*, Langmuir **20**, 6946 (2004).

[SM06] V. Salgueiriño-Maceira, M. A. Correa-Duarte, M. Spasova, L. M. Liz-Marzán, and M. Farle, *Composite Silica Spheres with Magnetic and Luminescent Functionalities*, Adv. Funct. Mat. **16**, 509 (2006).

[Sta03a] B. Stahl, J. Ellich, R. Theissmann, M. Ghafari, S. Bhattacharya, H. Hahn, N. S. Gajbhiye, D. Kramer, R. N. Viswanath, J. Weissmüller, and H. Gleiter, Phys. Rev. B **67**, 014422 (2003).

[Sta03b] S. Stappert, *FePt-Nanopartikel aus der Gasphase: Herstellung, Struktur und Magnetismus*, Doktorarbeit, Universität Duisburg-Essen (2003).

[Sta03c] S. Stappert, B. Rellinghaus, M. Acet, and E. F. Wassermann, J. Cryst. Growth **252**, 440 (2003).

[Sud06] D. Sudfeld, *private communication* (2006).

[Sun00] S. Sun, C. B. Murray, D. Weller, L. Folks, and A. Moser, *Monodisperse FePt Nanoparticles and Ferromagnetic FePt Nanocrystal Superlattices*, Science **287**, 1989 (2000).

[Thi98] J. U. Thiele and L. F. et al., J. Appl. Phys. **84**, 5686 (1998).

[Thu96] A. Thust, W. Coene, M. O. de Beeck, and D. V. Dyck, *Focal-series reconstruction in HRTEM: simulation studies on non-periodic objects*, Ultramicroscopy **64**, 211 (1996).

[Tro04] A. Trounova, *Elektronenmikroskiopie zur Strukturcharakterisierung von chemisch synthetisierten $Fe_xPt_{1-x}$-Nanopartikeln*, Diplomarbeit, Universität Duisburg-Essen (2004).

[Vis95] M. R. Visokey and R. Sinclair, Appl. Phys. Lett. **66**, 1692 (1995).

[Wan06] R. Wang, O. Dmitrieva, G. Dumpich, M. Farle, H. Ye, S. Mejía-Rosles, E. Pérez-Tijerina, M. José-Yacamán, H. Poppa, R. Kilaas, and C. Kisielowski, *Layer Resolved Relaxation and Pt Enrichment at the Surface of Magnetic FePt Icosahedral Nanoparticles*, submitted (2006).

[Wha98] S. H. Whang, Q. Feng, and Y. Q. Gao, *Ordering, deformation and microstructure in L10 type FePt*, Acta mat. **46**, 6485 (1998).

[Wil96] D. B. Williams and C. B. Carter, *Transmission Electron Microscopy*, Springer New York (1996).

[Xu05] X. Xu, S. P. Beckman, P. Specht, E. Weber, D. Chrzan, R. P. Erni, I. Arslan, N. Browning, A. Bleloch, and C. Kisielowski, *Distortion and Segregation in a Dislocation Core Region at Atomic Resolution*, PRL **95**, 145501 (2005).

[Yam94] M. Yamamoto, C. Chan, and K. Ho, *First-principles calculations of the surface relaxation and electronic structure of Zr(0001)*, Phys. Rev. B **50**, 7932 (1994).

[Yan05] B. Yang, M. Asta, O. Mryasov, T. Klemmer, and R. Chantrell, *Equilibrium Monte Carlo simulations of A1-L10 ordering in FePt nanoparticles*, Scripta Materialia **53**, 417 (2005).

# Acknowledgements/Danksagung

Mein Dank gilt all denen, die mir durch ihre hilfreiche Unterstützung die Erstellung dieser Diplomarbeit ermöglicht haben.

Insbesondere möchte ich mich herzlich bei meinem Betreuer Prof. Dr. Michael Farle für die sehr interessante Themenstellung und die gute Betreung bedanken.

Frau Dr. Daniela Sudfeld danke ich für die Einarbeitung in die Hochaufgelöste Transmissionselektronenmikroskopie, für gute Zusammenarbeit und vor allem die seelische Unterstützung während meiner Arbeit.

Bei Frau Dipl. Phys. Olga Dmitrieva bedanke ich mich für die Einweisung an der Sputteranlage, die ständige Hilfs- und Diskussionsbereitschaft und eine schöne, wenn auch verregnete, gemeinsame Zeit in Berkeley.

Bedanken möchte ich mich auch bei Michaël Tran und Dr. Olivier Margeat für die Bereitstellung der Proben bzw. Hilfe bei der Präparation.

Ein großes Danke geht an Herrn Dipl. Ing. Horst Zähres für die vielen guten Ideen, seine ständige Hilfsbereitschaft und die Einweisung am TEM.

Dieter Schädel und Wolfgang Kunze danke ich für die Herstellung von Probenhaltern und ihre Hilfsbereitschaft.

Frau Dipl.-Phys. Carolin Antoniak möchte ich für die Durchführung zusätzlicher SPR-KKR Berechnungen danken.

Bei Frau Dr. Marina Spasova und Herrn Dr. Ralf Meckenstock bedanke ich mich für zahlreiche Diskussionen.

Ganz herzlich möchte ich dem NCEM-Team für die Gastfreundschaft und für den angenehmen Forschungs-Aufenthalt danken. Hierbei geht mein besonderer Dank an Herrn Dr. Christian Kisielowski, der durch die gute Betreuung und die vielen faszinierenden Fachgespräche mein Interesse für die Transmissionselektronenmikroskopie geweckt hat.

ChengYu Song danke ich für die Einweisung und Unterstützung am CM300.

Dank der finaziellen Unterstützung durch den DAAD wurde mir mein Forschungs-Aufenthalt am National Center for Electron Microscopy in Berkeley ermöglicht.

Herrn Dr. Alfred Hucht danke ich für das Bereitstellen der Simulationskoordinaten.

Bei Herrn PD Dr. Talaat Al-Kassab möchte ich mich für Tipps bei der Spitzenpräparation und die Bereitschaft FIM Aufnahmen zu machen bedanken.

Allen Gruppenmitgliedern der AG-Farle danke ich für die angenehme Arbeitsatmosphäre.

Mein ganz besonderer Dank geht an meine Familie und meinen Freund, die mich die ganze Zeit unterstützt und immer wieder aufgebaut haben.